TBMCE2025

8th International Conference on
Technologies & Business Models for Circular Economy

Conference Proceedings

Sanja POTRČ Miloš BOGATAJ Zdravko KRAVANJA Zorka NOVAK PINTARIČ
EDITORS

University of Maribor Press

University of Maribor

Faculty of Chemistry and Chemical Engineering

8th International Conference on Technologies & Business Models for Circular Economy

Conference Proceedings

Editors

Sanja Potrč

Miloš Bogataj

Zdravko Kravanja

Zorka Novak Pintarič

April 2026

Title 8th International Conference on Technologies & Business Models for Circular Economy

Subtitle Conference Proceedings

Editors Sanja Potrč
(University of Maribor, Faculty of Chemistry and Chemical Engineering)

Miloš Bogataj
(University of Maribor, Faculty of Chemistry and Chemical Engineering)

Zdravko Kravanja
(University of Maribor, Faculty of Chemistry and Chemical Engineering)

Zorka Novak Pintarič
(University of Maribor, Faculty of Chemistry and Chemical Engineering)

Language editing Shelagh Hedges

Technical editor Jan Perša
(University of Maribor, University of Maribor Press)

Cover designer Jan Perša
(University of Maribor, University of Maribor Press)

Graphic material Sources are own unless otherwise noted.
Authors of proceedings and Potrč, Bogataj, Kravanja, Novak Pintarič (editors), 2026

Conference TBMCE, International Conference on Technologies & Business Models for Circular Economy

Date and location September 3rd to September 5th 2025, Portorož, Slovenia

Likozar (National Institute of Chemistry, Slovenia), Primož Oven (University of Ljubljana, Slovenia), Dragica Marinič (Slovenian national building and civil engineering institute, Slovenia), Vilma Ducman (Slovenian national building and civil engineering institute, Slovenia), Sanja Potrč (University of Maribor, Slovenia)

Published by **University of Maribor**
University of Maribor Press
Slomškov trg 15, 2000 Maribor, Slovenija
https://press.um.si, zalozba@um.si

Issued by **University of Maribor**
Faculty of Chemistry and Chemical Engineering
Smetanova ulica 17, 2000 Maribor, Slovenija
https://www.fkkt.um.si/, fkkt@um.si

Publication type E-book

Edition 1st

Available at http://press.um.si/index.php/ump/catalog/book/1108

Published at Maribor, Slovenia, April 2026

REPUBLIC OF SLOVENIA
MINISTRY OF THE ECONOMY, TOURISM AND SPORT

REPUBLIC OF SLOVENIA
MINISTRY OF COHESION AND REGIONAL DEVELOPMENT

The event was held under the patronage of the Ministry of the Economy, Tourism and Sport and Ministry of Cohesion and Regional Development of the Republic of Slovenia.

With the financial support of:

dem
Dravske elektrarne Maribor

Skupina hse

KRKA

MEREL

Saubermacher Slovenija

TALUM

bia
TRUSTED LAB PARTNER

CIP - Kataložni zapis o publikaciji
Univerzitetna knjižnica Maribor

330:502.131.1(082)(0.034.2)

INTERNATIONAL Conference on Technologies & Business Models for Circular Economy (8 ; 2025 ; Portorož)
8th international conference on technologies & business models for circular economy [Elektronski vir] : [September 3rd to September 5th 2025, Portorož, Slovenia] / editors Sanja Potrč ... [et al.]. - 1st ed. - E-zbornik. - Maribor : University of Maribor, University of Maribor Press, 2026

Način dostopa (URL): https://press.um.si/index.php/ump/catalog/book/1108

ISBN 978-961-299-130-2 (PDF)
doi: 10.18690/um.fkkt.1.2026
COBISS.SI-ID 272982019

ISBN 978-961-299-130-2 (pdf)

DOI https://doi.org/10.18690/um.fkkt.1.2026

Price Free copy

For publisher Prof. Dr. Zdravko Kačič,
Rector of University of Maribor

Attribution
Citiranje Potrč, S., Bogataj, M., Kravanja, Z., Novak Pintarič, Z., (Eds.). (2026). 8th *International Conference on Technologies & Business Models for Circular Economy: Conference Proceedings* Maribor: University Press. doi: 10.18690/um.fkkt.1.2026

8TH INTERNATIONAL CONFERENCE ON TECHNOLOGIES & BUSINESS MODELS FOR CIRCULAR ECONOMY: CONFERENCE PROCEEDINGS
S. Potrč, M. Bogataj, Z. Kravanja, Z. Novak Pintarič (eds.)

University of Maribor Press

Table of Contents

Alkali-Activated Fly Ash Composites with Canine-Fibre Reinforcement

Barbara Horvat,[1] Nadja Železnik,[1] Lara Petrič,[2] Sara Tominc[3]

[1] Milan Vidmar Electric Power Research Institute, Ljubljana, Slovenia
barbara.horvat@eimv.si, nadja.zeletnik@eimv.si
[2] University of Ljubljana, Biotechnical Faculty, Ljubljana, Slovenia
lp46225@student.uni-lj.si
[3] Slovenian National Building and Civil Engineering Institute, Ljubljana, Slovenia
sara.tominc@zag.si

The construction industry contributes over 40% of human-made carbon emissions, due mainly to the high consumption of raw materials and energy-intensive processing. Alkali-activated materials (AAMs) prepared from secondary raw materials such as fly ash (FA) offer a sustainable alternative that is synthesised at low temperatures. In this study, the FA was milled and sieved to achieve higher reactivity and compressive strength (CS). To increase the bending strength, keratin-based fibres from a Chesapeake Bay Retriever were added in mass percentages (m%) of 1 and 5. While the addition of 1 m% of fibres improved the overall mechanical performance and increased the CS by ~20 MPa, the addition of 5 m% resulted in a soft composite that deforms under pressure but returns to its original shape cyclically as the fibres act as an internal cushioning network. However, the CS of the 5 m% fibre-rich composite decreased to 20 MPa, which is 30 MPa lower than the fibre-free sample.

DOI
https://doi.org/10.18690/um.fkkt.1.2026.1

ISBN
978-961-299-130-2

Keywords:
alkali-activated materials, fly ash, keratin-based fibres, Chesapeake Bay Retriever, circular economy

University of Maribor Press

1 Introduction

The construction and civil engineering industry has a significant impact on the environment, contributing over 40% of human-made carbon emissions (*The Industry Creating a Third of the World's Waste*, n.d.), due mainly to the high consumption of raw materials and energy-intensive processing at temperatures above 1000 °C (*Cement Production: How Hot Air Becomes Green Energy*, n.d.).

Alternative materials such as alkali-activated materials (AAMs) are being researched, to reduce the impact on the environment. AAMs can be synthesised from secondary raw materials, often at low temperatures. They represent a more sustainable alternative to conventional cement, and could transform the built environment from a net carbon emitter to a carbon sink (Škvára, 2007).

Alkali activation requires precursors rich in amorphous silicon and aluminium, which form a three-dimensional aluminosilicate network connected by oxygen bridges. The charge imbalance around the aluminium is compensated by the alkali elements (chemical elements from the 1st and 2nd groups of the periodic table) from the liquid alkali reagent (Škvára, 2007). Materials rich in Si and Al include fly ash (FA), a by-product of coal combustion (Horvat et al., 2023; Palomo & Fernández-Jiménez, 2011). However, despite the chemical suitability of FA for alkali activation, FA has physical limitations. The predominantly spherical morphology of FA particles lacks fibrous structures (Horvat et al., 2022), which would contribute naturally to higher bending strength (Traven et al., 2022).

Fibres can be added to overcome the natural physical limitation of the FA. In conventional building materials, synthetic fibres such as polypropylene (Blazy & Blazy, 2021) or steel (Batson, 1976) are used commonly. However, synthetic fibres are not sustainable, as they are made from raw materials, are not recyclable, increase the environmental footprint and the cost of the composite.

Hence, natural fibres are a promising alternative. In the past, animal hairs have been used as reinforcement in mortars and plasters (Dudac, 2019) as they provide mechanical support and durability. However, the behaviour of keratin-based fibres permanently embedded in an alkaline matrix has not been studied systematically, and their performance in AAMs is still largely unknown.

Therefore, this study focuses on the evaluation of the mechanical performance of alkali-activated FA composites reinforced with keratin-based fibres from a Chesapeake Bay Retriever. The presented results demonstrate the potential for environmentally sustainable, high-performance construction materials that utilise unused waste resources.

2 Experimental

2.1 Materials and characterisation of the materials

In the alkali-activated synthesis of the composite, two solid (Figure 1) and one liquid ingredients were used: FA as the precursor, keratin-based hair as the fibres, and an Na-silicate solution as the liquid alkali:

- The precursor used for alkali activation was FA from the Slovenian thermal power plant. The FA was milled and sieved below 125 μm to increase the reactivity in alkaline media. However, as-received FA (labelled as FA) was used as the primary AAM reference for the milled FA (labelled as FA_{milled}) and for the AAMs containing fibres.
- The keratin-based fibres were hairs trimmed from brown short-coated Chesapeake Bay Retrievers (bred under the rules of the Kennel Club of Slovenia and according to the Fédération Cynologique Internationale breed standard) during the shedding period after winter. The collected hair was cut to a length of up to 1 cm.
- The liquid alkali was an Na-silicate solution (Geosil, 344/7, Woelner, 16.9 m% Na_2O, 27.5 m% SiO_2, 55.6 m% H_2O), which was used without further manipulation.

The FA was characterised using complementary analytical techniques, to assess both the chemical and mineralogical composition as well as the organic content: loss on ignition (LOI), X-ray fluorescence (XRF), and X-ray diffraction (XRD):

- The organic residues were quantified by LOI at 550 °C for 2 h.
- The bulk chemical composition, covering elements from fluorine to americium, was determined by XRF (Thermo Scientific ARL Perform'X Sequential XRF)

on samples milled and sieved below 125 μm and treated thermally at 950 °C for 2 h.

– The mineral phases were identified by XRD (Empyrean PANalytical Diffractometer, Cu source) over a 2θ range of 4–70° with a step size of 0.0263°, using Rietveld refinement with X'Pert Highscore plus 4.1 software and corundum (Al_2O_3) as an external standard. The crystalline and amorphous fractions were estimated by comparing the XRD and XRF results element-wise. A detailed summary of the FA characterisation results is provided in Table 1, and all the raw data are available in the open repository.

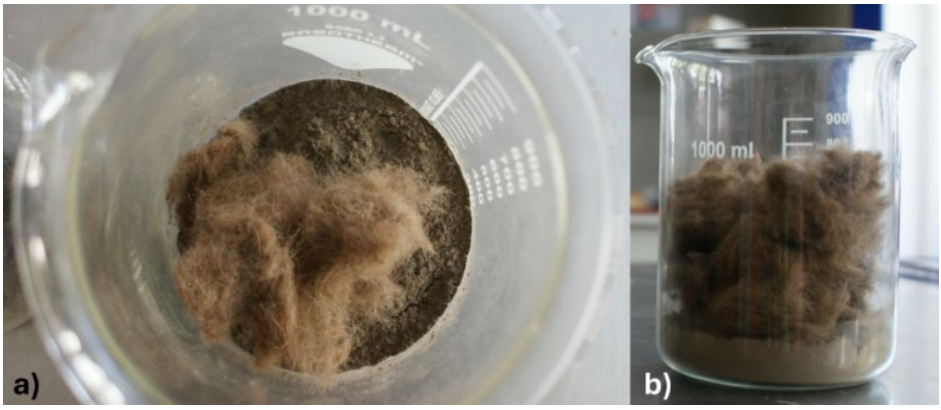

Figure 1: Solid dry ingredients: FA_{milled} at the bottom of the beaker, with a) 1 m%, and b) 5 m% of CBR fibres on top.

Source: own.

Table 1: Content of critical elements for alkali activation in the FA, expressed in mass percent (m%).

Elements [m%]	Na	K	Mg	Ca	Al	Si	Content [m%]
XRF (whole material)	0.7	2.0	1.5	6.3	14.1	20.4	100.0
XRD (crystalline)	0.0	0.0	0.6	0.9	3.2	4.4	25.1
Amorphous	0.7	2.0	0.9	5.4	10.9	16.0	74.9

The mechanical properties (compressive strength, bending strength and geometric density) were evaluated on 3-day-old AAMs using a ToniTechnik ToniNORM testing machine.

2.2 Synthesis of the material

The mixture of FA (and FA_{milled}) and the alkali solution was designed based on the XRF and XRD measurements of the FA, excluding its organic content. The calculation was performed under boundary conditions aimed at avoiding efflorescence with subsequent degradation of the AAM (the ratio of Al to the combined content of chemical elements from the first group of the periodic table was kept close to 1 or slightly lower) and achieving the highest compressive strength (the molar ratio of the amorphous Si to Al was set to 1.9 to 1). The theoretical mass ratio between the FA and liquid alkali was established at 1 to 0.35. The optimal ratio was determined using software developed on the MS Excel platform within the Project no. C3330-17-529032 "Raziskovalci-2.0-ZAG-529032" (Horvat & Ducman, 2019), and later upgraded in the ARIS project under Grant no. J2-3035.

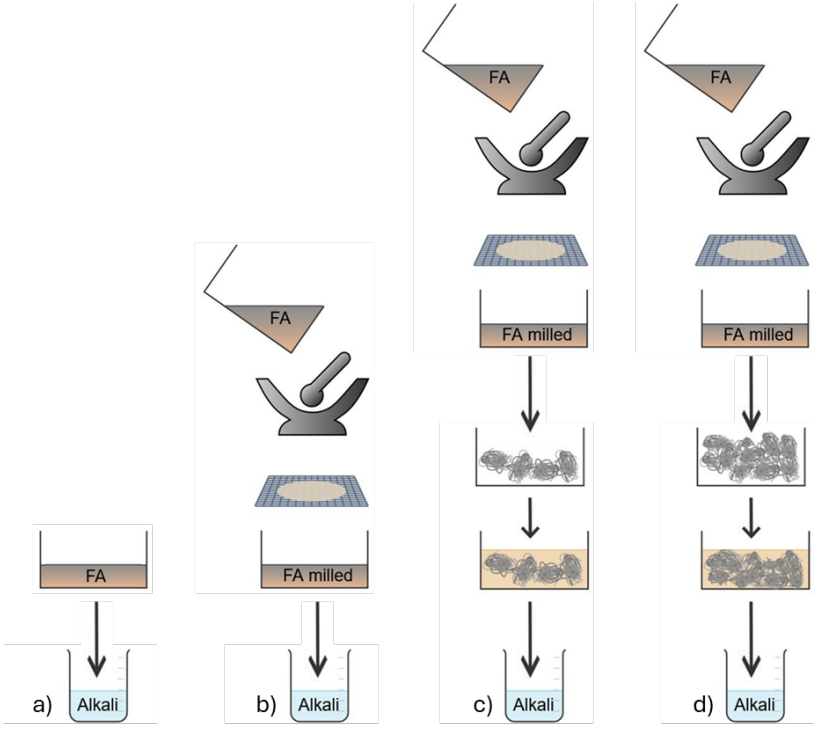

Figure 2: Synthesis scheme: a) as-received FA, without fibres, b) 1 m%, and c) 5 m% fibres.
Source: own.

Four mixtures were prepared with the same mass ratio of the precursor (FA and FA_{milled}) and alkali (1 to 0.35), as shown in Figure 2: a) using the FA as-received and without fibres, b) using the FA_{milled} and without fibres, c) using the FA_{milled} and 1 m% of fibres, and d) using FA_{milled} and 5 m% of fibres. The fibres and FA_{milled} were homogenised in a dry state before being activated with the liquid alkali. The precursor (with/without fibres) and the alkali were mixed for 2 minutes at up to 1000 rpm. The resulting slurry was moulded in silicone rubber moulds with 6 prisms ($2 \times 2 \times 8$ cm^3), and cured for 60 h at 70 °C in a conventional drying chamber, and then exposed to room conditions to cool before the mechanical tests were performed.

3 Results and discussion

With the exception of the AAM composite, which contained 5 m% CBR fibres, the samples showed no noticeable differences in appearance or parameters observable by the naked eye or by touch. As can be seen in Figure 3, the composite with the highest percentage of CBR fibres appeared "hairy," without sufficient binder throughout the volume, and felt soft when pressed between the fingers, suggesting that pavements made from a larger amount of CBR fibres in AAM material could provide a "cushioned" walking experience. The composite showed the ability to recover its shape under cyclic pressure between the fingers.

The mechanical strengths in the MPa and in % (normalised to the values of the AAM without fibres and from the as-received FA) are shown in Figures 4 and 5, respectively. While the compressive strength of the AAM from FA_{milled} increased compared to the AAM based on the as-received FA, the bending strength decreased, which could be due to the loss of non-combusted cellulose particles (large, non-spherical, but non-fibrous) during the mechanical milling of the FA. However, the difference between the mechanical strengths of the AAM from FA_{milled} and from FA is less significant than the difference between the AAM from FA or FA_{milled} and AAM with added fibres. Both the bending and compressive strength increased significantly in the AAM composites with 1 m% CBR fibres, while the "cushion" effect and the lack of binder in the AAM composites with 5 m% CBR fibres led to a significantly lower mechanical performance compared to the fibreless reference.

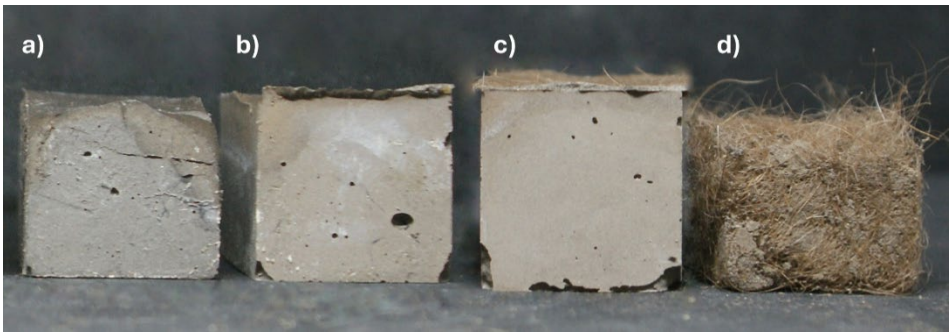

Figure 3: AAM composites with: a) as-received FA and without fibres, b) FA_{milled} and without fibres, c) FA_{milled} and 1 m% fibres, and d) FA_{milled} and 5 m% fibres.

Source: own.

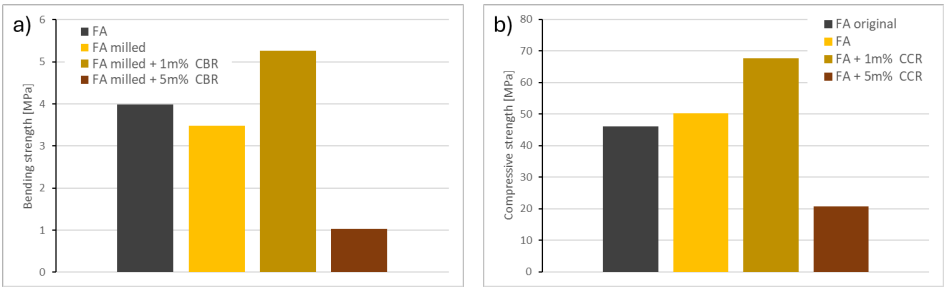

Figure 4: a) Bending, and b) compressive strength of AAM composites in MPa.

Source: own.

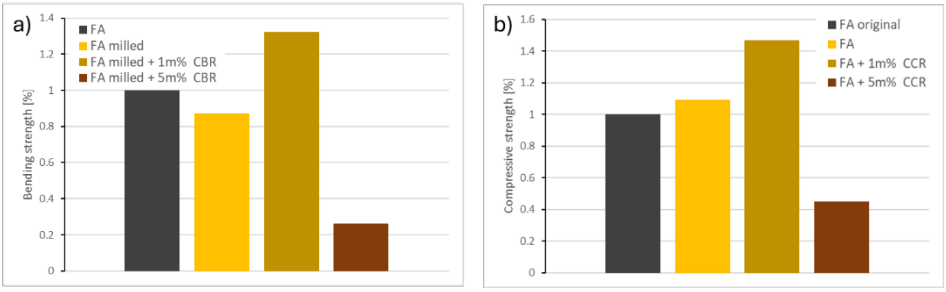

Figure 5: a) Bending, and b) compressive strength of the AAM composites in % (normalised to the values of the AAM without fibres).

Source: own.

When comparing the AAM composites with fibres with the AAM from the as-received FA, the bending strength of the AAM composite with 1 m% CBR fibres increased by more than 30% and the compressive strength by almost 50%. The addition of 5 m% CBR fibres reduced the bending strength by almost 30% and the compressive strength by almost 50%. The highest compressive strength achieved among all the AAM composites was, therefore, almost 70 MPa, and the bending strength was 5 MPa.

The geometric densities of the AAM composites are shown in Figure 6. While the difference in geometric density after the addition of 1 m% CBR fibres falls within the range of measurement error, the decrease in geometric density of almost 20% after the addition of 5 m% CBR fibres is far too large to be explained by measurement or sample preparation errors. In fact, the theoretical value of the densities of the composites is only lower to the 3rd decimal compared to the measured geometric density of the fibre-free AAM (the calculation was performed in kg/l). The current hypothesis is that the decrease in geometric density of the AAM composite with 5 m% CBR fibres is due to the lack of binder in the composite, which is replaced by air (as can also be seen in the photo in Figure 3d).

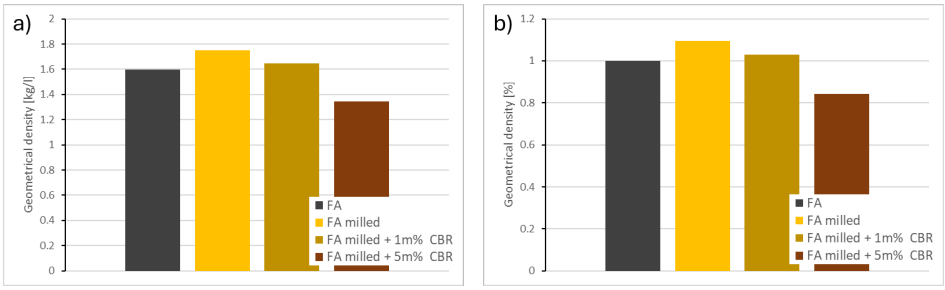

Figure 6: Geometric density of AAM composites in a) kg/l, and b) % (normalised to the values of the AAM without fibres).
Source: own.

Therefore, the decision on the required proportion of the CBR fibres in the AAM must be based on the desired functionality of the building product. A higher mass ratio of CBR fibres can be used for garden paths or insulation panels, but for products that require a higher mechanical performance, the addition of CBR fibres must be less than 5 m%.

4 Conclusion

This study demonstrated that even a small addition of fibres, specifically of dog hair with a functional, naturally water-resistant coat, can lead to unexpectedly high compressive strength values. However, the optimal fibre content and the influence of fibre length still need to be determined experimentally. Equally important is the assessment of the longevity (degradation) of such fibres in an alkaline environment.

Acknowledgment

This study is part of Dr. Barbara Horvat's ARIS project and was supported financially by the Slovenian Research Agency under Grant No. J2-3035. The present study was performed at the Slovenian National Building and Civil Engineering Institute while Dr Horvat was still employed there, for which Dr. Horvat is thankful. Dr. Horvat also thanks the Milan Vidmar Electric Power Research Institute for offering peer review, proofreading, and evaluation of the work by the committee.

Data availability status

The original data presented in the study are openly available in the repository Zenodo at https://zenodo.org/records/17184936 with DOI: 10.5281/zenodo.17184936.

References

Batson, G. (1976). Steel fiber reinforced concrete. *Materials Science and Engineering*, *25*, 53–58. https://doi.org/10.1016/0025-5416(76)90051-3

Blazy, J., & Blazy, R. (2021). Polypropylene fiber reinforced concrete and its application in creating architectural forms of public spaces. *Case Studies in Construction Materials*, *14*, e00549. https://doi.org/10.1016/j.cscm.2021.e00549

Cement production: How hot air becomes green energy. (n.d.). Retrieved 30 September 2024, from https://insights.thyssenkrupp-polysius.com/story/cement-production-how-hot-air-becomes-green-energy/

Dudac, Y. (2019, December 11). History and Use of Horsehair Plaster. *John Canning & Co.* https://www.articleURL

Horvat, B., Češnovar, M., Traven, K., Pavlin, M., König, K., & Ducman, V. (2022). Influence of Homogenization of Alkali-Activated Slurry on Mechanical Strength. *3rd International Conference on Technologies & Business Models for Circular Economy: Conference Proceedings*, 11–50. https://doi.org/10.18690/um.fkkt.2.2022.2

Horvat, B., & Ducman, V. (2019). Potential of Green Ceramics Waste for Alkali Activated Foams. *Materials*, *12*(21), 3563. https://doi.org/10.3390/ma12213563

Horvat, B., Pavlin, M., & Ducman, V. (2023). Influence of microwaves in the early stage of alkali activation on the mechanical strength of alkali-activated materials. *Ceramics International*, *49*(14), 24246–24258. https://doi.org/10.1016/j.ceramint.2022.12.133

Palomo, A., & Fernández-Jiménez, A. (2011). *Alkaline Activation, Procedure for Transforming Fly Ash into New Materials, Part I: Applications*. World of Coal Ash (WOCA) Conference. http://www.flyash.info/

Škvára, F. (2007). Alkali Activated Material—Geopolymer. *Department of Glass and Ceramics Faculty of Chemical Technology*, 16.

The industry creating a third of the world's waste. (n.d.). Retrieved 30 September 2024, from https://www.bbc.com/future/article/20211215-the-buildings-made-from-rubbish

Traven, K., Češnovar, M., Horvat, B., & Ducman, V. (2022). The Influence of Different Fibres Quantity on Mechanical and Microstructural Properties of Alkali-activated Foams. *3rd International Conference on Technologies & Business Models for Circular Economy: Conference Proceedings*, 113–126. https://doi.org/10.18690/um.fkkt.2.2022.9

About the authors

Barbara Horvat, PhD, is a physicist and project leader at the High Voltage and Power Plants Department, in the nuclear group. Her research focuses on radioactive waste (management), (green) building materials, (electrical and thermal) insulation materials, especially fire-resistant electrical cables, semiconductors, the circular economy in material science, and life cycle assessment (LCA). She earned her BSc in Physics with a thesis on eye-safe LIDAR for aerosol detection, and her PhD in Nanophysics, studying photocatalytic degradation of organics using TiO_2 nanoparticles. Her postdoc involved chemical and mineralogical evaluation of primary and secondary raw materials for alkali-activated materials, including software development for recipe optimisation using XRF/XRD. She led teams to multiple circular economy awards for inventions, especially connected with the influence of the electromagnetic field on new materials.

Nadja Železnik, PhD, is a physicist, psychologist and project leader at the High Voltage and Power Plants Department, in the nuclear group. Her work focuses on radioactive waste (management), nuclear legislation, stakeholder engagement, risk perception, emergency preparedness, and communication in environmental and nuclear projects. She earned her BSc in Physics and MSc in Reactor Physics at the Faculty of Mathematics and Physics, and her PhD in Psychology at the Faculty of Arts. With over 35 years of experience, she has contributed to numerous national and international projects, developing legislation, feasibility studies, remediation plans, safety assessments and education and training programmes. She has coordinated multiple EU projects, and serves as an expert for the International Atomic Energy Agency.

Lara Petrič, BSc student, is studying at the Biotechnical Faculty, University of Ljubljana. As part of a summer research internship, she contributed to the synthesis and characterisation of alkali-activated materials within the ARIS project, including sample preparation, mechanical testing and chemical and crystallographic analyses. As a promising student, she has also begun contributing to abstracts and presentations for scientific conferences.

Sara Tominc, PhD, is a researcher at the Department of Materials, in the Laboratory for Cements, Mortars and Ceramics, at the Slovenian National Building and Civil Engineering Institute. Her research focuses on traditional ceramics, and on the beneficial use of waste materials in the construction industry. She obtained her BSc in Chemistry and Chemical Engineering at the University of Maribor and her PhD at the Jožef Stefan Institute, where she investigated the influence of pentavalent dopants on twinning and microstructure development in SnO_2 ceramics for high-performance varistors and dielectrics. She specialises in electron microscopy, thermal analysis and waste characterisation. Recently, she has been investigating accelerated mineral carbonation, aiming to understand the mechanisms and kinetics of CO_2 sequestration and to optimise carbonation conditions.

Summary

The study investigates alkali-activated fly ash (FA) composites reinforced with keratin-based fibres from Chesapeake Bay Retrievers. To increase reactivity, the FA was milled and sieved below 125 μm, while the fibres were incorporated at two mass ratios (1 m% and 5 m%) relative to the FA as part of the preliminary study. Mechanical tests on 3-day-old composites showed that the addition of 1 m%

fibres improved performance significantly, increasing the compressive strength by almost 50% (to ~70 MPa) and bending strength by over 30%. In contrast, the addition of 5 m% fibres resulted in a "hairy", low-binder structure with reduced geometric density and compressive strength. Nevertheless, the fibre-rich composite displayed a unique cushioning effect that restored shape under cyclic pressure, suggesting potential for non-structural applications such as pathways or insulation. The results demonstrated that small additions of keratin fibres can improve the performance of AAM, but excessive fibre content compromises its strength.

Optimisation of Fly Ash Pretreatment for Mechanical Strength and Radioactive Safety in Microwave-Irradiated Alkali-Activated Materials: Preliminary Results

Barbara Horvat,[1] Nadja Železnik,[1] Lara Petrič,[2] Sara Tominc[3]

[1] Milan Vidmar Electric Power Research Institute, Ljubljana, Slovenia
barbara.horvat@eimv.si, nadja.zeletnik@eimv.si
[2] University of Ljubljana, Biotechnical Faculty, Ljubljana, Slovenia
lp46225@student.uni-lj.si
[3] Slovenian National Building and Civil Engineering Institute, Ljubljana, Slovenia
sara.tominc@zag.si

The construction sector is a major contributor to global carbon emissions, due largely to high-temperature processing and extensive use of raw materials. Alkali-activated materials (AAMs), synthesised below 100 °C from secondary raw materials such as fly ash (FA), offer a more sustainable solution. This study investigates the mechanical performance and radionuclide presence of theoretically chemically optimal alkali-activated FA, based on three conditions: untreated FA, FA sieved below 200 μm, and FA treated thermally at 550 °C. Both the sieving and thermal treatment removed the organic content from the FA, resulting in a significant improvement in the compressive strength of the AAMs. However, in the absence of organic content, microwave irradiation no longer improved the compressive strength. Additionally, sieving below 200 μm also reduced the radionuclide content, offering a simple and effective pathway to high-performance, radwaste-safe building materials, even though the radionuclides themselves did not affect the mechanical performance of the AAM.

DOI
https://doi.org/10.18690/um.fkkt.1.2026.2

ISBN
978-961-299-130-2

Keywords:
alkali-activated materials, radioactive fly ash, naturally occurring radioactive material, radionuclide separation, microwave irradiation, circular economy

University of Maribor Press

1 Introduction

The building and civil engineering industry has a significant impact on the environment, by contributing over 40% of human-made carbon emissions (The Industry Creating a Third of the World's Waste, n.d.). This is a consequence of the use of large quantities of raw materials, which account for almost two-thirds of the mass of Mount Everest per year (The Industry Creating a Third of the World's Waste, n.d.), and processing at temperatures exceeding 1000 °C (Cement Production: How Hot Air Becomes Green Energy, n.d.). To reduce the environmental concerns, the building industry is exploring alternative materials, such as alkali-activated materials (AAMs) with synthesis temperatures below 100 °C and secondary raw materials as reagents, which can even transform the built environment from a net carbon emitter into a carbon sink (Škvára, 2007).

Potential precursors for alkali activation are inorganic materials rich in amorphous Al and Si, such as fly ash (FA). Although FA is one of the most researched materials for alkali activation, its main disadvantages (e.g., cellulose and radionuclide content) have not yet been explored sufficiently.

The amount of cellulose in the FA is related directly to the completeness of coal combustion: the more incomplete the combustion, the more organic residues remain in the ash. In contrast to wood used in construction, where cellulose is protected from degradation deliberately through structural design and chemical treatments, the cellulose found in FA is only encapsulated randomly by the surrounding inorganic material of the AAM. The uncontrolled encapsulation may be ineffective, or even detrimental to the long-term durability of the AAMs, as cellulose is prone to degradation. In addition, the FA contains concentrated naturally occurring radioactive materials (NORM), originating from the coal itself. While alkali activation can immobilise radionuclides within a stable aluminosilicate matrix, this entrapment may not be sufficient in cases where the FA exhibits elevated levels of radioactivity, such as the material investigated in this study.

Therefore, this preliminary study aimed to remove the cellulose by mechanical and thermal treatment, while assessing how these treatments affect the radionuclide content in the FA. To evaluate the effect of FA treatment on the AAM performance,

the compressive strength was compared to the AAM produced from the as-received FA, which was used as a reference.

2 Experimental

2.1 Materials and characterisation of the materials

In alkali-activated synthesis, only two ingredients were used- a precursor and a liquid alkali:

- The precursor used for alkali activation was Slovenian FA from the Slovenian Thermal power plant, which is known for its high radionuclide content, which exceeds the regulatory limits for use in construction (Fidanchevski et al., 2024). Therefore, this material cannot currently be reused as part of the circular economy and is classified as 100% waste.
- The alkali component used with the FA was an Na-silicate solution (Geosil, 344/7, Woelner, 16.9 m% Na_2O, 27.5 m% SiO_2, 55.6 m% H_2O), which was used as an aqueous liquid alkali without further manipulation.

The FA was characterised using several complementary techniques:

- Loss on ignition (LOI), performed at 550 °C for 2 h, was used to determine the organic content in the FA,
- X-ray fluorescence (XRF, Thermo Scientific ARL Perform'X Sequential XRF) was used to determine the chemical composition, which includes chemical elements from fluorine to americium. For the XRF analysis, the samples were milled and sieved below 125 μm, and then treated thermally at 950 °C for 2 h.
- X-ray diffraction (XRD, Empyrean PANalytical X-ray Diffractometer, Cu X-Ray source) was used to determine the minerals present in the FA. The samples were milled and sieved below 125 μm, placed in XRD sample holders, and measured under clean room conditions in the 2θ range from 4 to 70° and a step size of 0.0263°.

  The Rietveld refinement of the XRD spectra was performed using the X'Pert Highscore plus 4.1 software and an external standard (corundum, Al_2O_3) to quantify the crystalline content. The amorphous content in the FA was

calculated as the element-wise difference between the XRF and XRD (per element, not per oxide). The summary of the XRF and XRD characterisation results is presented in Table 1, while the raw data are stored in the open repository.

Table 1: Mass percentage ($m_{\%}$) of crucial elements in the alkali activation.

Elements [$m_{\%}$]	Na	K	Mg	Ca	Al	Si	Content [$m_{\%}$]
XRF (whole material)	0.68	2.04	1.53	6.34	14.08	20.40	100.0
XRD (crystalline)	0.00	0.00	0.57	0.94	3.15	4.36	25.1
Amorphous	0.68	2.04	0.96	5.40	10.93	16.04	74.9

To obtain cellulose-free FA for the alkali-activated synthesis, different processing methods were applied to the original FA:

- sieving below 200 μm, between 200 and 400 μm, and above 400 μm, and
- thermal treatment at 550 °C for 2 h at a heating rate of 10 °C/min, followed by natural cooling inside the furnace to room temperature.

The efficiency of the organic content removal in the sieved sample was assessed in the same way as for the as-received FA, namely, by determining the LOI at 550 °C. In parallel, the chemical composition was analysed by XRF spectroscopy, to monitor the presence of radionuclide-related elements that can be detected by the used XRF apparatus.

Only the mechanical properties (compressive strength, bending strength and geometric density) were evaluated in this preliminary study. All the measurements were performed on 3-day-old AAMs using a ToniTechnik ToniNORM testing machine.

2.2 Synthesis of the material

The mixture of FA and alkali solution was pre-calculated using the XRF and XRD results of the original FA, excluding the organic content. The precalculation was performed under boundary conditions, with the aim that for the molar ratio of amorphous:

- Si to Al should be 1.9 to 1 to achieve the highest compressive strength,
- Al to the sum of the chemical elements from the 1st group of the periodic table 1 to 1, or even 1 to <1, to avoid efflorescence and degradation of the AAM.

The theoretically determined mass ratio (using software designed in the MS Excel platform, developed in project no. C3330-17-529032 "Raziskovalci-2.0-ZAG-529032" (Horvat & Ducman, 2019) and upgraded in the ARIS project under Grant no. J2-3035) between the FA and liquid alkali was 1:0.35.

Three mixtures, with the same mass ratio of precursor and alkali (1:0.35, respectively), were prepared using: a) as-received FA, b) FA with the lowest cellulose content (sieved below 200 μm), and c) FA treated thermally at 550 °C for 2 h, as shown in Figure 1.

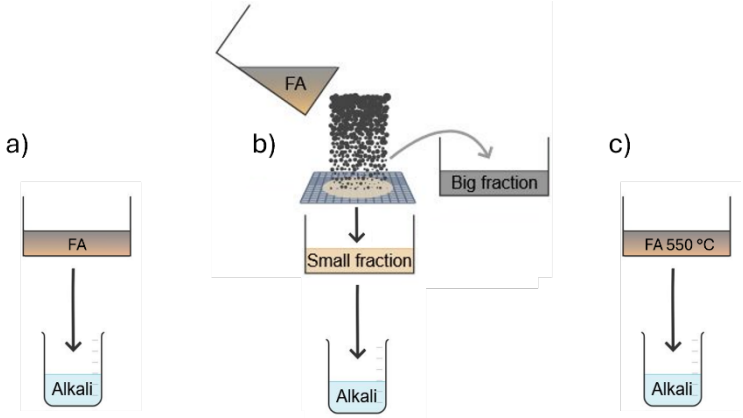

Figure 1: Synthesis scheme.
Source: own.

The precursor and the alkali were mixed for 2 minutes at up to 1,000 rpm. The resulting slurry was then moulded into silicone rubber moulds, each containing 6 prisms (2 × 2 × 8 cm^3), and subjected to one of the following curing procedures:

- Microwave-assisted curing: The mould with only one prism was exposed to low-power microwave irradiation (100 W, inverter microwave oven Panasonic, NN-CD575M, frequency 2.45 GHz, magnetron source) for 2 minutes to induce

volumetric heating, promote dissolution and enhance the reaction kinetics throughout the slurry. The prism was positioned at the 1st observed dosimetry maxima position (~6 cm from the centre of the turntable) (Horvat et al., 2024). After irradiation, the prism remained in the mould, and was cured under conventional conditions at 70 °C for 60 hours.

- Conventional curing: The remaining prisms were cured without microwave treatment, under the same conventional conditions (60 h at 70 °C).

3 Results and discussion

The XRF results for the minor elements, expressed as oxides, together with the LOI values determined at 550 °C, are summarised in Table 2 for the as-received FA and the sieved fractions. Since the thermal treatment at 550 °C does not affect the overall chemical composition of the inorganic content of the FA, and the samples were already pre-treated at 950 °C for XRF analysis, no additional XRF was performed for the thermally treated FA. Namely, its chemical profile was considered to be equivalent to the as-received FA. The changes caused by the thermal treatment are expected at the mineralogical level, but not in the elemental composition.

Although the total organic content in the FA is less than 1 m%, it was not distributed uniformly across the particle size distribution. The largest fractions of FA contain the highest concentration of organic content: (i) the fraction between 200 and 400 μm contained more than 5 m%, and (ii) the fraction above 400 μm contained more than 20 m%.

Because the concentration of radionuclide was above the detection limit of XRF, the radionuclide elements were measured both in the as-received FA and in the coarsest fractions (between 200 and 400 μm, and above 400 μm). However, the presence of radionuclide elements was below the detection limit in the fraction below 200 μm.

Therefore, the fraction below 200 μm was selected as the main sample, as it contained a minimal organic content and no detectable radionuclides based on the XRF analysis.

Table 2: XRF results for minor elements and LOI performed at 550 °C.

Oxides [10^{-2} m%]	CuO	Ga_2O_3	Nb_2O_5	Ag_2O	PbO	ThO_2	PuO_2	LOI 550°C
FA	0.44				0.65		0.52	0.70
FA < 200 µm				1.52				0.62
FA 200 – 400 µm		0.33	0.33			1.07		5.50
FA > 400 µm			0.48				0.66	21.49

The mechanical strengths of the non-irradiated samples are shown in Figure 2, the comparison between irradiated and non-irradiated samples in Figure 3, and their geometric densities in Figures 4 and 5.

The bending strength was below 5 MPa for all the samples, which was to be expected given the absence of fibre material that would increase the flexural resistance. The highest bending strength was observed in the sample prepared from the FA treated thermally at 550 °C. This sample also exhibited the highest geometric density, which is consistent with the effective thermal removal of the organic content. However, the compressive strength, which was already high (46 MPa) for the AAM prepared from the as-received FA, increased further when the cellulose was removed from the precursor, regardless of the procedure (sieving or thermal treatment), reaching up to 62 MPa. Therefore, sieving is considered to be the more favourable method, as it requires significantly less energy for sample preparation, and results in a lower carbon footprint of the final material.

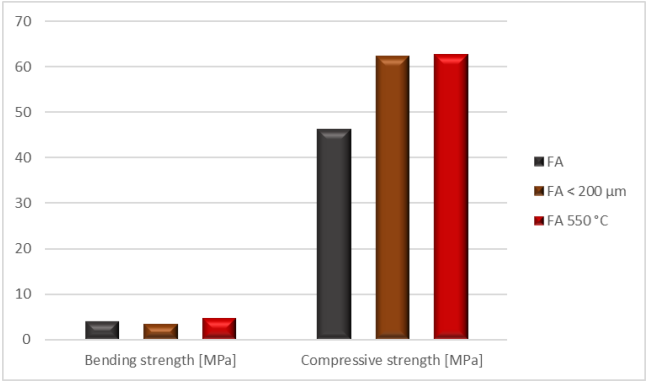

Figure 2: Bending and compressive strength of the non-irradiated samples prepared from the as-received FA, FA sieved below 200 µm, and FA treated thermally at 550 °C.

Source: own.

The experimental results presented in Figure 3 show that the low-power microwave irradiation improved the mechanical properties of the AAM synthesised from the as-received FA. In contrast, no such improvement was observed for the sample prepared from the FA sieved below 200 μm, as the cellulose had already been removed, as well as the radionuclides detectable by XRF.

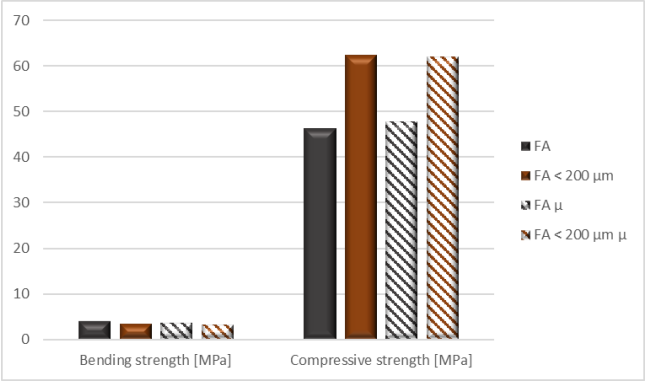

Figure 3: Bending and compressive strength of the non-irradiated and irradiated samples prepared from the as-received FA and the FA sieved below 200 μm.
Source: own.

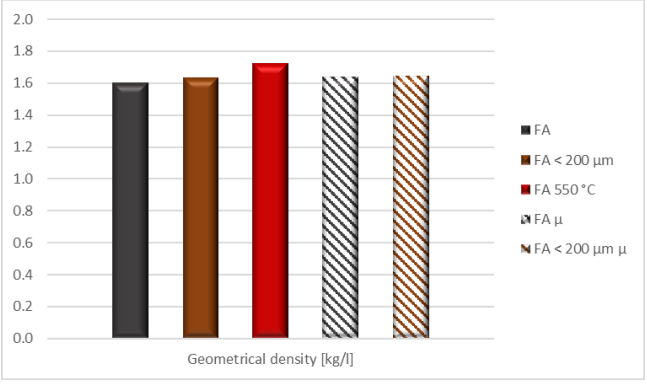

Figure 4: Geometric density of the non-irradiated and irradiated samples prepared from the as-received FA, FA sieved below 200 μm, and the FA treated thermally at 550 °C.
Source: own.

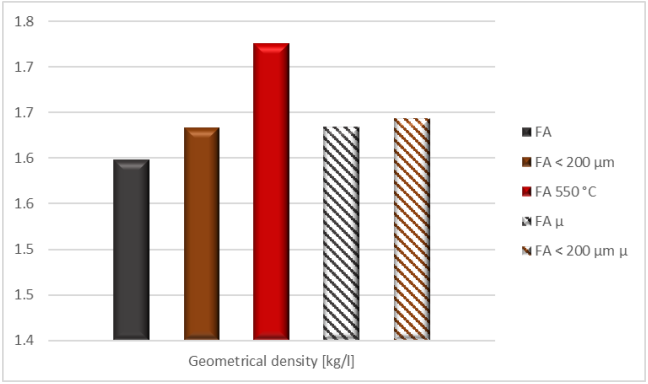

Figure 5: Cut y-axis (for easier comparison of the values) of the geometric density of the non-irradiated and irradiated samples prepared from the as-received FA, FA sieved below 200 µm, and the FA treated thermally at 550 °C.

Source: own.

This suggests that the observed increase in strength after irradiation was due either to thermal degradation of the cellulose present in the as-received FA, or to improved dissolution of the surrounding inorganic material due to localised heating near the cellulose particles. Although the cellulose content was less than 1 m%, the compressive strength increased by 2 MPa after irradiation. However, the intentional addition of cellulose to the FA would probably not lead to a significantly higher increase in compressive strength after irradiation, as the cellulose itself does not contribute to the mechanical performance of the inorganic AAM matrix, and would most likely reduce the compressive strength (Pavlin et al., 2022). Indeed, the samples with removed cellulose had 16 MPa higher compressive strength than the samples with cellulose.

Nevertheless, the presence of radionuclides had no observable impact on the mechanical behaviour of the AAM, as their concentrations were too low to influence the bulk-scale properties.

4 Conclusion

This study has shown that even a small amount of cellulose affects the mechanical performance of AAMs negatively, and that their removal, particularly by sieving, is an efficient, cost-effective, energy-saving, environmentally friendly and low-carbon

solution. While the separation of radionuclide needs further validation, the addition of a sieve represents a viable pathway for the development of high-performance, environmentally sustainable and radwaste-safe construction materials.

Acknowledgment

This study is part of Dr. Barbara Horvat's ARIS project and was supported financially by the Slovenian Research Agency under Grant No. J2-3035. The present study was performed at the Slovenian National Building and Civil Engineering Institute while Dr Horvat was still employed there, for which Dr. Horvat is thankful. Dr. Horvat also thanks the Milan Vidmar Electric Power Research Institute for offering peer review, proofreading, and evaluation of the work by the committee.

Data availability status

The original data presented in the study are openly available in the repository Zenodo at https://zenodo.org/records/16531514 with DOI: 10.5281/zenodo.16531514.

References

Cement production: How hot air becomes green energy. (n.d.). Retrieved 30 September 2024, from https://insights.thyssenkrupp-polysius.com/story/cement-production-how-hot-air-becomes-green-energy/

Fidanchevski, E., Šter, K., Mrak, M., Rajacic, M., Koszo, B. D., Ipavec, A., Teran, K., Žibret, G., Jovanov, V., Aluloska, N. S., Loncnar, M., Žibret, L., & Dolenec, S. (2024). Characterization of Al-Containing Industrial Residues in the ESEE Region Supporting Circular Economy and the EU Green Deal. Materials, 17(24), 6245. https://doi.org/10.3390/ma17246245

Horvat, B., & Ducman, V. (2019). Potential of Green Ceramics Waste for Alkali Activated Foams. Materials, 12(21), 3563. https://doi.org/10.3390/ma12213563

Horvat, B., Knez, N., Hribar, U., König, J., & Mušič, B. (2024). Thermal insulation and flammability of composite waste polyurethane foam encapsulated in geopolymer for sustainable building envelope. Journal of Cleaner Production, 446, 141387. https://doi.org/10.1016/j.jclepro.2024.141387

Pavlin, M., Horvat, B., & Ducman, V. (2022). Fibre Reinforced Alkali-Activated Rock Wool. 3rd International Conference on Technologies & Business Models for Circular Economy: Conference Proceedings, 77–94. https://doi.org/10.18690/um.fkkt.2.2022.6

Škvára, F. (2007). Alkali Activated Material - Geopolymer. Department of Glass and Ceramics Faculty of Chemical Technology, 16.

The industry creating a third of the world's waste. (n.d.). Retrieved 30 September 2024, from https://www.bbc.com/future/article/20211215-the-buildings-made-from-rubbish

About the authors

Barbara Horvat, PhD, is a physicist and project leader at the High Voltage and Power Plants Department, in the nuclear group. Her research focuses on radioactive waste (management), (green) building materials, (electrical and thermal) insulation materials, especially fire-resistant electrical cables, semiconductors, the circular economy in material science, and life cycle assessment (LCA). She earned her BSc in Physics with a thesis on eye-safe LIDAR for aerosol detection and her PhD in Nanophysics, studying photocatalytic degradation of organics using TiO_2 nanoparticles. Her postdoc involved chemical and mineralogical evaluation of primary and secondary raw materials for alkali-activated

materials, including software development for recipe optimisation using XRF/XRD. She led teams to multiple circular economy awards for inventions, especially connected with the influence of the electromagnetic field on new materials.

Nadja Železnik, PhD, is a physicist, psychologist, and project leader at the High Voltage and Power Plants Department, in the nuclear group. Her work focuses on radioactive waste (management), nuclear legislation, stakeholder engagement, risk perception, emergency preparedness, and communication in environmental and nuclear projects. She earned her BSc in Physics and MSc in Reactor Physics at the Faculty of Mathematics and Physics, and her PhD in Psychology at the Faculty of Arts. With over 35 years of experience, she has contributed to numerous national and international projects, developing legislation, feasibility studies, remediation plans, safety assessments, and education and training programs. She has coordinated multiple EU projects and serves as an expert for the International Atomic Energy Agency.

Lara Petrič, BSc student, is studying at the Biotechnical Faculty, University of Ljubljana. As part of a summer research internship, she contributed to the synthesis and characterisation of alkali-activated materials within the ARIS project, including sample preparation, mechanical testing, and chemical and crystallographic analyses. As a promising student, she has also begun contributing to abstracts and presentations for scientific conferences.

Sara Tominc, PhD, is a chemist at the Department of Materials, in the Laboratory for Cements, Mortars and Ceramics, at the Slovenian National Building and Civil Engineering Institute. Her research focuses on traditional ceramics and on the beneficial use of waste materials in the construction industry. She earned her BSc in Chemistry and Chemical Engineering at the University of Maribor and her PhD at the Jožef Stefan Institute, investigating the influence of pentavalent dopants on twinning and microstructure development in SnO_2 ceramics for high-performance varistors and dielectrics. She specialises in electron microscopy, thermal analysis and waste characterisation. Recently, she has been investigating accelerated mineral carbonation, aiming to understand the mechanisms and kinetics of CO_2 sequestration and to optimise carbonation conditions.

Summary

The study investigates the optimisation of fly ash (FA) pretreatment for producing alkali-activated materials (AAMs) with high mechanical strength and reduced radioactive content. Three FA conditions were compared: as-received, sieved below 200 μm, and treated thermally at 550 °C. Both the sieving and thermal treatment removed the residual cellulose effectively, enhancing the compressive strength significantly, while the microwave irradiation improved the strength only in the as-received FA containing organic content. Sieving below 200 μm also reduced the detectable radionuclides, providing a simple, energy-efficient and low-carbon approach to synthesising high-performance, radwaste-safe AAMs. The preliminary results highlight sieving as a promising method to produce environmentally sustainable construction materials from radioactive FA.

Energy-Efficient Coatings: The Role of Heat-Reflecting Pigments

Mirica Karlovits,[1] Mirjam Leskovšek,[2]
Blaž Likozar,[1] Uroš Novak[1]

[1] National Institute of Chemistry, Ljubljana, Slovenia
mirica.karlovits@ki.si, blaz.likozar@ki.si, uros.novak@ki.si
[2] University of Ljubljana, Faculty of Natural Sciences and Engineering, Ljubljana, Slovenia
mirjam.leskovsek@ntf.uni-lj.si

DOI
https://doi.org/10.18690/um.fkkt.1.2026.3

ISBN
978-961-299-130-2

Given the increasing global demand for energy and the escalating climate crisis, the development of energy-efficient materials has become increasingly important. Heat-reflecting pigments play a key role in the formulation of coatings that reduce solar heat gain, thereby contributing to passive cooling strategies in buildings, vehicles and infrastructure. By reflecting infrared light and reducing heat, infrared reflective coatings can keep objects cooler and provide significant benefits across a range of applications. The main objective of our research was to investigate the influence of pristine cellulose nanocrystal (CNC) coatings and pigmented CNC coatings on the absorbance, reflectance and transmittance of light in the UV-VIS-NIR regions. In the study four different pigments were used (one heat-reflective and three effect pigments), which differ in chemical composition and particle size.

Keywords:
heat-reflecting pigments,
cellulose nanocrystals,
energy efficiency,
solar heat,
coatings

University of Maribor Press

1 Introduction

Applications in the field of Heat Management, such as glass windows, require both protection against infrared radiation and adequate visible light transmission to ensure that the interior spaces are illuminated. To fulfill these demands materials are needed exhibiting high transmission values in a certain spectral area (e.g. visible light) while, in other areas (e.g. the NIR spectrum), the transmission of light is decreased. Materials with reduced infrared light transmission are used frequently in thermal insulation and heat management applications (Greiler et al., 2021).

For exterior coatings requiring heat protection (e.g. horticulture and architecture), inorganic pigments with strong IR reflectance are an excellent solution (Sameera et al., 2017). Energy consumption could be decreased not only by cooling, but also by using special infrared reflective coatings. When solar reflectance increases, the surface temperature decreases; solar radiation is reflected rather than absorbed. Infrared reflective coatings can keep objects cooler and have major advantages in a wide range of applications (Mara et al., 2023; Blaco et.al, 2023). A cool coating reflects a high percentage of incident infrared radiation, while transmitting high levels in the visible spectra. This will reduce the amount of solar energy entering the substrate, which results on a cool surface when exposed to the sun (Sameera et al., 2017).

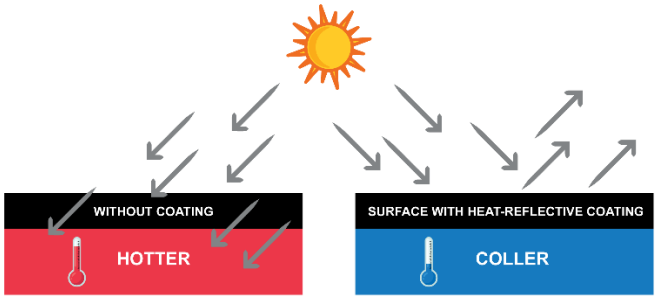

Figure 1: Schematic illustration of a heat-reflective coating.

Conventional coating technologies decrease the transmission of light while they reduce the energy of solar radiation. In contrast, heat-reflecting pigments reflect the sunlight's invisible heat radiation while allowing the majority of the visible light to

pass through. Compared to conventional coating, they offer more light, less heat and higher UV absorption (Merck, 2019).

In cases of surfaces exposed to sunlight, solar energy can be transmitted, reflected, or absorbed. The electrons in a substance exposed to sunlight will absorb light wave energy and change their energy state when the frequency of the incoming light is near to their electron energy levels. In other words, the absorbed light is converted into thermal energy. The absorption of light depends on the nucleus and on the electrons. In its transmission, light moves through a substrate, and, at the reflection of different wavelengths, the angle of incidence of the light is equal to that of the reflection on smooth surfaces; consequently, the light bounces back from the surface (Mara et al., 2023).

Sunlight contains visible light and non-visible radiation such as ultraviolet light (UV-light) and infrared light (IR-light) (Greiler et al., 2021). The composition of the solar spectrum includes 52% NIR radiation (700-2500 nm), 43% visible (VIS) light (400-700 nm), and 5% ultraviolet (UV) radiation (100-400 nm). Over half of the solar radiation accounts for infrared radiation (Mansour et al., 2025, La Notte et al., 2020). The UV radiation is divided further into: UV-C (100-280 nm, which is generally created from artificial light sources), UV-B (280-315 nm, being the most energetic component of natural UV light), UV-A (315-400 nm, which accounts for the lowest energy of UV light) (Roy et al., 2023).

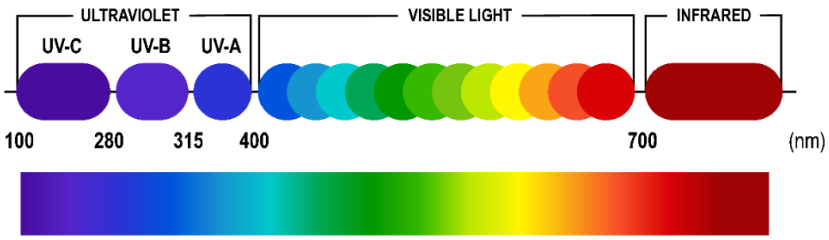

Figure 2: The solar spectrum.

Near infrared light plays an important role in heat generation. The absorbed sunlight increases the temperature and requires more cooling energy, additionally it can cause physical damage (Mara et al., 2023). However, these radiations on absorption result

in heating up of the surface of the material which is exposed to the sunlight. A significant amount of heat is absorbed into the surface through conduction (Jose et a., 2019).

2 Materials and methods

In this study a commercially available cellulose nanocrystals "CNCs" (Table 1) as a binder and four different special pigments were used (Table 2), which were coated in a machine direction using a K Control Coater / meter bar coating (wire diameter: 0.05 mm, wet film deposit: 4 µm) on translucent paper (G = 100 g/m²). The coating formulation was based on pigments mixed with cellulose nanocrystals (CNCs) at a ratio of 20:100. Before the measurement the samples were placed in standard conditions of 23 °C and 50% humidity for one day.

Table 1: Properties of the cellulose nanocrystals (CNCs).

Parameter	**Specification**
Chemical name	$C_6O_5H_{10}$
Colour	White-translucent
Form	Aqueous suspension, 2-5wt.% solids
Surface	Hydrophilic
Average size (Scherrer method, SEM)	10-15 nm wide,150-300 nm length
Crystallinity (XRD:Segal method)	90,3 %
Initial decomposition temperature	285 °C
Density	Aqueous gel: 1.04 g/cm³
Lihnin content	Negligible

Table 2: Properties of the pigments.

Pigment label	**Trade name**	**Form**	**Pigment type**	**Chemical composition**	**Particle size**
HRP	Iriotec 9770	Powder	Heat - reflecting pigment	Mica coated with SiO_2, TiO_2, SnO_2	5 -60 µm
EP1	Symic A001	Powder	Effect pigment	Synthetic mica	1 - 15 µm
EP2	Spectraval W	Powder	Effect pigment	Natural mica	5 - 25 µm
EP3	Pyrisma T30-23	Powder	Effect pigment	Mica-based iron oxide	5 - 35 µm

A Scanning Electron Microscope - SEM (JSM-5610JOEL) was used to evaluate the pigment particles. The absorption (A), transmission (T) and reflectance (R) spectra of the coated pigments were obtained with a Lambda 950 UV-VIS-NIR

spectrometer (PerkinElmer, USA) in the range of wavelengths from 200 nm to 2500 nm, at 10-nm intervals.

Figure 3 shows a SEM image of the cellulose nanocrystals (CNCs).

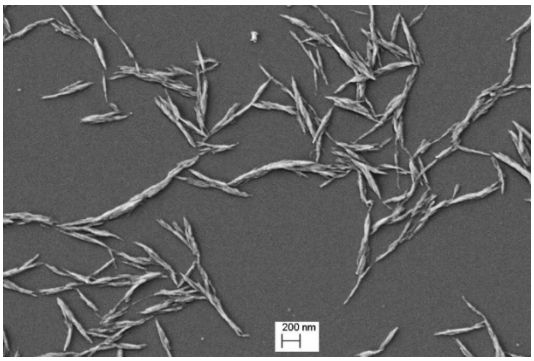

Figure 3: SEM image of the cellulose nanocrystals
Source: (Nanocrystacell, 2023).

The cellulose nanocrystals (CNCs), a kind of rod-like nanoparticles obtained from sulphuric acid hydrolysis of natural cellulose sources such as wood, cotton, tunicates and bacteria, have gained great interest owing to their abundant sources, biocompatibility, high specific surface area, high thermal stability and unique optical properties. CNC suspensions can self-organise into chiral nematic liquid crystal structures, and this helical-layered structure can be retained in solid films via an evaporation-induced self-assembly process, thereby leading to iridescent colour (Feng et al., 2023).

3 Results and Discussion

Figure 4 shows the scanning electron microscope (SEM) micrographs of all four pigments at 500x magnification used in this study. In both pigments examined (EP1 and EP4), the "corn flake" morphology is clearly recognisable, in which the particles appear as thin, irregular flakes with sharp edges and relatively smooth surfaces.

Pigment HRP (Iriotec 9770, Figure 4a) is a mica-based heat-reflecting pigment. It reflects the invisible heat radiation from sunlight while allowing most visible light to pass through. It enables the diffusion of visible light while reducing UV and NIR

transmission. It provides more light, less heat, and higher UV absorption, exhibiting properties similar to sun-protective filters on all transparent substrates.

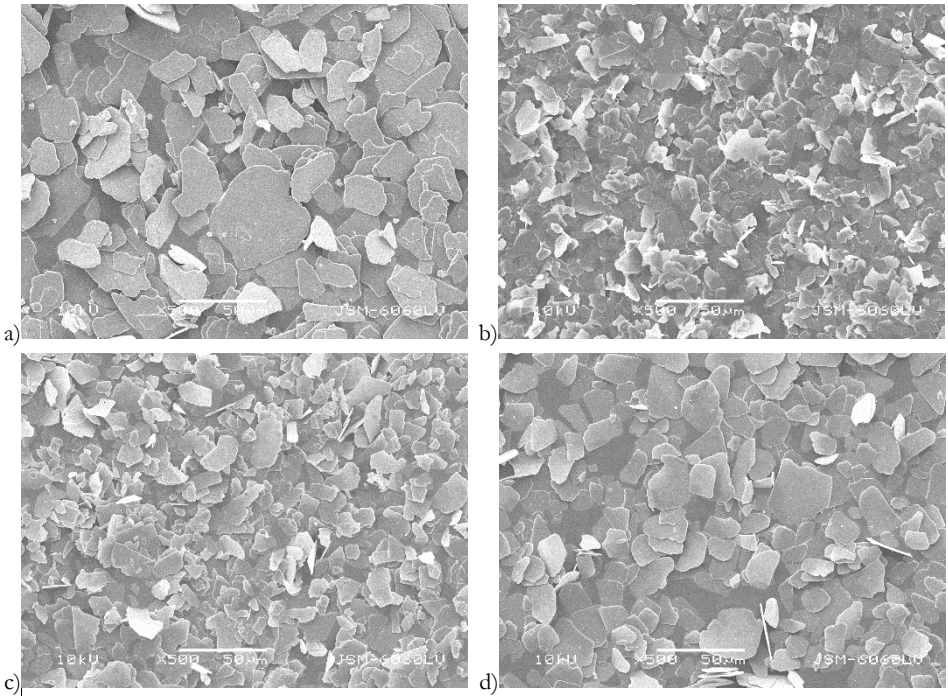

Figure 4: SEM images of the pigments:
a) HRP, b) EP1, c) EP2 and d) EP3.

Pigment EP1 (Symic A001, Figure 4b) is an interference silver-coloured, pearlescent pigment based on synthetic mica. It offers weather-resistance, and provides new styling possibilities for exterior and architectural powder coating applications.

Pigment EP2 (Spectraval White, Figure 4c) is a pearlescent pigment based on natural mica. It offers an interference and silky effect.

Pigment EP3 (Pyrisma T30-23, Figure 4d) is an interference pigment with specially developed titanium dioxide interference layers based on natural mica (Coating Ingredients Master Catalogue, 2017).

Figure 5 shows the absorbance spectra of two types of coatings: pristine CNC and pigmented CNC (labels HRP, EP1, EP2 and EP3), measured across a wide wavelength range (200–2500 nm), which includes the **UV, visible (VIS), and near-infrared (NIR)** regions of the spectrum.

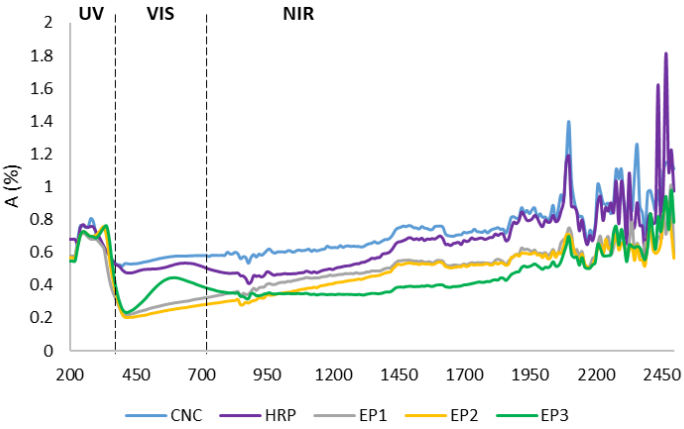

Figure 5: Absorbance spectra of pristine CNC and pigmented CNC coatings in the UV-VIS-NIR regions.

In the physical sense, absorption describes the reception of an angle, a particle or wave. More precisely, the absorption of light is defined as the total or partial, wavelength-dependent transfer of electromagnetic energy to matter. Thus, absorption comes along with a conversion into another form of energy like heat. Black materials like carbon pigments are almost ideal absorbers (Kehren, 2010). All the samples showed relatively high absorbance in the UV region. The highest peak was achieved by the pristine CNC coating at 250 nm, being A = 0,77%. In the VIS region, the absorbance decreased for all the samples. In the case of the pigments` evaluation, pigment EP2, which is based on natural mica, showed the lowest absorbance, while pigment HRP (the heat-reflecting pigment) showed the highest. Pigments EP1, EP2 and EP3 obtained the lowest peaks in the UV region between 410 and 440 nm. In the NIR region, all the samples tended towards higher absorbance, with the peak value was for pigment HRP at 2470 nm being A = 1.8%. On average, CNC had the highest values in the VIS and NIR regions.

The results of the reflectance spectra of pristine CNC and pigmented CNC coatings in the UV-VIS-NIR regions are shown in Figure 6.

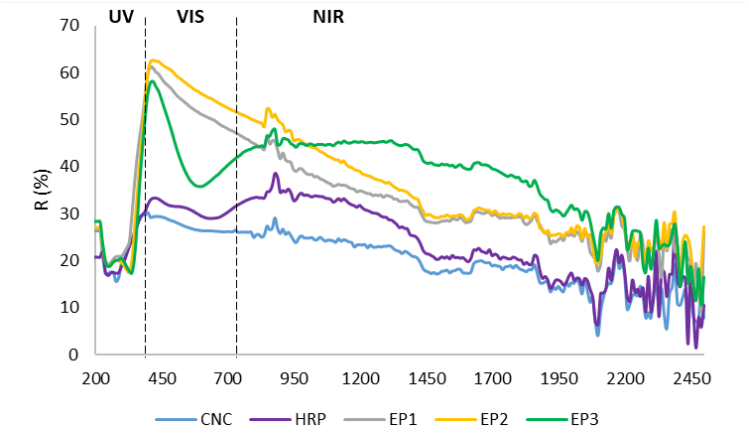

Figure 6: Reflectance spectra of pristine CNC and pigmented CNC coatings in the UV-VIS-NIR regions.

As demonstrated in Figure 6, the reflectance in the UV region was the lowest for all the samples. The CNC film exhibited the lowest overall reflectance across the spectrum. Its reflectance remained mainly between 20–35%, with only a moderate rise in the VIS region. This behaviour is typical for cellulose-based coatings, which are generally transparent to semi-transparent and do not scatter NIR radiation strongly. In the VIS region, significant differences appeared between the pigments (HRP, EP1–EP3). The pigment based on natural mica, E2, achieved the highest reflectance values, with a peak R value of 62.6% at 420 nm, while the heat-reflecting pigment HRP showed the lowest reflectance values in all three regions (UV, VIS, NIR). The heat-reflective pigment (HRP) showed moderately elevated reflectance in both VIS and NIR, but remained lower compared with the EP pigments. Its reflectance stayed in the ~25–45% range. The solar reflectance of a material depends on its surface orientation, which varies the spectral and angular distributions of the incident sunlight. The position of the sun and atmospheric conditions, such as resistance due to clouds, humidity, wind and temperature, also influences the solar reflectance of a material. Solar heat gain is the solar power absorbed per unit surface area, which is related t strongly o solar reflectance (Jose et a., 2019).

Figure 7 shows the transmittance spectra of pristine CNC and pigmented CNC coatings in the UV-VIS-NIR regions.

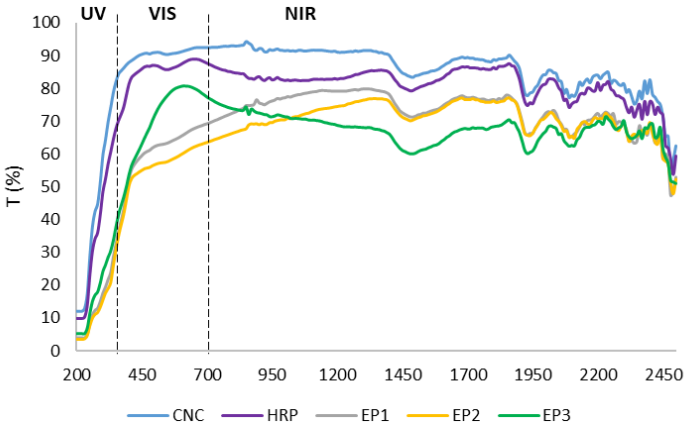

Figure 7: Transmittance spectra of pristine CNC and pigmented CNC coatings in the UV-VIS-NIR regions.

Transmittance is defined as the light passing through an object that is not reflected or absorbed (Kehren, 2010). Among all the pigments, the heat-reflecting pigment (HRP) exhibited the highest values across all three regions (UV-VIS-NIR), with the transmission peak occurring between 630 and 700 nm. This higher transmission can be explained by the chemical composition of pigment HRP. The transmission through a coating containing pigments is influenced by two effects, the absorption of the pigment and the interference effects. Silica or mica are almost transparent materials for light. However, metal oxide like titania or iron oxide absorbs UV-light and can, by this, decrease the transmission in the spectral area of UV-light. A high percentage transmittance indicates that little or no light is being absorbed (Greiler et al., 2021).

The transparency of CNCs is an essential property for their application in optically clear materials. They exhibited high optical transparency in the visible light range. The films exhibited transmittance values exceeding 80 %, indicating their suitability for transparent applications (Arockiasamy et al., 2024).

4 Conclusion

This study demonstrated that incorporating special-effect and heat-reflective pigments into cellulose nanocrystal (CNC) coatings influences their optical properties significantly across the UV–VIS–NIR spectral regions. The pristine CNC

films showed the lowest reflectance and moderate absorbance and transmittance, confirming their inherently transparent and weakly scattering nature. When pigments were incorporated into the CNC coat, clear spectral differences emerged that were strongly dependent on the pigment composition and particle morphology.

Among the evaluated pigments, the effect pigments (EP1, EP2 and EP3) exhibited the highest reflectance values, particularly in the visible and near-infrared regions. In contrast, the the heat-reflective pigment (HRP) showed only moderate reflectance, but provided the highest transmittance across all three spectral regions.

The absorbance measurements confirmed further that CNC-based coatings containing pigments EP series maintain the lowest absorbance in the VIS region, whereas the heat-reflective pigment (HRP) demonstrated the highest absorbance in all the measured spectra. Overall, the results show that the pigment type dictates the balance between reflectance, absorbance and transmittance strongly in incorporating into CNC coating.

This work provides a foundation for the further development of CNC-based, energy-efficient coating systems for use in heat-sensitive applications.

Acknowledgment

The authors would like to acknowledge the financial support of the Horizon Europe Project UPSTREAM (GA 101112877).

References

Arockiasamy, F.S. *et al.* (2024) 'Navigating the Nano-world Future: Harnessing Cellulose Nanocrystals from Green Sources for Sustainable Innovation', *Heliyon*, pp. e41188–e41188. Available at: https://doi.org/10.1016/j.heliyon.2024.e41188.

Blasco-Zarzoso, S., Beltrán-Mir, H. and Cordoncillo, E. (2023) 'Sustainable inorganic pigments with high near-infra-red reflectance based on Fe3+ doped YAlO3 for high temperature applications', Journal of Alloys and Compounds, 960, p. 170695. Available at: https://doi.org/10.1016/j.jallcom.2023.170695.

Coating Ingredients Master Catalog: all products from all suppliers (2017) Specialchem.com. Available at: https://www.specialchem.com/coatings (Accessed: 17 November 2025).

Greiler, L.C. and Mahltig, B. (2021) 'Pearlescent Effect Pigments for Coatings on Textiles -Part I: Protective Materials Against UV Light and IR...', *ResearchGate*, 7, pp. 73–83. Available at:

https://www.researchgate.net/publication/365275708_Pearlescent_Effect_Pigments_for_Coatings_on_Textiles_-Part_I_Protective_Materials_Against_UV_Light_and_IR_Light.

Kehren, K. (2013) Optical properties and Visual Appearance of Printed Special Effect Colors. PH diss., Technischen Universität Darmstadt, pp. 23-50.

La Notte, L. et al. (2020) Hybrid and organic photovoltaics for greenhouse applications, Applied Energy, 278, p. 115582.

Feng, K. *et al.* (2023) 'Cellulose Nanocrystals Chiral Nematic Coating with Reversible Multiple-Stimuli-Responsive Coloration', *ACS Sustainable Chemistry & Engineering*, 11(22), pp. 8374–8385. Available at: https://doi.org/10.1021/acssuschemeng.3c01782.

Jose, S. *et al.* (2019) 'Recent advances in infrared reflective inorganic pigments', *Solar Energy Materials and Solar Cells*, 194, pp. 7–27. Available at: https://doi.org/10.1016/j.solmat.2019.01.037.

Mara, J., Attila-Ede Bodnár, László Trif and Judit Telegdi (2023). Development of Effective Infrared Reflective Coatings. Applied sciences, 13(23), pp.12903–12903. doi:https://doi.org/10.3390/app132312903.

Mansour, S.A. and Farha, A.H. (2025) 'A Review of Near-Infrared Reflective Nanopigments: Aesthetic and Cooling Properties', *Crystals*, 15(3), pp. 271–271. Available at: https://doi.org/10.3390/cryst15030271.

Merck (2019) Merck - The Vibrant Science & Technology Company, Merckgroup.com. Available at: https://www.merckgroup.com/en.

Nanocrystacell (2023). Available at: https://www.nanocrystacell.eu/?lang=sl (Accessed: 18 February 2025).

Sameera, S. *et al.* (2017) 'High IR reflecting BiVO 4 -CaMoO 4 based yellow pigments for cool roof applications', *Energy and Buildings*, 154, pp. 491–498. Available at: https://doi.org/10.1016/j.enbuild.2017.08.089.

Roy, Swarup, et al. (2023) Recent Progress on UV-Light Barrier Food Packaging Films - a Systematic Review. Innovative Food Science & Emerging Technologies, Vol. 91, Elsevier BV, pp. 103550–50.

Utilisation of Industrial Red Gypsum for Sustainable Cementitious and Geopolymer Composites

Gregor Kravanja,[1, 2] Grega Kos,[3]
Pavel Blagotinšek,[3] Dejan Verhovšek,[3]
Tinkara Marija Podnar[1]

[1] University of Maribor, Faculty of Civil Engineering, Transportation Engineering and Architecture, Maribor, Slovenia
gregor.kravanja@um.si, tinkaramarija.podn@student.um.si
[2] University of Maribor, Faculty of Chemistry and Chemical Engineering, Maribor, Slovenia
gregor.kravanja@um.si
[3] Cinkarna Celje, d.d., Celje, Slovenia,
grega.kos@cinkarna.si, pavel.blagotinsek@cinkarna.si, dejan.verhovsek@cinkarna.si

This study investigates the potential utilisation of industrial red gypsum (RG), a by-product of titanium dioxide production, as a sustainable component in cementitious and geopolymer composites. Cement pastes, mortars and metakaolin-based geopolymers were prepared with partial replacement of the main binder by RG (5–50 wt%) to evaluate its effects on workability, porosity, hydration and mechanical performance. The experimental results showed that small additions of RG (5 %) enhanced the mechanical strength of cement mortars slightly due to its micro-filling and nucleation effects, while higher contents reduced the strength and workability because of the increased water demand and porosity. In geopolymers, RG acted mainly as an inert filler, with strength decreasing significantly beyond 10 % replacement. Response Surface Methodology (RSM) confirmed an optimal composition range at low RG dosages. The results demonstrate that limited RG incorporation can contribute to a circular economy strategy in construction, promoting waste valorisation and reducing cement consumption.

DOI
https://doi.org/10.18690/um.fkkt.1.2026.4

ISBN
978-961-299-130-2

Keywords:
red gypsum, cementitious composites, geopolymers, mechanical strength, circular economy, RSM optimisation

University of Maribor Press

1 Introduction

Cement is among the most extensively produced materials on Earth, and, by mass, is second only to water in global consumption (Environment et al., 2018). However, the production of each ton of ordinary Portland cement results in the emission of approximately one ton of carbon dioxide into the atmosphere (Hamada et al., 2021). Consequently, the scientific community has focused on developing alternative construction materials capable of replacing cement partially or fully, aiming to reduce its consumption while maintaining the overall quality and performance of concrete.

Supplementary cementitious materials (SCMs) are inorganic substances that enhance the performance of concrete. They can be classified as inert, latent hydraulic, or pozzolanic. Inert SCMs act primarily as fillers, providing nucleation sites that accelerate the hydration and hardening of cement while, simultaneously, filling voids and promoting microstructural densification in cementitious systems. Latent hydraulic SCMs, which are rich in calcium or reactive silicates, react with water to form calcium silicate hydrate (C–S–H) gels, either independently, or in combination with ordinary Portland cement (OPC) (Rashad et al., 2013; Zhang & Ye, 2012). Incorporating SCMs enhances the mechanical performance, durability and microstructural density of cement composites. Favourable results were provided by incorporating bentonite (Al-Hammood et al., 2021), biomass ash (Thomas et al., 2021), metakaolin (Kravanja & Knez, 2023), volcanic ash (Calderoni et al., 2024) and fly ash (Podnar et al., 2025). Natural SCMs showed greater potential for replacing cement than artificial ones, thereby reducing the energy demand and environmental impact (Fode et al., 2023).

Despite that, the limited research on both the short-term and long-term effects of incorporating emerging SCMs into concrete is one of the main factors preventing their widespread adoption in industrial applications (Jhatial et al., 2023).

Red gypsum (RG) is an industrial by-product generated during titanium dioxide production via the sulphate process. It is most often landfilled, which leads to environmental and spatial concerns due to the large volumes produced (Ju et al., 2023; Sotiriadis et al., 2024). However, because of its mineralogical composition, RG has attracted attention as a potential secondary raw material in sustainable construction. Previous studies demonstrated that RG can be used in cementitious

and gypsum-based binders, even providing photocatalytic and self-cleaning properties (Xie et al., 2024). The valorisation of RG therefore represents an opportunity to support the principles of the circular economy by reducing industrial waste and transforming it into a valuable construction resource.

In addition to cement-based systems, geopolymer technology has emerged as a promising alternative binder system capable of achieving high mechanical strength (Castillo et al., 2021) and chemical stability (Lingyu et al., 2021) with significantly lower CO_2 emissions (Huang et al., 2023). Geopolymers are formed through the alkaline activation of aluminosilicate precursors, and their reaction mechanisms allow for the inclusion of various industrial residues, such as fly ash, slag, or red gypsum, as reactive or partial filler components. Their amorphous gel structure and dense matrix often result in enhanced durability and chemical resistance compared to traditional Portland-based binders (Das et al., 2022).

To ensure efficient material design and property optimisation, the use of Design of Experiments (DOE) has gained attention in material research. These statistical approaches allow systematic evaluation of multiple parameters—such as curing time, temperature, water-to-binder ratio and additive content—while minimising the number of experiments required (Jiju, 2023). Applying DOE to red gypsum–based cementitious and geopolymer systems can thus provide valuable insight into the interaction effects between material variables and their influence on mechanical and durability performance.

Therefore, this study aims to evaluate the potential utilisation of industrial red gypsum as a supplementary or partial replacement material in sustainable cementitious and geopolymer composites. The research focuses on understanding how the RG incorporation affects the binding behaviour, durability, porosity and mechanical properties of both material types. Furthermore, the study explores the applicability of RSM for optimising the mixture design and performance prediction. The findings are expected to contribute to the broader goal of developing low-carbon construction materials and advancing the sustainable management of industrial by-products.

2 Materials and Methods

2.1 Raw Materials

The Red gypsum (RG) used in this study was obtained from Cinkarna Celje d.d. (Slovenia), where it is produced as a by-product of TiO_2 manufacture via the sulphate process. The excess sulphuric acid is neutralised with limestone and lime milk, yielding a reddish-brown residue composed mainly of $CaSO_4 \cdot 2H_2O$, with minor Fe and Ti oxides, quartz, Mg hydroxides, and traces of heavy metals.

The as-received material, delivered as moist pressed cakes (~49 wt% moisture), was dried at 40 °C, ground and sieved (<90 μm) according to SIST EN 196-6, to ensure homogeneity and reproducibility.

For cementitious mixtures, Ordinary Portland Cement (CEM I 52.5 R, SIST EN 197-1) was used to isolate the effect of the RG on hydration and strength.

For geopolymer synthesis, the metakaolin (MK) was activated by NaOH–Na_2SiO_3 solutions.

2.2 Sample Preparations

The cement pastes were prepared by replacing the OPC partially with 5 %, 10 %, 15 %, and 20 % RG by mass, while maintaining the total binder content constant. The mixtures were designed and tested in accordance with SIST EN 196-3, which specifies procedures for determining the standard consistency, setting time and soundness of cement pastes.

The water content was adjusted to achieve a Vicat penetration between 5 mm and 7 mm. The RG was previously dried, ground finely (< 90 μm), and stored in sealed containers to prevent moisture re-absorption. All the samples were cured at 20 ± 1 °C and 98 % RH until testing.

The cement mortars were prepared following SIST EN 196-1, using a cement : sand mass ratio of 1 : 3 and a fixed water-to-cement ratio (w/c) = 0.5. Standard quartz sand conforming to SIST EN 196-1, Section 5.1.2 was used to ensure reproducibility.

The cement in the reference mix was replaced progressively with 5 %, 10 %, and 15 % RG by mass. The mixtures were cast into 40 × 40 × 160 mm prisms, compacted and cured under controlled conditions (20 ± 1 °C, RH > 95 %).

The workability was determined using the mini-slump test (ASTM C1437), and the porosity was measured according to SIST EN 1015-7. The compressive and flexural strengths were evaluated after 1, 7, and 28 days, as specified in SIST EN 196-1.

To analyse the influence of the RG content and curing time, the Response Surface Methodology (RSM) was applied to the experimental results.

The geopolymer mixtures were designed using a Design of Experiments (DOE) approach, to evaluate the effect of RG incorporation on the mechanical and microstructural performance. The mixtures were based on metakaolin replaced partially by RG at 0%, 10%, 25%, and 50% by mass, using the activator ratios Na_2SiO_3 : NaOH = 2 : 1(B1 mix) and 1 : 1 (B2 mix). Each mix contained NaOH solutions of 8 M, 9 M, or 10 M, with a water-to-binder ratio of approximately 0.1 and a sand-to-binder ratio of 2 : 1. Two curing regimes were applied:– ambient curing at room temperature, and accelerated curing at 60 °C for 24 h, followed by 7 days of laboratory ageing. This procedure enabled evaluation of the influence of RG on the geopolymerisation, setting behaviour and mechanical performance.

2.3 Characterisation methods

2.3.1 Determination of the Binding Properties and Durability of the Cement Pastes

The binding behaviour of cement pastes with and without red gypsum (RG) was evaluated following SIST EN 196-3. The tests included:

- standard consistency, determined using the Vicat apparatus to achieve a penetration depth of 5–7 mm,
- setting time, measured with the Vicat needle (cross-section 1 mm^2), where the initial set corresponds to a penetration 3–5 mm from the mould bottom and the final set to ≤ 1 mm,

- soundness (dimensional stability), assessed using the Le Chatelier method, where the expansion of the specimen after boiling in water was measured to ensure stability (< 10 mm).

All the pastes were prepared at 20 ± 1 °C and 98 % relative humidity and tested immediately after curing.

2.3.2 FTIR–ATR Analysis of the Cement Pastes

The Fourier Transform Infrared Spectroscopy with Attenuated Total Reflectance (FTIR–ATR) technique was applied to identify functional groups and reaction products in the hydrated cement pastes.

Spectra were collected in the 4000–600 cm^{-1} range using a diamond ATR crystal. The characteristic peaks were interpreted as follows:

- Broad bands near 3400 cm^{-1} → -OH stretching from the bound water;
- Signals between 2000–2400 cm^{-1} → CO_2 adsorption and carbonate formation;
- Peaks around 1400 cm^{-1} → carbonate groups (CO_3^{2-}) associated with $CaCO_3$;
- Absorptions near 1000 cm^{-1} → sulphate groups (SO_4^{2-}) from the gypsum;
- Features near 700–850 cm^{-1} → mineral phases common to all hydrated systems.

The analysis enabled qualitative comparison of the hydration and carbonation processes in pastes containing varying RG contents.

2.3.3 Mortar Characterisation (Workability, Porosity, Strength)

The workability of fresh mortars was determined using the mini-slump test (ASTM C1437), where the average spread diameter (in mm) indicates the flowability.

The porosity was measured according to SIST EN 1015-7, by determining the air content of fresh mortar using a 1 L calibrated pressure vessel.

The mechanical testing followed SIST EN 196-1. Mortar prisms (40 × 40 × 160 mm) were cured for 1, 7, and 28 days, and tested for flexural and compressive strength using a standard testing machine.

The results were calculated according to Equations (1-2):

$$\sigma_f = \frac{3\,FL}{2b^3} \tag{1}$$

$$\sigma_c = \frac{F}{A} \tag{2}$$

where σ_f is the flexural strength (MPa), F is the maximum load (N), L is the span length (mm), b is the side length of the square cross-section (mm), and σ_c is the compressive strength (MPa), with A as the loaded area (mm^2). Both tests were performed for cement-based and geopolymer mortars, to ensure comparability of strength development and durability.

2.4.4 Application of the RSM Approach

Response Surface Methodology (RSM) was employed to analyse and optimise the influence of the key parameters.

A quadratic polynomial model was fitted to the experimental data, to evaluate the combined and interactive effects of the independent variables.

For cement mortars, RSM was used to model the relationship between the RG content, porosity, workability and compressive strength.

The RSM approach allowed efficient visualisation of nonlinear trends and identification of the optimum mixture compositions while minimising the number of experimental runs.

3 Results and discussion

3.1 Cement pastes with red gypsum

The influence of red gypsum (RG) on the binding behaviour and stability of cement pastes was examined systematically through standard consistency, setting time, soundness and FTIR–ATR analyses. Ordinary Portland cement (CEM I 52.5 R) was replaced partially by 5 %, 10 %, 15 %, and 20 % RG by mass, while a reference mix without RG served as the control.

The results showed that the incorporation of RG increased the water demand to reach standard consistency, with the reference mixture requiring 122 g of water and the 15 % and 20 % RG pastes requiring 149 g and 158 g, respectively. This higher water requirement is attributed to the fine particle size and high surface area of the RG, which enhances water absorption and reduces the fluidity of the paste.

Table 1 summarises the effect of the red gypsum (RG) addition on the setting time of the cement pastes. The data show that a small RG content (5 %) delayed both the initial and final set slightly compared to the reference mixture, while the higher RG contents (15–20 %) accelerated setting significantly. This indicates a transition from a mild retardation effect at low dosages to a pronounced acceleration of hydration at higher sulphate concentrations.

Table 1: Initial and final setting time in hours.

	REF	RS-5%	RS-10%
Initial setting time	2:00	2:30	2:00
Final setting time	2:35	3:20	2:45

The Le Chatelier test confirmed excellent dimensional stability across all the mixtures, with expansions between 0 and 1.5 mm, well below the permissible 10 mm limit, indicating that RG does not induce volumetric instability, and may even contribute to matrix densification.

The FTIR–ATR spectra supported these findings further, revealing broad -OH stretching bands near 3400 cm^{-1} that intensified with the RG content due to the increased bound water, as well as carbonate-related peaks around 1400 cm^{-1} and

sulphate-associated absorptions near 1000 cm^{-1}, confirming the coexistence of carbonate and sulphate phases in the hydration matrix.

Overall, the partial replacement of cement with up to 15 % RG maintained suitable workability and stability, modifying the hydration kinetics slightly, while promoting a denser microstructure.

3.2 Cement mortars with red gypsum

The performance of cement mortars containing red gypsum (RG) was assessed in terms of workability, porosity and mechanical properties. The mortars were prepared with 5 %, 10 %, and 15 % replacement of cement by RG at a constant water-to-binder ratio (w/c = 0.5).

3.2.1 Workability and porosity

The results demonstrated that the incorporation of RG reduced the workability of fresh mortars progressively, as indicated by the mini-slump spread decreasing from 165 mm for the reference mixture to 157.5 mm, 117.5 mm, and 107.5 mm for 5 %, 10 %, and 15 % RG, respectively. The reduced flowability is attributed primarily to the increased water demand and higher surface area of the RG particles, which lower the effective water available for lubrication. The porosity measurements revealed a similar trend, with a slight reduction at 5 % RG (2.5 %) compared to the reference (3.0 %), followed by an increase to 3.5 % and 4.5 % at 10 % and 15 % RG. This suggests that small amounts of RG can improve packing density, while higher levels introduce additional voids due to the altered rheology and air entrainment.

3.2.2 Mechanical properties

The compressive and flexural strength of cement mortars with red gypsum (RG) after 1, 7 and 28 days are shown in Figures 1 and 2. A small RG addition (5 %) enhanced both strengths slightly, while higher contents reduced them. After one day, the reference mix reached 30.57 MPa and the 5 % RG sample achieved a slightly higher value (33.59 MPa) due to accelerated early hydration. At 7 days, the 5 % RG mortar attained 52.92 MPa, exceeding the reference (48.96 MPa), whereas 10 % and 15 % RG reduced the strength to 42.34 MPa and 34.27 MPa. After 28 days, the 5 %

RG mixture maintained the best performance (61.56 MPa) compared to the reference (58.70 MPa), while the 10 % and 15 % RG dropped to 47.66 MPa and 38.75 MPa. The flexural strength followed the same pattern: 7.73 MPa for 5 % RG versus 7.5 MPa for the control, decreasing to 6.5 MPa and 5 MPa for 10 % and 15 % RG. Overall, a 5 % replacement level provides a beneficial micro-filling and nucleation effect, whereas higher RG contents cause dilution, greater porosity and loss of strength.

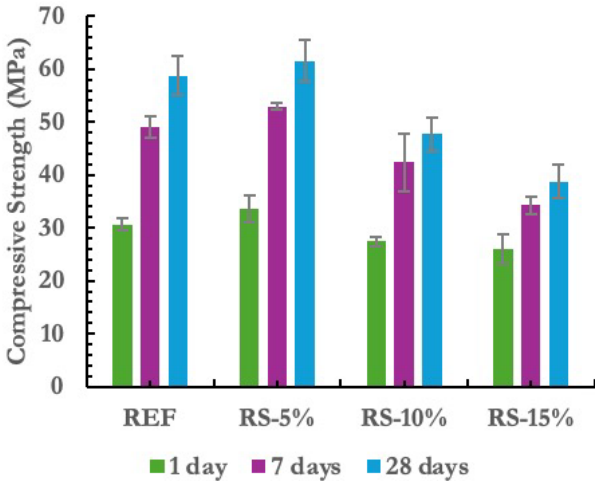

Figure 1: Compressive strength of cement composites after 1, 7, and 28 days.

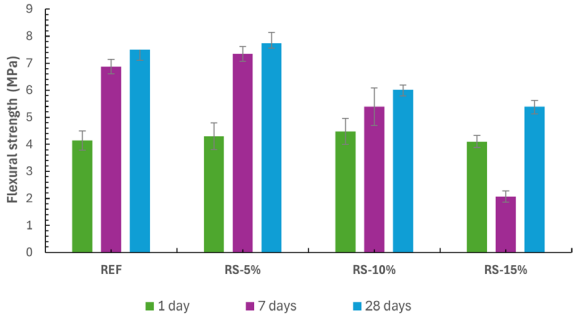

Figure 2: Flexural strength of cement composites after 1, 7, and 28 days.

The influence of red gypsum (RG) content and curing time on the mechanical behaviour of cement mortars was analysed further using Response Surface Methodology (RSM), as illustrated in Figures 3 and 4.

The 3D surface and contour plots show the nonlinear relationship between the RG percentage, curing duration, and the resulting compressive and flexural strengths. The models revealed that both properties initially increased with small additions of RG, reaching optimal values at approximately 5 %, followed by a gradual decline at higher replacement levels. This trend indicates a beneficial micro-filling and nucleation effect at low RG contents, enhancing early hydration and matrix densification, while excessive RG introduces dilution and increased porosity that weaken the composite structure. The curvature of the response surfaces also confirms that the development of mechanical strength is strongly time-dependent, with more pronounced differences observed after extended curing periods. The RSM analysis thus captured the combined and interactive effects of RG dosage and curing time effectively, allowing identification of an optimal composition range for achieving the best mechanical performance while maintaining mix stability.

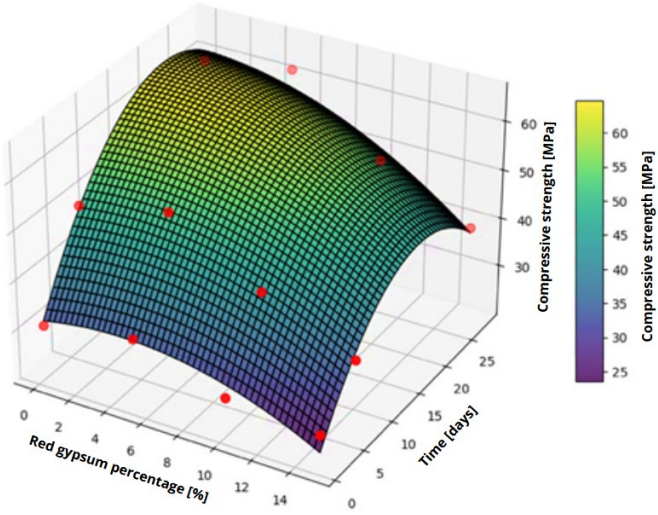

Figure 3: RSM visual representation of the effects of red gypsum content (%) and curing time (days) on compressive strength (MPa).

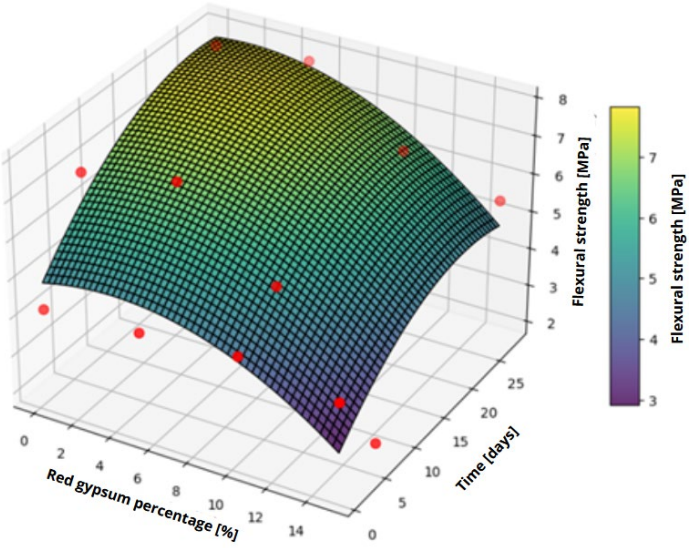

Figure 4: RSM visual representation of the effects of red gypsum content (%) and curing time (days) on flexural strength (MPa).

3.3 Geopolymers with red gypsum

Red gypsum (RG) was also evaluated as a partial replacement for metakaolin in geopolymer composites, to assess its effect on the workability and mechanical performance. As RG contains mainly calcium sulphate with limited aluminosilicate reactivity, its incorporation can influence geopolymerisation and matrix formation. This section examines how varying the RG contents (0–50 %) and activator ratios (Na_2SiO_3 : NaOH = 2 : 1 and 1 : 1) affect the fresh and hardened properties of geopolymer mixtures.

3.3.1 Workability and Porosity

All the geopolymer mixtures were designed using metakaolin (MK) as the main aluminosilicate precursor, replaced partially by 0–50 % of red gypsum (RG). High-alkali activating solutions composed of sodium silicate (Na_2SiO_3) and sodium hydroxide (NaOH) were used at ratios of 2 : 1 and 1 : 1. During mixing, it was observed that small additions of RG (up to 10 %) did not alter the consistency significantly, and the mixtures retained satisfactory workability suitable for

moulding. However, as the RG content increased to 25 % and 50 %, the mixtures became noticeably stiffer, less cohesive and more difficult to compact, even with the increased liquid content. This was attributed to the inert nature of RG, its high sulphate content and limited aluminosilicate reactivity, which hindered the geopolymer gel formation and reduced binder cohesion. Additionally, higher RG levels led to a more open and porous structure, as confirmed by the visual and mechanical observations, indicating that excessive RG disrupts the packing and continuity of the geopolymer matrix.

3.3.2 Mechanical Properties

The compressive and flexural strengths of metakaolin-based geopolymers incorporating red gypsum (RG) are shown in Figures 5 and 6. The results revealed a pronounced decrease in both strengths with increasing RG replacement. After 7 days of curing at 60 °C, the reference mixture without RG reached a compressive strength of 20.63 MPa, while the 10 % RG sample achieved 13.49 MPa, the 25 % RG sample dropped to 2.66 MPa, and the 50 % RG mixture showed almost no load-bearing capacity (0.01 MPa). A similar trend was observed for the second activator ratio, where the compressive strength values were 21.09 MPa (0 % RG), 19.01 MPa (10 % RG), 11.25 MPa (25 % RG), and 0.95 MPa (50 % RG).

The flexural strength results followed the same pattern, decreasing sharply with the higher RG contents. For the Na_2SiO_3 : NaOH = 2 : 1, (60 °C) system (B1 mixes), the flexural strength declined from 6.00 MPa (0 % RG) to 4.75 MPa (10 %), 2.80 MPa (25 %), and 0.60 MPa (50 %). In the Na_2SiO_3 : NaOH = 1 : 1 (B2 mixes), the values were slightly higher at each corresponding RG level: 6.00 MPa, 5.10 MPa, 3.00 MPa, and 1.00 MPa, respectively.

These findings indicate that small RG additions (≈ 10 %) may still act as an inert filler, allowing acceptable mechanical performance, while higher replacement levels disrupt the geopolymerisation process significantly. The decline in strength at ≥ 25 % RG confirms that the limited aluminosilicate reactivity and high sulphate content of RG hinder gel formation and lead to a porous, poorly bonded microstructure.

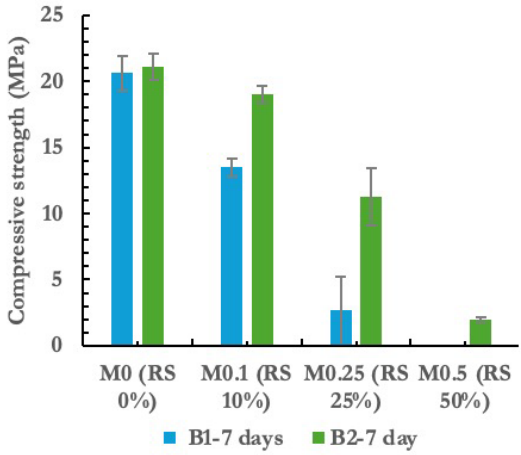

Figure 5: Compressive strength of geopolymer samples with metakaolin replaced partially by RG from 0% to 50%.

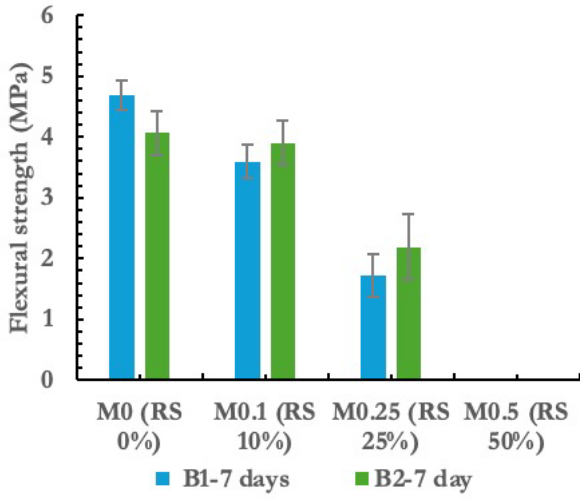

Figure 6: Flexural strength of geopolymer samples with metakaolin replaced partially by RG from 0% to 50%.

4 Conclusion

This research confirmed that industrial red gypsum (RG) can be valorised effectively as a secondary material in cement-based systems, with partial potential in geopolymer formulations. In cement pastes and mortars, RG additions up to about

5 % improved the matrix density and mechanical performance through filler and nucleation effects, while maintaining good dimensional stability. Higher RG contents increased the porosity and water demand, resulting in reduced strength and workability. The RSM analysis verified further that the optimum balance between compressive and flexural strength occurs at low RG replacement levels and longer curing times.

In geopolymer composites, the incorporation of RG limited geopolymerisation due to its low aluminosilicate reactivity, causing a rapid strength decline beyond 10 % replacement. Despite this, minor RG additions may serve as inert fillers or stabilisers within the alkali-activated matrix.

Overall, the study demonstrates that controlled use of red gypsum—particularly in low concentrations within cementitious systems—can support sustainable construction practices by reducing cement consumption, minimising industrial waste disposal, and advancing circular material use in the building sector. Nevertheless, the leaching behaviour of RG should be evaluated thoroughly prior to practical implementation, to ensure environmental safety and compliance with the regulatory Standards.

Acknowledgment

The authors acknowledge Cinkarna Celje d.d. for funding this industrial research project fully. The first author is a member of the research programme P2-0046, supported by the Slovenian Research and Innovation Agency (ARIS).

References

Al-Hammood, A. A., Frayyeh, Q. J. & Abbas, W. A. (2021). Raw bentonite as supplementary cementitious material – a review. *Journal of Physics: Conference Series*, *1795*(1), 012018. https://doi.org/10.1088/1742-6596/1795/1/012018

Calderoni, D., Gastaldi, D., Merlo, V., Pellino, L., Canonico, F. & Contrafatto, L. (2024). Etna volcanic ash as new sustainable supplementary cementitious material. *Journal of Building Engineering*, *95*, 110264. https://doi.org/10.1016/J.JOBE.2024.110264

Castillo, H., Collado, H., Droguett, T., Sánchez, S., Vesely, M., Garrido, P. & Palma, S. (2021). Factors Affecting the Compressive Strength of Geopolymers: A Review. *Minerals 2021, Vol. 11, Page 1317*, *11*(12), 1317. https://doi.org/10.3390/MIN11121317

Das, S., Saha, P., Prajna Jena, S. & Panda, P. (2022). Geopolymer concrete: Sustainable green concrete for reduced greenhouse gas emission – A review. *Materials Today: Proceedings*, *60*, 62–71. https://doi.org/10.1016/J.MATPR.2021.11.588

Environment, U., Scrivener, K., … V. J.-C. and concrete & 2018, undefined. (n.d.). Eco-efficient cements: Potential economically viable solutions for a low-CO_2 cement-based materials industry. *ElsevierUN Environment, KL Scrivener, VM John, EM GartnerCement and Concrete Research, 2018•Elsevier*. Retrieved October 27, 2025, from https://www.sciencedirect.com/science/article/pii/S0008884618301480

Fode, T. A., Chande Jande, Y. A. & Kivevele, T. (2023). Effects of different supplementary cementitious materials on durability and mechanical properties of cement composite – Comprehensive review. *Heliyon*, *9*(7), e17924. https://doi.org/10.1016/J.HELIYON.2023.E17924

Hamada, H., Thomas, B., … F. Y.-J. of B. & 2021, undefined. (n.d.). Sustainable use of palm oil fuel ash as a supplementary cementitious material: A comprehensive review. *ElsevierHM Hamada, BS Thomas, FM Yahaya, K Muthusamy, J Yang, JA Abdalla, RA HawilehJournal of Building Engineering, 2021•Elsevier*. Retrieved October 27, 2025, from https://www.sciencedirect.com/science/article/pii/S235271022100142X

Huang, Y., Huo, Z., Ma, G., Zhang, L., Wang, F. & Zhang, J. (2023). Multi-objective optimization of fly ash-slag based geopolymer considering strength, cost and CO_2 emission: A new framework based on tree-based ensemble models and NSGA-II. *Journal of Building Engineering*, *68*, 106070. https://doi.org/10.1016/J.JOBE.2023.106070

Jhatial, A. A., Nováková, I. & Gjerløw, E. (2023). A Review on Emerging Cementitious Materials, Reactivity Evaluation and Treatment Methods. *Buildings 2023, Vol. 13, Page 526*, *13*(2), 526. https://doi.org/10.3390/BUILDINGS13020526

Jiju, A. (2023). *Design of Experiments for Engineers and Scientists* - (M. Malloy, Ed.; third). Matthew Deans. https://books.google.si/books?hl=en&lr=&id=cmilEAAAQBAJ&oi=fnd&pg=PP1&dq=design+of+experiment+materials+science&ots=uKNFQpgmoQ&sig=ouM1yKkIhPaS_soP24Ew4yK62pA&redir_esc=y#v=onepage&q=design%20of%20experiment%20materials%20science&f=false

Ju, J., Feng, Y., Li, H. & Xu, C. (2023). Resource utilization of strongly acidic wastewater and red gypsum by a harmless self-treatment process. *Process Safety and Environmental Protection*, *172*, 594–603. https://doi.org/10.1016/J.PSEP.2023.02.067

Kravanja, G. & Knez, Ž. (2023). Carbonization of Class G well cement containing metakaolin under supercritical and saturated environments. *Construction and Building Materials*, *376*, 131050. https://doi.org/10.1016/J.CONBUILDMAT.2023.131050

Lingyu, T., Dongpo, H., Jianing, Z. & Hongguang, W. (2021). Durability of geopolymers and geopolymer concretes: A review. *Reviews on Advanced Materials Science*, *60*(1), 1–14. https://doi.org/10.1515/RAMS-2021-0002/ASSET/GRAPHIC/J_RAMS-2021-0002_FIG_015.JPG

Podnar, T. M., Knez, Ž. & Kravanja, G. (2025). Enhancing strength and CO_2 uptake in lignite-based fly ash geopolymer mortar through supercritical carbonation. *The Journal of Supercritical Fluids*, *225*, 106695. https://doi.org/10.1016/J.SUPFLU.2025.106695

Rashad, A. M., Bai, Y., Basheer, P. A. M., Milestone, N. B. & Collier, N. C. (2013). Hydration and properties of sodium sulfate activated slag. *Cement and Concrete Composites*, *37*(1), 20–29. https://doi.org/10.1016/J.CEMCONCOMP.2012.12.010

Sotiriadis, K., Kiyko, P. I., Chernykh, T. N. & Kriushin, M. V. (2024). Self-cleaning ability of gypsum-cement-pozzolan binders based on thermally processed red gypsum waste of titanium oxide manufacture. *Journal of Building Engineering*, *87*, 109009. https://doi.org/10.1016/J.JOBE.2024.109009

Thomas, B. S., Yang, J., Mo, K. H., Abdalla, J. A., Hawileh, R. A. & Ariyachandra, E. (2021). Biomass ashes from agricultural wastes as supplementary cementitious materials or aggregate replacement in cement/geopolymer concrete: A comprehensive review. *Journal of Building Engineering*, *40*, 102332. https://doi.org/10.1016/J.JOBE.2021.102332

Xie, Z. ;, Liu, X. ;, Zhang, Z. ;, Wei, C. ;, Gu, J., Xie, Z., Liu, X., Zhang, Z., Wei, C. & Gu, J. (2024). Application of the Industrial Byproduct Gypsum in Building Materials: A Review. *Materials 2024, Vol. 17, Page 1837*, *17*(8), 1837. https://doi.org/10.3390/MA17081837

Zhang, Q. & Ye, G. (2012). Dehydration kinetics of Portland cement paste at high temperature. *Journal of Thermal Analysis and Calorimetry*, *110*(1), 153–158. https://doi.org/10.1007/S10973-012-2303-9

The Influence of Processed Steel Slag Additive on Brick-Making Clay

Mojca Loncnar,[1] Sara Tominc,[2] Lea Žibret,[2]
Maruša Mrak,[2] Vilma Ducman[2]

[1] SIJ Acroni, Jesenice, Slovenia
mojca.loncnar@acroni.si
[2] Slovenian National Building and Civil Engineering Institute, Ljubljana, Slovenia
sara.tominec@zag.si, lea.zibret@zag.si, marusa.mrak@zag.si, vilma.ducman@zag.si

DOI
https://doi.org/10.18690/um.fkkt.1.2026.5

ISBN
978-961-299-130-2

As clay deposits become scarce, the brick industry is increasingly seeking additives or substitutes. This study investigates a high-plasticity clay that requires an opening agent, for which was used 10 wt.% of processed steel slag Ekominit S1. Ceramic-technological tests were performed to determine the compressive strength, density and porosity. The addition of Ekominit S1 increased the total porosity by 5% in samples fired at 950 °C, and by 4% in samples fired at 1050 °C, while the compressive strength decreased by 36% in the samples fired at 950 °C and by 38% in those fired at 1050 °C compared to the reference material. Although the mechanical properties were lower than those of the reference, the benefit is reduced shrinkage. The processed steel slag could be incorporated successfully into bricks, which would also reduce the environmental impact of this sector by using secondary products instead of virgin materials.

Keywords:
clay bricks,
compressive strength,
opening agent,
porosity,
steel slag

University of Maribor Press

1 Introduction

As clay deposits vary in scarcity, this sector is searching constantly for potential additives or alternatives to clay. Some additives simply replace virgin clay and conserve resources, while others may have a positive effect on the process or product. When evaluating various wastes for their usability in the clay-based sector, the following parameters are important: chemical and mineralogical compositions, and the particle size of the additives.

In terms of mineralogical composition, the amount of quartz is particularly important, as it affects both the product properties and the drying process by reducing sensitivity. It also influences firing, where the phase transformation of quartz at 573 °C should be considered during the cooling phase, as it is associated with volumetric changes and can lead to cracking of the products if the cooling process is not managed properly. The carbonate content, if dispersed finely, can be as high as 20–25%; only lime inclusions larger than 1 mm can pose a problem (Ducman & Kopar, 2007, Baksa et al., 2018).

Various wastes have already been introduced successfully into the clay-based sector, including wastewater treatment sludges (Detho et al., 2024), paper sludge (Mohd Tajri and Hashim, 2025), ashes (Muñoz et al., 2023) and sediments. For the same type of clay investigated in the present paper, Božič et al.`s (2023) studied untreated Drava River sediment as a clay substitute for fired bricks, and showed that, despite reduced compressive strength, the pilot-scale bricks met all the regulatory requirements. Marine sediments are another potential material, but their chloride content can affect the brick properties negatively. Baksa et al. (2018) evaluated marine sediments from the Port of Koper, again with the same type of clay, and found them only conditionally suitable as a raw material, as they show excessive drying and firing shrinkage and high water absorption. These drawbacks can be mitigated by incorporating suitable additives, such as virgin clay or compatible waste materials. Various slags have also been investigated; Shih et al. (2004) found that slag addition reduced the required firing temperature. When the firing temperature exceeded 1050 °C and the slag content was below 10%, the bricks met the ROC National Standard CNS 3319 for third-class building bricks. As the slag content increased, quartz and kaolin decreased in the sintered samples, while magnesium aluminium silicate and calcium silicate increased. No new crystal phases were

observed. In another study, Freitas et al. (2021) reported high substitution rates (up to 50%) of clay with iron ore concentrate tailings (IOT) and basic oxygen furnace (BOF) steel slag. The results confirmed that a high level of clay substitution with IOT and BOF slag can be used together to produce fired clay bricks, but some adjustments are necessary. To avoid cracking, the particle size should be adjusted, and changes in the heating and cooling stages of the firing process are recommended. Depending on the type of slag, its addition to the brick-making clay can have varying degrees of beneficial influence (Gencel et al., 2021).

The aim of this study is to evaluate the potential of processed steel slag Ekominit S1 as an additive to brick-making clay, and to assess its influence on key properties such as shrinkage, water absorption and compressive strength. Furthermore, the study enhances the understanding of these effects through detailed phase and microstructural analyses (XRD, SEM, and MIP).

2 Materials and methods

2.1 Raw material

Steel slag is the main solid co-product of steel production, accounting for about 90% by mass. Electric arc furnace (EAF) slag from stainless steel production and ladle slag from secondary metallurgical processes for stainless and carbon steel were mixed, stabilised in the slag cooling yard, and processed further on the slag processing line. The resulting products are steel granulate, which is returned to the EAF, and the mineral product Ekominit S1, which was the material investigated in this study. The reference brick-making mixture was provided by the brick factory Goriške opekarne, located in western Slovenia. It consists of marl (50 wt%), clay (48 wt%), and coal powder (2 wt%) (Žibret et al., 2025).

2.2 Sample preparation

To evaluate the influence of Ekominit S1 as an additive in clay brick production, 10 wt.% Ekominit S1 was added to a clay sample, and the mixtures were fired at 950 °C and 1050 °C (Figure 1).

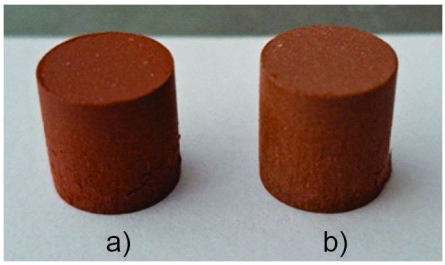

Figure 1: (a) Brick-making clay, and (b) clay with 10 wt.% Ekominit S1 after firing at 1050 °C. Source: own.

The brick samples were ground to a particle size below 63 μm, pressed at 150 MPa with the addition of 4% moisture, and sintered in an HLF 100 laboratory furnace (Protherm) at 950 °C and 1050 °C for 2 hours, using heating and cooling rates of 150 °C/h.

2.3 Test procedures

The particle size distribution (PSD) of the raw materials (slag and clay samples) was determined by laser diffraction granulometry using a Sync+Flow-Sync laser grain size analyser (Microtrack MRB). The clay was measured with distilled water, while the slag was dispersed in isopropanol. The PSD of the raw materials is shown in Figure 2.

Before the chemical analysis the samples were dried to a constant mass in a laboratory oven at 105 °C, and ground to pass through a 125 μm sieve. The loss on ignition (LOI) of the raw materials was determined at 950 °C, according to the EN 196-2:2013 Standard. The chemical composition of the materials was determined using an ARL PERFORM'X sequential X-ray fluorescence (XRF) spectrometer (Thermo Fisher Scientific Inc., Ecublens, Switzerland) with UniQuant 5 software (Thermo Fisher Scientific Inc., Waltham, MA, USA). The analysis was performed on melted discs, prepared by melting a mixture of the ignited sample and Fluxana (Li-tetraborate and Li-metaborate mixed in a mass ratio of 1:1) at a ratio of 1:10. LiBr (aq) (50 mL H_2O and 7.5 g LiBr (s) from Sigma Aldrich) was added to the mixture to avoid gluing the melt to the Pt crucible.

The compressive strength was measured using a ToniPRAX compressive strength testing machine (ToniTechnik, Berlin, Germany) at a loading rate of 1.2 kN/s.
The shrinkage was determined by measuring the change in the pellet diameter before and after sintering. The diameter of each pressed pellet was measured with a digital calliper (±0.01 mm) before firing (d_0). After sintering at 950 °C and 1050 °C and cooling to room temperature, the final diameter (d_f) was measured using the same method. The shrinkage was calculated following the approach of Xu et al. (2025) using Equation (1):

$$\text{Shrinkage (\%)} = [(d_0 - d_f)/d_0] \times 100 \quad (1)$$

Small representative pellets with a diameter and height of 10 mm were analysed for their porosity and pore size distribution directly after sintering using the Micromeritics® Autopore IV 9500 instrument (Micromeritics, Norcross, GA, USA).

X-ray powder diffraction of the clay fired at 950 °C and 1050 °C, as well as clay containing 10 wt.% Ekominit S1 fired at the same temperatures, was conducted using a PANalytical X'Pert Pro X-ray powder diffractometer equipped with CuKα1 radiation (Johannson Ge (111) incident beam monochromator) and an X'Celerator detector at 45 kV and 40 mA. The samples were prepared by back-loading the powder into a circular sample holder with a diameter of 16 mm to minimise the preferred orientation effects. The measurements were taken in a 2θ range of 5–70° with a step size of 0.013° 2θ, using a 1° divergence slit and a 15 mm mask. Rietveld refinement was performed using the PANalytical X'Pert High Score Plus diffraction software (version 4.9), utilising structures for the phases from the ICDD PDF 4+ 2021 RDB powder diffraction files.

The microstructure and elemental composition (as a complementary method to confirm XRD) of the brick samples were examined using a JEOL IT500 HV Scanning Electron Microscope (SEM) equipped with an Energy Dispersive X-ray Spectrometer (EDS). The samples were cast in epoxy resin, dry polished, and coated with an approximately 17 nm thick layer of carbon.

3 Results and discussion

3.1 Raw material

Ekominit S1 is composed mainly of the oxides of calcium, iron, silicon and magnesium (Table 1). It is a fine-grained material with particle sizes mostly below 0.1 mm (Figure 2). The main minerals are C_2S, merwinite, periclase, ferrite and mayenite (Loncnar et al., 2025). Brick-making clay from regular brick production was used as a reference material. It contained illite/muscovite, chlorite, kaolinite, feldspars, calcite and quartz (Božič et al., 2023, Žibret et al., 2025).

Table 1: Chemical composition of the brick-making clay and Ekominit S1 (determined by XRF analysis, in wt.%)

	Brick-making clay	Ekominit S1
LOI 950 °C	8.9	7.5
Na_2O	0.8	0.0
MgO	1.7	14.0
Al_2O_3	16.5	10.2
SiO_2	59.4	18.3
P_2O_5	0.1	0.1
SO_3	0.0	0.3
K_2O	2.3	0.0
CaO	3.2	36.9
TiO_2	0.7	0.6
V_2O_5	0.0	0.1
Cr_2O_3	0.0	2.8
MnO	0.2	1.6
Fe_2O_3	6.0	7.2
Others	0.2	0.4

Source: own.

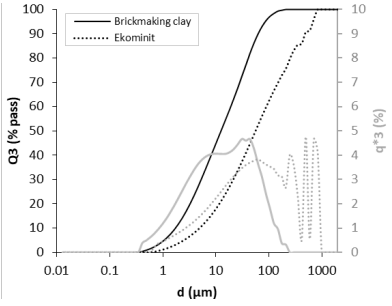

Figure 2: Particle size distribution of the Ekominit S1 and brick-making clay.
Source: own.

3.2 Evaluation after firing

The mechanical properties, shrinkage, density, and porosity were evaluated after firing at selected temperatures. The results show that adding 10 wt.% Ekominit S1 increased the total porosity of the samples fired at both temperatures. At 950 °C the porosity increased from 21.2% for the reference clay to 25.9% with the Ekominit S1. The lowest measured porosity was for the clay sample fired at 1050 °C (18.8%), which also exhibited the highest mechanical strength and density. With the addition of Ekominit S1, the porosity increased to 25.5%. A similar trend was observed at 1050 °C, where the reference sample had the lowest porosity of all the tested compositions (18.8%), while the Ekominit S1-containing sample reached 25.5% (Table 2). These changes are consistent with the mercury intrusion porosimetry (MIP) results shown in Figure 3, confirming the porosity-enhancing effect of Ekominit S1.

Table 2: Bulk density and porosity, measured with MIP, and compressive strength and shrinkage of samples fired at 950 and 1050 °C.

	Temperature (°C)	Brick-making clay	Clay with 10 wt.% Ekominit S1
Bulk density (g/cm^3)	950	2.1	2.0
	1050	2.2	2.0
Porosity (%)	950	21.2	25.9
	1050	18.8	25.5
Shrinkage (%)	950	2.0	1.0
	1050	3.9	2.0
Compressive strength (MPa)	950	235.2 ± 10.3	151.5 ± 12.7
	1050	261.2 ± 11.6	161.9 ± 4.0

Source: own.

The bulk density remained comparable between the samples, showing only a slight decrease with the addition of Ekominit S1 at both temperatures (Table 2), which reflects the increased open porosity. The shrinkage values also decreased in the presence of Ekominit S1, from 2.0% to 1.0% at 950 °C and from 3.9% to 2.0% at 1050 °C. The reduced shrinkage suggests that the additive limits densification during firing and acts as an opening agent (Ducman & Kopar, 2007), indicating that Ekominit S1 could replace quartz in the clay brick mixture.

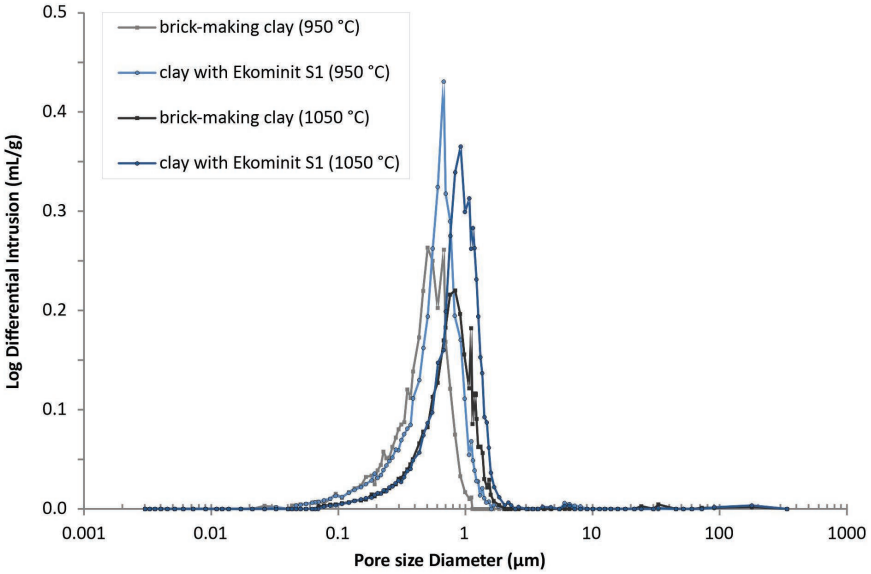

Figure 3: Pore size distribution of brick-making clay and clay sample with 10 wt.% of Ekominit S1, fired at 950 and 1050 °C.

Source: own.

The mechanical properties followed the expected relationship with the porosity (Figures 3 and 4). The reference clay samples, particularly those fired at 1050 °C, exhibited the highest compressive strength (261.2 MPa), consistent with their lower porosity. In contrast, the samples containing Ekominit S1 showed reduced compressive strength at both temperatures (151.5 MPa at 950 °C and 161.9 MPa at 1050 °C), corresponding to their higher porosity values.

Overall, the results indicate that Ekominit S1 increases porosity while reducing shrinkage and mechanical strength.

XRD analysis identified the following major phases: quartz, hematite, feldspar, an amorphous phase, and periclase as a minor phase (Figure 5). The quantitative results are presented in Table 3, which shows that the phase composition of the brick-making clay and the clay with the addition of 10 wt.% Ekominit S1 varied with the firing temperature and slag addition.

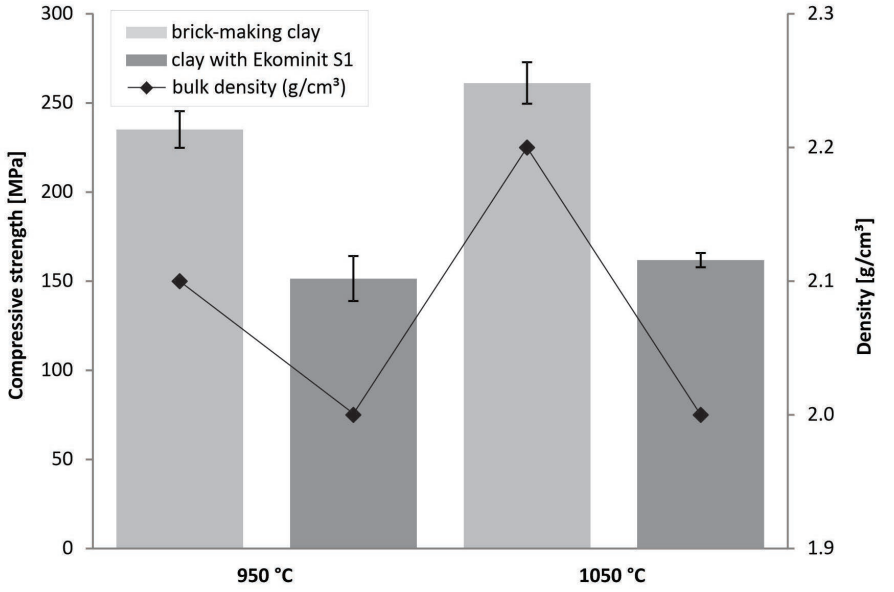

Figure 4: Compressive strength and density of brick-making clay and clay with the addition of 10 wt.% of Ekominit S1 after firing at 950 °C and 1050 °C.

Source: own.

Table 3: Main phase composition of brick-making clay fired at 950 °C and 1050 °C, and clay with the addition of 10 wt.% Ekominit S1, fired at 950 °C and 1050 °C.

	Temperature (°C)	Brick-making clay	Clay with 10 wt.% Ekominit S1
Quartz	950	36.3	41.0
	1050	35.5	26.7
Hematite	950	10.4	9.9
	1050	11.1	10.8
Feldspar	950	9.8	8.7
	1050	18.4	24.2
Amorphous	950	42.7	40.4
	1050	34.9	37.4

Source: own.

For pure clay, increasing the firing temperature from 950 °C to 1050 °C decreased the quartz content slightly (from 36.3 to 35.5 wt.%) and the amorphous phase (from 42.7 to 34.9 wt.%), while promoting feldspar crystallisation (from 9.8 to 18.4 wt.%) and increasing the hematite slightly (from 10.4 to 11.1 wt.%). This indicates that higher temperatures facilitate the transformation of amorphous material into

crystalline phases, particularly feldspar, consistent with enhanced fluxing and partial melting. The addition of 10 wt.% Ekominit S1 also resulted in different phase evolution. At 950 °C, quartz content increased slightly (from 36.3 to 41 wt.%), while the feldspar decreased slightly (from 9.8 to 8.7 wt.%). At 1050 °C, the Ekominit S1 addition promoted feldspar formation (from 18.4 to 24.2 wt.%) while decreasing quartz (from 35.5 to 26.7 wt.%). The amorphous content in the mixture remained slightly higher than in pure clay (37.4 wt.% vs 34.9 wt.%), suggesting that the slag stabilises part of the glassy phase at elevated temperatures. Overall, Ekominit S1 acts as a flux, accelerating the feldspar crystallisation at high temperatures while modifying the balance between the crystalline and amorphous phases, which could influence the sintering behaviour and final properties of the fired material.

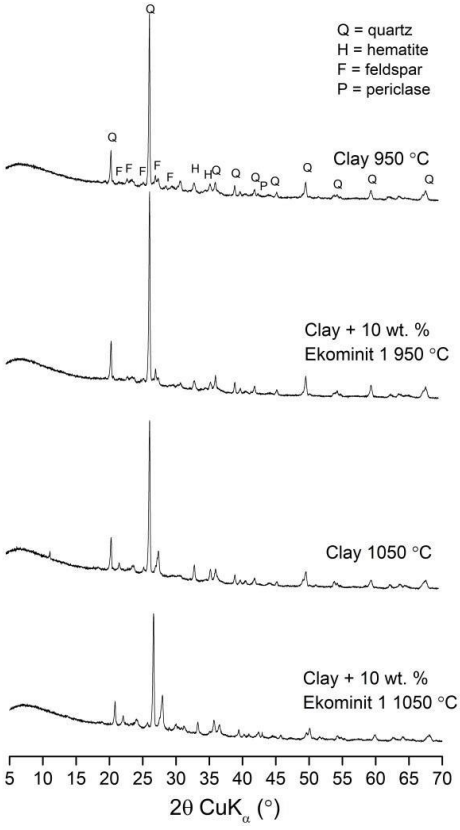

Figure 5: X-ray diffraction patterns of brick-making clay fired at 950 °C and 1050 °C, and clay with the addition of 10 wt.% Ekominit S1, fired at 950 °C and 1050 °C.

Source: own.

Further microstructural evaluation confirmed the presence of the phases identified by XRD, with feldspars enriched in K (K-feldspars) (Figure 6). At both firing temperatures, the porosity was higher in the mixtures containing 10 wt.% Ekominit S1 than in the pure clay bricks. Additionally, the SEM images show a reduction in matrix porosity with the increased firing temperature, resulting in larger pore diameters. This is consistent with the MIP results, which indicate that the pore diameter for samples fired at 1050 °C shifted to higher values (Figure 3).

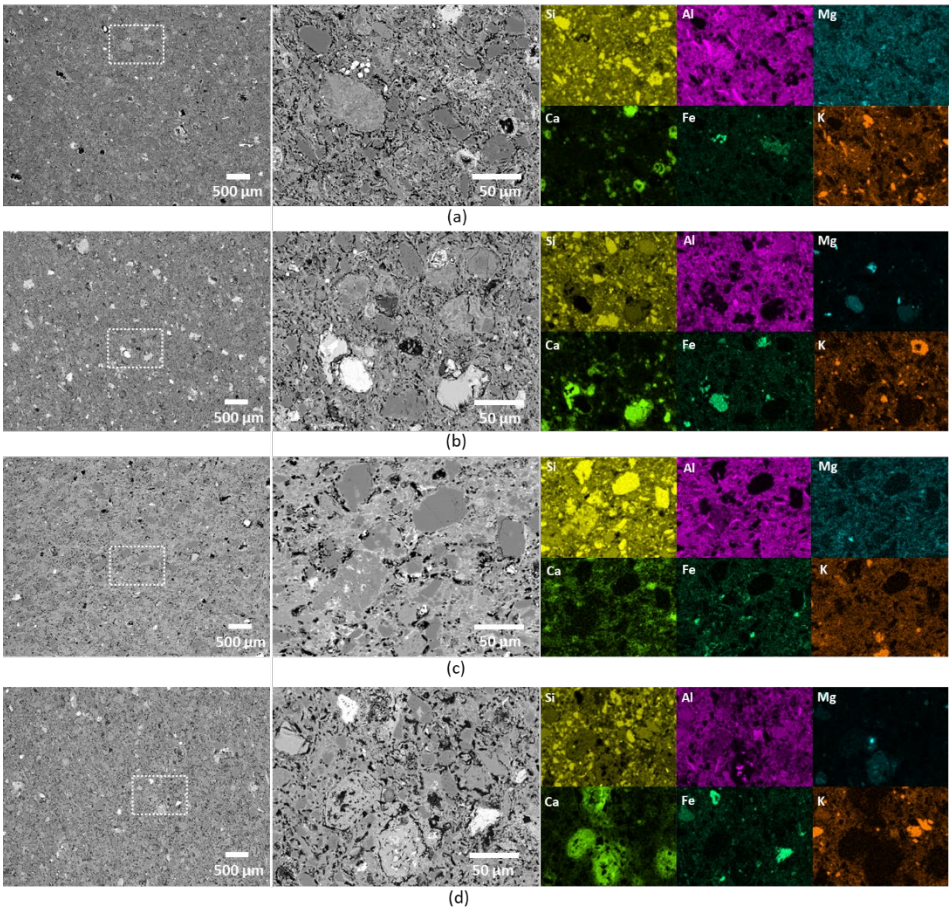

Figure 6: SEM images and EDS elemental maps of Si, Ca, Al, Fe, Mg, and K for the laboratory brick samples, where (a) is pure clay fired at 950 °C, (b) is clay with 10 wt% Ekominit S1 fired at 950 °C, (c) is pure clay fired at 1050 °C, and (d) is clay with 10 wt% Ekominit S1 fired at 1050 °C.

Source: own.

4 Conclusions

The investigated clay is classified as high-plasticity clay and requires the addition of an opening agent, in this case Ekominit S1. Adding Ekominit S1 (up to 10 wt.%) reduced the density, which, consequently, led to decreased mechanical properties. However, the beneficial effect of Ekominit S1 is the reduction in shrinkage, which is important from a technological perspective.

In regular production an extrusion process is used, and, as hollow bricks are produced, the compressive strength of laboratory-made samples cannot be compared directly with that of regular production. Nevertheless, the study showed that processed steel slag can be incorporated into bricks, reducing the environmental impact of both sectors by using secondary products instead of virgin materials. The next step should be pilot production at the brick-making company, which will provide a comprehensive insight into the additive's impact on the process and final properties.

Acknowledgment

This research was funded by the European Union under the KIC GEORIS project – Innovative technologies for waste processing in the ESEE region (Grant number 21107) and the Research Programme P2–0273 "Building structures and materials".

References

Baksa,P., Cepak, F., Kovačič Lukman, R., Ducman, V. (2018). Evaluation of Marine Sediments in Terms of their usability in the Brick Industry: Case Study Port of Koper. *Journal of Sustainable Development of Energy, Water and Environment Systems, 6* (1), 78-88. doi:10.13044/j.sdewes.d5.0183

Božič, M., Žibret, L., Kvočka, D., Mauko Pranjić, A., Gregorca, B., Ducman, V. (2023). Drava river sediment in clay brick production: Characterization, properties, and environmental performance. *Journal of Building Engineering 71*, 106470. doi:10.1016/j.jobe.2023.106470

Clewlow, R. R. (2016). Carsharing and sustainable travel behavior: Results from the San Francisco Bay Area. *Transport Policy, 51*, 158-164. doi:10.1016/j.tranpol.2016.01.013

Cussler, E. L. (2015). Diffusion in liquids. In M. L. McGraw & T. H. Chilton (Eds.), *Chemical engineering series* (pp. 45–78). McGraw-Hill

Detho, A., Kadir, A. A., Ahmad, S. (2024). Utilization of wastewater treatment sludge in the production of fired clay bricks: An approach towards sustainable development. *Results in Engineering, 21*, 101708. doi:10.1016/j.rineng.2023.101708

Ducman, V., Bizjak, K.F., Likar, B., Kolar, M., Robba, A., Imperl, J., Božič, M., Gregorc, B. (2022). Evaluation of Sediments from the River Drava and Their Potential for Further Use in the Building Sector. *Materials 15*(12), 4303. doi:10.3390/ma15124303

Ducman, V. & Kopar, T. (2007). The influence of different waste additions to clay-product mixtures. *Materials and Technologies*, 41(6), 289-293. http://mit.imt.si/izvodi/mit076/ducman.pdf

Freitas, S. M. A. C., Sousa, L. N., Estevam, T., Martins, M. E., Asis, P. S. (2021). Manufacturing of fired clay brick with iron ore tailing and steel slag. *Revista Latinoamericana de Metalurgia y Materiales 41*(2), 139-148. https://www.rlmm.org/ojs-files/full_pdf/RLMM-2021-V41N2.pdf

Gencel, O., Munir, M. J.., Kazmi, S. M. C., Sutcu, M., Erdogmus, E., Velasco, P. M., Quesada, D. E.. (2021). Recycling industrial slags in production of fired clay bricks for sustainable manufacturing. *Ceramics International 47*(21), 30425-30438. doi:10.1016/j.ceramint.2021.07.222

Loncnar, M., Kriskova, L., Georgopoulos, C., Skentzou, D., Tesovnik, A., Ducman, V. (2025). GEORIS pavers - a small scale demonstration within the GEORIS project. *7th International Conference on Technologies & Business Models for Circular Economy: Conference proceedings*; *7*, 69-81. doi:10.18690/um.fkkt.1.2025.7

Mohd Tajri, M.H., Hashim, N. H. (2025). Performance Evaluation of Sludge - Added Clay Bricks, *Progress in engineering application and technology, 6*(2), 1-14. doi:10.30880/peat.2025.06.02.001

Muñoz, P., Letelier, V., Muñoz, L., Gencel, O., Sutcu, M., Vasic, M. (2023). Assessing technological properties and environmental impact of fired bricks made by partially adding bottom ash from an industrial approach. *Construction and Building Materials, 396*, 132338. doi:10.1016/j.conbuildmat.2023.132338

Shih, P.-H., Wu, Z.-Z., Chiang H.-L. (2004). Characteristics of bricks made from waste steel slag, *Journal of Waste Management, 24* (10), 1043-1047. doi:10.1016/j.wasman.2004.08.006

Žibret, L., Carević, I., Štirmer, N., Koloda, I., Vrčon Mihelj, M.., Kragelj, M., Ducman, V. (2025). Evaluation of the performance of clay-based bricks with the addition of co-combustion ash. *7th International Conference on Technologies & Business Models for Circular Economy: Conference proceedings*; *7*, 169-179. doi:10.18690/um.fkkt.1.2025.15

Xu, J., Shao, Y., Feng, X., Zhang, X., Li, H., Yang, J., Gao, F. (2025). Low sintering shrinkage porous ceramics: Principles, progress, and perspectives. *Journal of Advanced Ceramics, 14*(2), 9221015. doi:10.26599/JAC.2024.9221015

ASSESSMENT OF THE TECHNOLOGICAL FEASIBILITY AND ECONOMIC VIABILITY OF RESIDUE VALORISATION IN APPLE PROCESSING

KATJA MAKOVŠEK,[1] UROŠ NOVAK,[1] BLAŽ LIKOZAR,[1] ILJA GASAN OSOJNIK ČRNIVEC,[1] MIJA SEŽUN,[2] GREGOR LAVRIČ,[2] MATEJ FATUR,[3] LUKA JUVANČIČ[3]

[1] National Institute of Chemistry, Ljubljana, Slovenia,
katja.makovsek@ki.si, uros.novak@ki.si, blaz.likozar@ki.si, gasan.osojnik@ki.si
[2] Country Pulp and Paper Institute, Ljubljana, Slovenia
mija.sezun@icp-lj.si, gregor.lavric@icp-lj.si
[3] University of Ljubljana, Biotechnical faculty, Ljubljana, Slovenia
matej.fatur@bf.uni-lj.si, luka.juvancic@bf.uni-lj.si

Apple pomace, a major by-product of the apple processing industry, was assessed through two alternative valorisation pathways business models: pectin extraction for premium gelling sugar incorporation and fruit leather production. Both models were developed on pilot-scale based data and assessed through discounted cash flow analysis. Clustered pectin extraction (30 t/year capacity) demonstrates strong profitability (Net Present Value > €240,000, Internal Rate of Return > 100%). In contrast, single-farm scale processing and fruit leather production (6.6 t/year capacity) were economically viable only for/when targeting premium market segments. The integration of additional residue valorisation options, such as specialty paper production or ethanol regeneration, improved the overall sustainability and resource efficiency further. The findings confirm that small-scale circular approaches can drive economic resilience when focusing on high-value markets and employing systemic, resource-efficient design.

DOI
https://doi.org/10.18690/um.fkkt.1.2026.6

ISBN
978-961-299-130-2

Keywords:
apple pomace, pectin, paper, fruit leather, economic evaluation of the prototype, biomass residues, biomass side streams, biomass valorisation, sustainable business model

University of Maribor Press

1 Introduction

Apple pomace is produced globally at a rate of 4 million tonnes per annum, and is as such one of the most significant types of agri-food residues and waste (Kauser, 2024; Gołębiewska, 2022). Apples are by far the most important fruit species in the Slovenian agricultural output (about 50,000 tonnes yearly), which is used mainly for food as fresh fruit, and in the form of apple products such as apple juice, apple cider vinegar, dried apples, etc. Apple processing generates large amounts of apple pomace (estimated at about 1,200 tonnes of dry matter), which are usually processed into animal feed or compost. Apple pomace contains various high-value components, such as phenolic compounds (e.g. flavonoids, hydroxycinnamic acids or dihydrochalcones), dietary fibre and high pectin contents (Bhushan, 2008; Barreira, 2019). Most commonly, apple pomace contains abundant pectin and cellulose, between 9 and 20 % pectin and between 7 and 44 % cellulose, making apple pomace a potential source of pectin and cellulose (Costa, 2022; Ma, 2019).

The material flow balance conducted within the project "Circular technological concepts and business models in Slovenian agriculture (V4-2208; Juvančič, 2025)" confirmed the potential of apple pomace as a raw material source for further valorisation through cascading use. Two prototype systems were developed to assess the economic potential of apple pomace valorisation in Slovenia. The first prototype explored pectin extraction, with an option for the remaining extraction residue to be used subsequently to produce speciality papers. The second prototype focused on the production of fruit leather as a plant-based alternative to conventional animal leather.

The cascading valorisation of apple pomace has emerged as a showcase for farm-level circularity, lowering disposal costs and opening new revenue streams simultaneously. The technological prototypes have subsequently been translated into circular and sustainable business models that are transferable to the context of professional fruit-growing farms, or micro-enterprises engaging in these activities. Both concepts – pectin extraction and fruit leather production, intentionally target higher-end market segments, where eco-design and local provenance add differentiating value able to offset the limited raw-material base and higher unit cost typical of family farms (Juvančič, 2025).

2 Methods

In this article we focus on the process of transforming technological prototypes of agricultural by-product utilisation into functioning business models. In doing so, we follow the principle that business models can be used as supplementary activities on farms or small-scale processing plants in rural areas. In cooperation with the developers of the technological prototypes, we have translated the proposed technological solutions into a business model that describes the organisation of the business process, the technological parameters of production and the form of the economic entity. The scope of apple pomace utilisation was defined based on the inventory of production mass flows on Kastelic farm, which participated in the project. The analytical framework mirrors the stepwise approach described by Fatur et al. (Fatur, 2025), in which the prototype mass balances are first translated into cost items, and thereafter into discounted-cash-flow indicators:

- Technological prototype 1: Extraction of pectin, sales of pectinated sugar: For pectin extraction two capacity scenarios were evaluated 6.6 tonnes annually (single farm) versus 30 tonnes (cluster of farms).
- Technological prototype 2: Production of fruit leather: 6.6 tonnes of apple pomace per year were evaluated for fruit leather production.

The economic viability is gauged over ten years at a real 6 % discount rate, using straight-line depreciation for the resulting Net Present Value (NPV) and Internal Rate of Return (IRR). A qualitative discussion of the loop-closing options – either outsourcing the cellulose-rich residue to a niche paper mill, or fermenting it to regenerate extraction ethanol – followed the sustainability reasoning advanced in the second stage of the cascade.

3 Results

Two technological prototypes, with their technical specification, were developed for valorisation of the technological feasibility and economic viability of apple processing residue. Figure 1. represents the technical scheme of pectin extraction, used for the description of the technological prototype 1. This scheme was developed based on known experimental results from the literature, and was used for following economic evaluations.

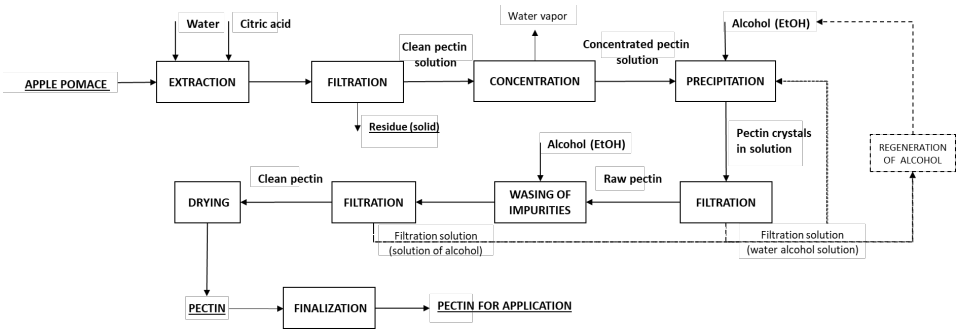

Figure 1: The technical scheme for the extraction of pectin (technological prototype 1).
Source: own, author: Katja Makovšek

Figure 2 represents the scheme for the second evaluated technological prototype, the production of fruit leather. The prototype was developed based on the previous projects.

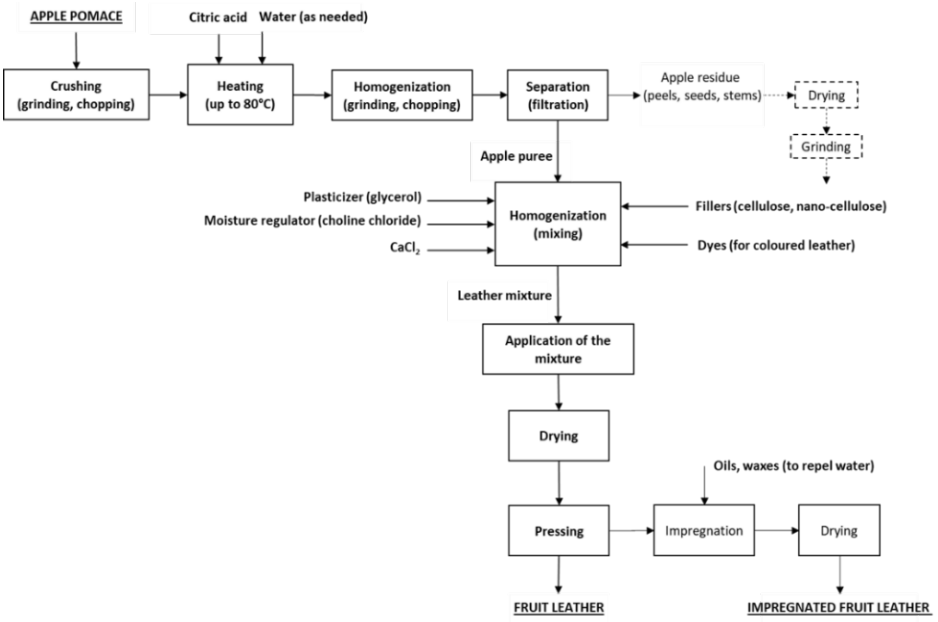

Figure 2: Prototype 1: Production of fruit leather (technological prototype 2).
Source: Fatur, 2025, author: Katja Makovšek

At the cluster farm scale (30 t annually), pectin extraction converts pomace into about 720 kg of high-methoxyl pectin, subsequently blended into 9,650 kg of premium gelling sugar. With a farm-gate price of 22.4 €/kg, the annual revenue reaches 216,000 €, while the variable costs are dominated by the ethanol purchases (≈ 109,000 €). A modest equipment set – an extractor, jacketed tanks and filtration – requires 19,500 €, complemented by a 15,500 € modular hall. Under these premises the own cost for pectin settles at 3.86 €/kg, the NPV attains 240,192 €, at the IRR 101 %, confirming strong viability when the raw material is pooled among several farms. Scaling the same technology down to 6.6 tonnes annually lifts the unit cost to 5.10 €/kg; the NPV shrinks to 17,695 € and the IRR to 15 %, making the profitability contingent on sustained premium pricing, as already noted for the pectinated sugar marketed through direct sales.

Table 1: Cash flow on two cases of production scale for pectin extraction on a farm level.

Farm scale	Cluster of farms 30 t/y	Small farm 6 t/y
Total Revenue (TR)	216,000 €	47,520 €
Total Costs (TC)	189,480 €	45,657 €
Differential cash flow	34,829 €	6,618 €
IRR	101%	15%
NPV	240,192 €	17,695 €

The fruit leather, produced from 6.6 tonnes of pomace blended with natural binders, yields roughly 1,200 kg of dehydrated fruit leather sheets. If priced at 60 €/kg in the eco-packaging niches the concept will generate 72,000 € annually against an own cost of 36.8 €/kg. With total costs amounting to 48,747 €, the NPV reaches 171,655 € and the IRR approaches 86 %. The result aligns with the general finding that high-margin, design-driven outlets are indispensable for small-scale circular ventures.

Table 2: Cash flow of apple leather production on a farm level.

Fruit leather	Production scale 6.6 t/y
Total Revenue (TR)	72,000 €
Total Costs (TC)	48,747 €
Differential cash flow	23,253 €
IRR	86%
NPV	171,655 €

The residual press-cake can either feed a niche paper line – incurring 1.20 €/kg of service cost as reported for specialty sheets – or undergo fermentation and distillation, recovering up to 60 % of the ethanol input and lowering the variable expenses further.

4 Conclusion

The study confirms that economic resilience hinges on premium positioning. Clustered pectin extraction leverages economies of scale to deliver an IRR above 100 %, whereas single-farm installations remain borderline profitable unless backed by strong branding. Fruit leather, though more speculative technologically, achieves attractive returns owing to favourable price–cost differentials and modest capital needs. In both cases, loop-closing options – be it cellulose-based paper for promotional use or in-house ethanol regeneration – enhance the circular performance and reinforce the storytelling potential that underpins market acceptance. The evidence thus supports the broader claim that circular products from agri-food by-products can succeed commercially when embedded in well-crafted, sustainability-oriented business narratives.

Acknowledgment

This work builds largely on findings developed within the project »Circular technological concepts and business models in Slovenian agriculture« (V4-2208), financed jointly by the Slovenian Research and Innovation Agency, and the Ministry for Agriculture, Forestry and Food.

References

Barreira J. C., Arraibi A. A., Ferreira I. C., (2019). Bioactive and functional compounds in apple pomace from juice and cider manufacturing: Potential use in dermal formulation. *Trends in Food Science & Technology, Volume 90,* p. 76-87.

Bolka, S., Fatur, M., Juvančič, L., Kavčič, S., Krt, K., Makovšek, K., Mihelič, R., Osojnik Črnivec, G.I., Schwarzmann, A., Sežun, M., Stojilković, B., Šutar, N. (2024). Predstavitev prototipov valorizacije stranskih proizvodov kmetijske proizvodnje. Fazno poročilo, Krožne tehnološke zasnove in poslovni modeli v slovenskem kmetijstvu (angl. Circular technological concepts and business models in Slovenian agriculture), V4-2208, Slovenian Research and Innovation Agency, Ljubljana, 87 pp.

Bhushan S., Kalia K., Sharma M., Singh B., Ahuja P. S., (2008). Processing of Apple Pomace for Bioactive Molecules. *Critical Reviews in Biotechnology, Volume 28*, p. 285–296.

Fatur, M., Bolka, S., Kavčič, S., Krt, K., Makovšek, K., Mihelič, R., Osojnik Črnivec, G.I., Schwarzmann, A., Sežun, M., Stojilković, B., Šutar, N., Juvančič, L. (2025). Prototipi valorizacije stranskih proizvodov v kmetijstvu: zasnove poslovnih modelov, presoja ekonomske upravičenosti in ocena okoljske trajnosti. Fazno poročilo, Krožne tehnološke

zasnove in poslovni modeli v slovenskem kmetijstvu (angl. Circular technological concepts and business models in Slovenian agriculture), V4-2208, Slovenian Research and Innovation Agency, Ljubljana, 110 pp.

Gołębiewska E, Kalinowska M, Yildiz G. (2022). Sustainable Use of Apple Pomace (AP) in Different Industrial Sectors. *Materials (Basel). 27;15(5),* 1788. doi: 10.3390/ma15051788. PMID: 35269018; PMCID: PMC8911415.

Costa, J. M., Ampese L. C., Ziero, H. Di D., Sganzerla W. G., Forster-Carneiro T., (2022). Apple pomace biorefinery: Integrated approaches for the production of bioenergy, biochemicals, and value-added products – An updated review. *Journal of Environmental Chemical Engineering,* 10(108358). https://doi.org/10.1016/j.jece.2022.108358.

Joyce, A., & Paquin, R. L. (2016). The triple layered business model canvas: A tool to design more sustainable business models. Journal of Cleaner Production, 135, 1474-1486. https://doi.org/10.1016/j.jclepro.2016.06.067.

Juvančič L., Fatur M., Kavčič, S., Mihelič R., Schwarzmann A., Berne S., Osojnik Črnivec I. G., Novak U., Makovšek K., Sežun M., Lavrič G., Bolka S., Križnik N., Bedenk T. (2025) Krožne tehnološke zasnove in poslovni modeli v slovenskem kmetijstvu, Povzetek rezultatov in ugotovitev projekta, Krožne tehnološke zasnove in poslovni modeli v slovenskem kmetijstvu (angl. Circular technological concepts and business models in Slovenian agriculture), V4-2208, Slovenian Research and Innovation Agency, Ljubljana, 37 pp.

Kauser, S. Murtaza, M. A.,Hussain, A.,Imran, M., Kabir, K.,Najam, A., An, Q. U., Akram, S., Fatima, H., Batool, S. A., Shehzad, A.,Yaqub, S. (2024). Apple pomace, a bioresource of functional and nutritional components with potential of utilization in different food formulations: A review. *Food Chemistry Advances, 4,* 2772-753X, https://doi.org/10.1016/j.focha.2023.100598.

Lavtižar, V., Kos, I., Košir, L.G., Bavcon Kralj M., Trebše P., (2021). A Transition Towards the Circular Economy in Slovenia. In Circular Economy: Recent Trends in Global Perspective (pp. 425-456). Singapore: Springer Nature Singapore.

Ma, Y., Luo, J., Xu, Y., (2019). Co-preparation of pectin and cellulose from apple pomace by a sequential process. *Journal of Food Science and Technology, 56(9)*, p. 4091–4100. https://doi.org/10.1007/s13197-019-03877-5

Muscat, A., de Olde, E.M., Ripoll-Bosch, R. (2021). Principles,drivers and opportunities of a circular bioeconomy. *Nature Food 2,* 561–566, https://doi.org/10.1038/s43016-021-00340-7

Osterwalder, A., & Pigneur, Y. (2010). Business model generation: a handbook for visionaries, game changers, and challengers (Vol. 1). John Wiley & Sons.

VIRTUAL TECHNOLOGY FOR TEACHING ABOUT DRINKING WATER PREPARATION AND WASTEWATER TREATMENT

URŠKA ROZMAN,[1] MATEVŽ GABRIEL MOŽE GUERRERO,[2] SEBASTJANA KLEPEC HLEBIČ,[3] BOŠTJAN ERJAVEC,[3] SENKA HUSAR,[3] SONJA ŠOSTAR TURK[1]

[1] University of Maribor, Faculty of Health Sciences, Maribor, Slovenia
urska.rozman@um.si, sonja.sostar@um.si
[2] University of Maribor, Faculty of Chemistry and Chemical Technology, Maribor, Slovenia
matevz.moze@student.um.si
[3] Mariborski vodovod, javno podjetje, d.o.o., Mariobr, Slovenia
sebastjana.klepec.hlebic@mb-vodovod.si, bostjan.erjavec@mb-vodovod.si, senka.husar@mb-vodovod.si

Slovenia's sustainable strategy prioritises wastewater management and drinking water preparation, yet their interconnection in the light of climate change is often neglected. To address these challenges, different educational tools were prepared, using innovative technologies. Using a 360° camera, the processes at the Maribor Waterworks and Central Wastewater Treatment Plant were recorded, documenting water preparation, treatment and laboratory work. The materials were processed with H5P software to create interactive digital lessons in Moodle. These resources raise awareness about environmental health, focusing on wastewater management and safe drinking water practices. Ultimately, the educational tools enhance skills, expand knowledge, and supports efforts to protect the environment and combat climate change.

DOI
https://doi.org/10.18690/um.fkkt.1.2026.7

ISBN
978-961-299-130-2

Keywords:
drinking water,
wastewater,
digital learning materials,
360 degree camera,
virtual reality

University of Maribor Press

1 Introduction

Wastewater management and drinking water preparation are two of the priority areas of the Slovenian sustainable smart specialisation strategy (Ministrstvo za kohezijo in regionalni razvoj, 2025). However, the connection is often overlooked between wastewater treatment and an adequate drinking water supply. Due to the impact of the increasing climate change, there is an urgent need to educate students, employees and the wider population, which can be achieved successfully through the use of new technologies (e.g., extended reality) (Fauville et al., 2020; Thoma et al. 2023; Said et al., 2023).

1.1 Drinking water

Drinking water represents one of the most essential resources for human survival, public health and sustainable development. The preparation of drinking water involves a series of carefully controlled technological processes that transform raw water into safe, high-quality water suitable for consumption. These stages typically include abstraction from groundwater or surface water, aeration, coagulation and flocculation, sedimentation, sand or membrane filtration, activated carbon treatment and final disinfection. Each step plays a crucial role in reducing or eliminating microbiological risks, suspended solids, organic matter, chemical pollutants and potentially harmful trace substances (CDC, 2022).

In Slovenia, groundwater is the primary source of drinking water, which naturally provides a high level of protection, but is also increasingly vulnerable to the effects of climate change. Rising temperatures, altered precipitation patterns, agricultural runoff and extreme weather events can influence water quality and availability (NIJZ, 2023). As a result, the need for continuous monitoring, public awareness and educational initiatives has grown significantly. Virtual reality (VR) and 360° video allow learners to explore the internal structure of water facilities, observe the functioning of filtration systems, and understand better how strict procedures ensure microbiologically safe and chemically stable drinking water (Djordjević et al., 2025).

1.2 Wastewater

Wastewater treatment is a critical process that protects the environment by removing pollutants from used water before it is returned to natural ecosystems. Municipal wastewater typically contains organic materials, nutrients such as nitrogen and phosphorus, detergents, chemicals and microorganisms. Treatment begins with mechanical processes—screening, grit removal, and primary sedimentation—followed by biological treatment, where the microorganisms in activated sludge break down the organic substances. Advanced steps include tertiary treatment, nutrient removal, disinfection and sludge handling (European Environment Agency, 2023).

The Central Wastewater Treatment Plant Maribor plays a key role in maintaining water quality in the Drava River basin. With VR-supported learning, users can walk virtually through different treatment stages, observe aeration tanks, sedimentation basins, sludge dewatering units and laboratory testing areas. This immersive approach allows the learners to understand how wastewater becomes sufficiently purified for release into the natural environment, highlighting the interconnectedness of human activities, environmental protection and long-term water sustainability (Yunqin et al., 2022).

1.3 Innovative Learning Technologies

Traditional teaching materials often fail to convey the spatial complexity, scale and procedural details of water treatment systems. Innovative technologies—such as virtual reality, augmented reality, 360° recordings and H5P based interactive modules—provide an effective solution to this challenge. These tools support experiential learning by allowing the users to step inside real environments, interact with processes, and engage in self-directed exploration (Lampropoulos et al., 2025; Hamilton et al., 2021; Safitri et al., 2025).

VR enhanced learning has been shown to improve motivation, cognitive engagement, and long-term knowledge retention, especially in science and engineering education (Fauville et al., 2020; Said et al., 2023). In this project, these technologies were integrated strategically, to create an immersive experience that combines visual realism, guided explanations, quizzes and interactive hotspots. The

final result enables students and professionals to understand complex water management systems in a realistic, intuitive and pedagogically rich format.

2 Methods

2.1 Literature Review on Drinking Water and Wastewater

The research began with a comprehensive literature review focused on drinking-water treatment processes, wastewater purification technologies, the importance of water quality for public health and the impacts of climate change on water resources. The reviewed materials included the World Health Organization (WHO) guidelines, scientific articles, technical reports, and national regulations governing drinking-water preparation and municipal wastewater treatment (WHO, 2022; European Environment Agency, 2023). The findings from the literature review served as the foundation for developing recording scenarios and designing interactive learning materials.

2.2 Development of the Recording Scenarios

Based on the studied sources, detailed scenarios were prepared for filming at the Maribor Waterworks and the Central Wastewater Treatment Plant Maribor. These scenarios covered key stages of both processes, including raw water abstraction, filtration, disinfection and distribution, as well as mechanical and biological wastewater treatment and laboratory analysis procedures. The objective of the scenarios was to establish a logical sequence, provide clear explanations, and incorporate interactive components that would allow the users to gain a deeper understanding of water-treatment technologies.

2.3 Video Processing and Integration of Interactive Elements

Filming was conducted using the Insta360 360-degree camera. After footage collection, the material underwent digital processing, during which H5P was used to add interactive hotspots, questions, hyperlinks and graphical representations of the processes. These interactive elements were designed to offer the users explanations of the individual treatment stages and real-time knowledge checks during the virtual tour. The final materials were also adapted for use with 3D headsets, enabling an immersive experience of the waterworks and wastewater-treatment environments.

3 Results

Digital interactive learning materials in the form of a virtual walk through and as learning materials for an online classroom have been prepared, with the help of which we can raise awareness among the users about the environmental determinants of health, more specifically about the importance and procedures for wastewater management and appropriate preparation and control of drinking water.

3.1 Virtual tour through the premises of Maribor Waterworks and WWTP with interactions and a quiz

A 360-degree virtual tour with embedded information allows the user to walk through the premises of the Maribor Waterworks and WWTP. This way, the user can view and obtain information about the history of the Maribor Waterworks, a presentation of the waterworks, the filling fountain, cascades, sand filters, bioindicators, pumping station, water supply, control centre, wells, and a presentation of the quality and compliance of drinking water (Table 1). The user can view each of the images freely in a 360-degree view and read the added information. The interactions about WWTP contains basic information, laboratory analyses, air purification, waste removal with coarse and fine screens, sand and grease removal, biological treatment, and treatment of waste sludge, sand and grease (Table 2).

Table 1: Virtual tour through the premises of Maribor Waterworks with interactions

Location	Space shot with embedded interaction
Maribor Waterworks - history	
Maribor Waterworks - in numbers	

Location	Space shot with embedded interaction
Filling fountain	
Cascades	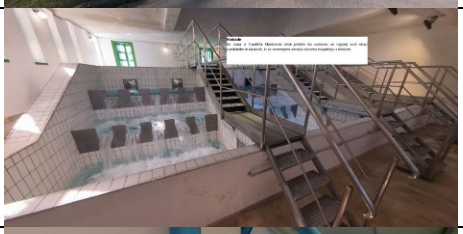
Sand filters	
Bioindicators	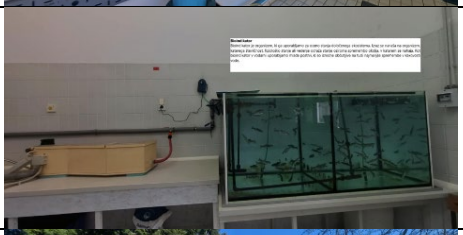
Pumping station	
Water supply	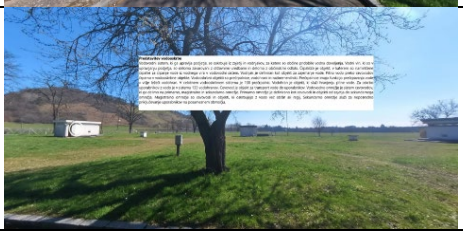

Location	Space shot with embedded interaction
Control center	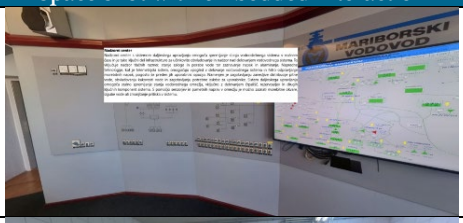
wells	
Quality and compliance of drinking water	

Source: own

Table 2: Virtual tour through the WWTP with interactions

Location	Space shot with embedded interaction
basic information	
laboratory analyses	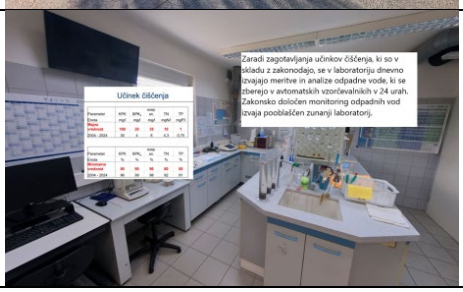

air purification	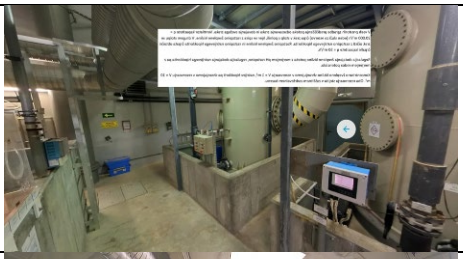
waste removal with coarse and fine screens	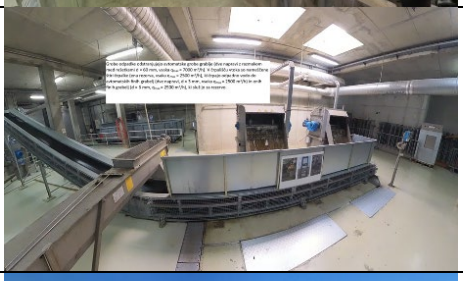
sand and grease removal	
biological treatment	
treatment of sludge from biological treatment, sand and grease treatment	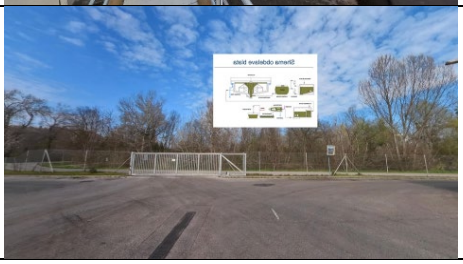

Source: own

After completing the tour, the user can take a 5-question quiz to test their knowledge about Maribor Waterworks (Table 3) or a 28-question quiz about WWTP. Each correct answer is also provided with an explanation of the answer.

Table 3: Five-question quiz about Maribor Waterworks

Question	Answer with explanation
Why is water white? 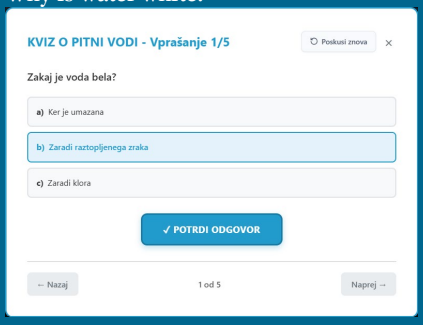	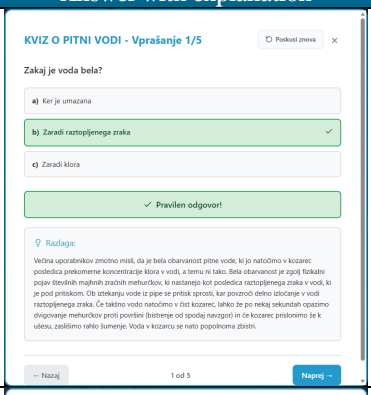
Why is the water brown? 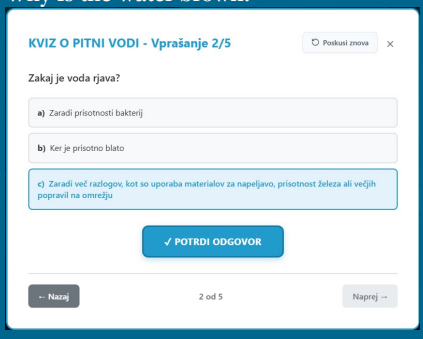	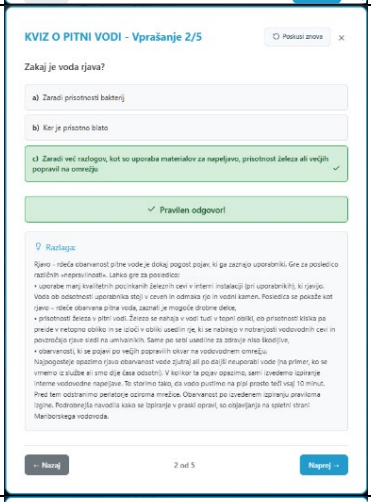
Why is water disinfected? 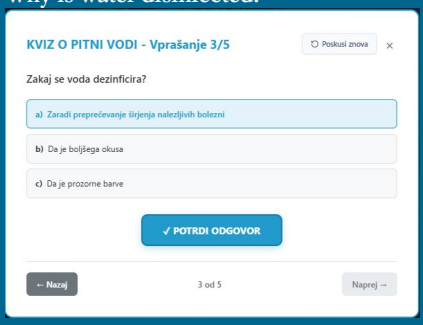	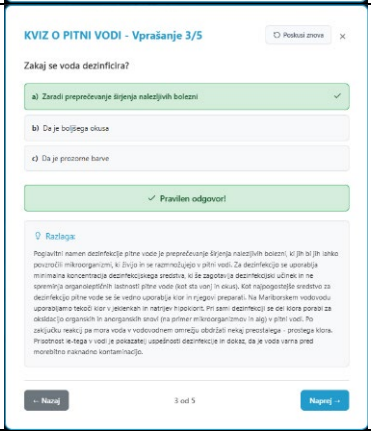

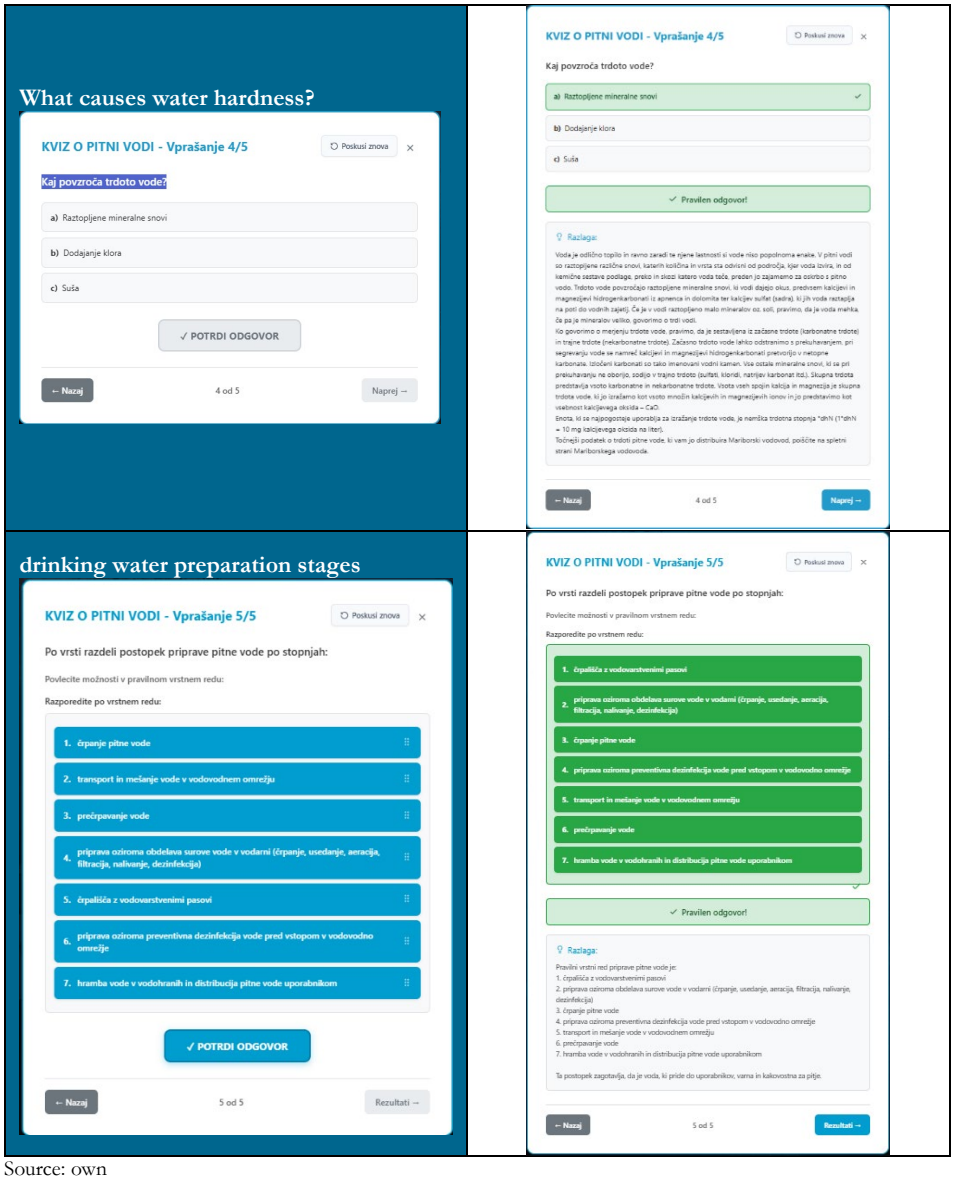

Source: own

3.2 Learning materials with knowledge testing in the online classroom

The 360-degree videos were processed with H5P, and different interactions were inserted, e.g., drag and drop a word, choosing the correct answers, correct / incorrect, fill in the missing words (Table 4,5). The learning material is designed in a

way where the user must choose all the correct answers or solve the tasks correctly in order to continue viewing. This encourages continuous learning and knowledge testing.

Table 4: Learning materials about Maribor Waterworks in the online classroom (selected interactions)

Interaction	Content / Print screen
Drag and drop a word	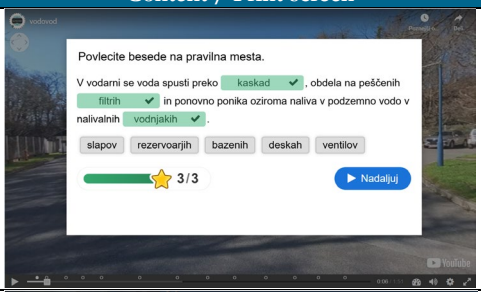
Choosing the correct answers	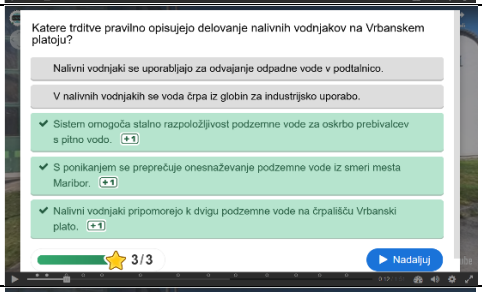
Correct / incorrect	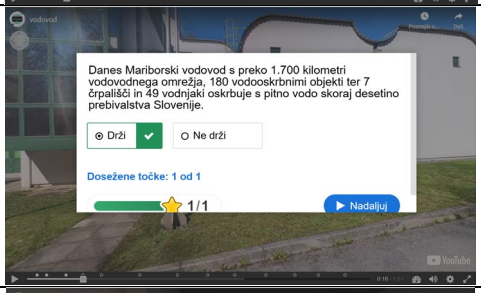
Fill in the missing words	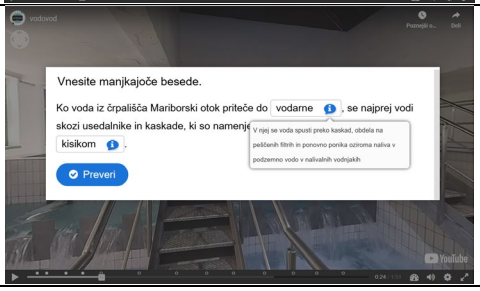

Source: www.um.si

Table 5: Learning materials about WWTP in the online classroom (selected interactions)

Interaction	Content / Print screen
Drag and drop a word	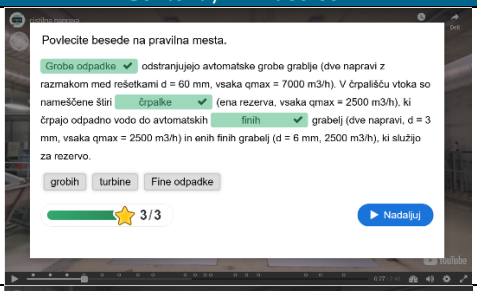
Choosing the correct answers	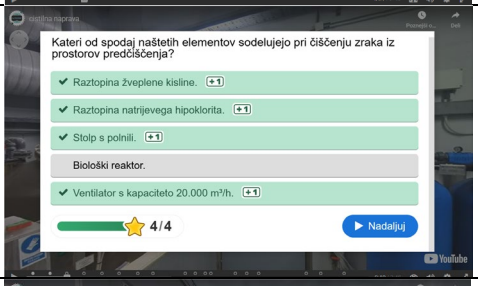
Correct / incorrect	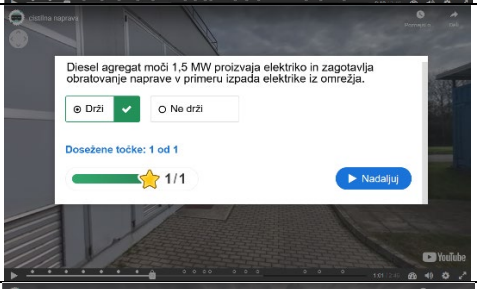
Fill in the missing words	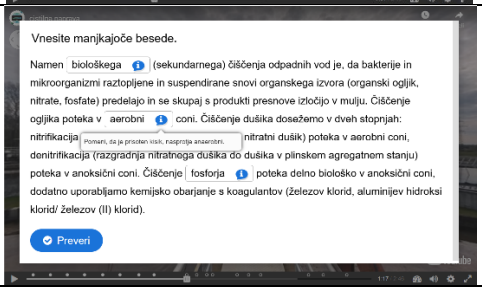

4 Conclusions

Innovative learning materials enable the acquisition of new skills, the upgrading of existing knowledge, as well as the verification and consolidation that is essential for maintaining a healthy environment and combating climate change effectively.

Acknowledgment

The project was implemented within the framework of the Public Tender »Problemsko učenje študentov v delovno okolje: gospodarstvo, negospodarstvo in neprofitni sektor v lokalnem/regionalnem okolju 2024-2027 (PUŠ v delovno okolje 2024-2027)«. We would like to thank all the participating students.

References

Centers for Disease Control and Prevention. (2022). How water treatment works. CDC. https://www.cdc.gov/drinking-water/about/how-water-treatment-works.html

Djordjević, A., Ćirić, M., Milošević, V., Radivojević, D., Zammit, E., Scerri, D., & Gocić, M. (2025). Transforming water education through investment in innovation: A case study on the cost-benefit of virtual reality in water education. Water, 17(13), 1998. https://doi.org/10.3390/w17131998

European Environment Agency. (2023). Wastewater treatment and water quality in Europe. https://www.eea.europa.eu/themes/water/interactive/water-quality

Fauville, G., Luo, M., Queiroz, A. C. M., Bailenson, J. N., & Hancock, J. (2020). Virtual reality as a practical tool for environmental education. Computers & Education, 147, 103778. https://doi.org/10.1016/j.compedu.2019.103778

Fauville, G., Queiroz, A. C. M., & Bailenson, J. N. (2020). Virtual reality as a promising tool to promote climate change awareness. In J. Kim & H. Song (Eds.), Technology and health: Promoting attitude and behavior change (pp. 91–108). Elsevier.

Hamilton, D., McKechnie, J., & Edgerton, E. (2021). Immersive virtual reality as a pedagogical tool in education: A systematic literature review of quantitative learning outcomes and experimental design. Journal of Computers in Education, 8, 1–32. https://doi.org/10.1007/s40692-020-00169-2

Lampropoulos, G., Fernández-Arias, P., de Bosque, A., & Vergara, D. (2025). Virtual reality in engineering education: A scoping review. Education Sciences, 15(8), 1027. https://doi.org/10.3390/educsci15081027

Li, Y., Zeng, Y., & Fang, S. (2022). Sewage treatment experiment teaching system based on virtual reality. Curriculum and Teaching Methodology, 5, 63–72. https://doi.org/10.23977/curtm.2022.050210

Ministrstvo za kohezijo in regionalni razvoj. (2025). Slovenska strategija trajnostne pametne specializacije – S5.

NIJZ. (2023). Svetovni dan voda 2023. Center za zdravstveno ekologijo. https://nijz.si/wp-content/uploads/2023/03/SVETOVNI-DAN-VODA-daljse-besedilo_14-03-23.pdf

Said, I., et al. (2023). Immersive climate narratives: Using extended reality to raise climate change awareness. In Proceedings of the 29th ACM Symposium on Virtual Reality Software and Technology (Article 63). Association for Computing Machinery.

Said, R., Kurniawan, F., & Hamid, M. (2023). Immersive learning for sustainable water management using virtual reality: A review. Sustainability, 15(5), 4123. https://doi.org/10.3390/su15054123

Safitri, D., Marini, A., Irwansyah, P., & Sudrajat, A. (2025). Transforming environmental education with augmented reality: A model for learning outcome. Social Sciences & Humanities Open, 12, 101796. https://doi.org/10.1016/j.ssaho.2025.101796

Thoma, S. P., et al. (2023). Increasing awareness of climate change with immersive virtual reality. Frontiers in Virtual Reality, 4.

World Health Organization. (2022). Guidelines for drinking-water quality. WHO. https://www.who.int/publications/i/item/9789240045064

MINERAL CO_2 SEQUESTRATION IN INDUSTRIAL WASTE MATERIALS: A COMPARATIVE STUDY USING FTIR, TGA AND CALCIMETRY

SARA TOMINC,[1] MAJDA PAVLIN,[1] MARUŠA MRAK,[1] VILMA DUCMAN,[1] OGNJEN RUDIĆ,[2,3] CYRILL GRENGG[2]

[1] Slovenian National Building and Civil Engineering Institute, Ljubljana, Slovenia
sara.tominc@zag.si, majda.pavlin@zag.si, marusa.mrak@zag.si, vilma.ducman@zag.si
[2] Graz University of Technology, Institute of Applied Geosciences, Graz, Austria
ognjen.rudic@tugraz.at, cyrill.grengg@tugraz.at
[3] Graz University of Technology, Institute of Technology and Testing of Building Materials, Graz, Austria
ognjen.rudic@tugraz.at

Mineral CO_2 sequestration is a promising approach for reducing greenhouse gas emissions by storing CO_2 in stable forms permanently. This process involves capturing CO_2 and converting it into solid carbonates through mineralisation. Waste ashes and slags, by-products of waste incineration and steel production, are promising materials for CO_2 sequestration, due to their high alkalinity and reactive mineral phases. In this study, the CO_2 sequestration potentials of different metallurgical slags and incineration ashes from Austria and Slovenia were analysed using Fourier transform infrared spectroscopy (FTIR), thermogravimetric analysis (TGA), and calcimetry. Biomass ash (A1) showed the highest sequestration capacity of 153.7 g CO_2 per kg of ash.

DOI
https://doi.org/10.18690/um.fkkt.1.2026.8

ISBN
978-961-299-130-2

Keywords:
CO_2 sequestration capacity, enhanced carbonation, thermogravimetric analysis, calcimetry, Fourier transform infrared spectroscopy

University of Maribor Press

1 Introduction

CO_2 is the most significant greenhouse gas (GHG) produced by human activities, accounting for about two-thirds of the enhanced greenhouse effect. The development of carbon capture and storage (CCS) technologies is one possible strategy to reduce atmospheric CO_2 (Medas et al., 2017). Mineral CO_2 sequestration is a carbon capture and storage process in which CO_2 reacts chemically with Ca- and Mg-containing minerals to form stable carbonate products (Li and Wu, 2022). Alkaline residues such as slags and ashes typically contain highly reactive Ca and Mg species that are potentially suitable for high and rapid carbonate conversion without the need for pre-treatment or energy-intensive operating conditions (Medas et al., 2017, Alturki, 2022; Li and Wu, 2022). For the steel industry, responsible for almost 8% of global CO_2 emissions, mineral carbonation technologies present a major opportunity, as the mineralisation of iron and steel slags could reduce its carbon footprint directly. Consequently, integrating carbon capture and storage management into the circular economy framework is crucial for progress towards global environmental goals (Capelo-Avilés et al., 2024).

Enhanced carbonation treatment has recently been developed extensively to improve the capacity and efficiency of CO_2 sequestration. Compared to natural carbonation, enhanced carbonation increases both the reaction rate and the carbon storage potential of materials significantly. Based on the exposure conditions applied during the CO_2 mineralisation process, carbonation treatments are generally divided into three main categories: gas-solid carbonation (dry carbonation), semi-dry carbonation (with water vapour), and aqueous carbonation (in suspension) (Li and Wu, 2022, Zajac et al., 2022). In the aqueous phase, the main mineralisation reaction involves the initial hydration of the free Ca and Mg oxides to form Ca and Mg hydroxides, followed by carbonation to Ca and Mg carbonates (Capelo-Avilés et al., 2024). Several factors influence the rate and extent of carbonation, including the CO_2 partial pressure, temperature and moisture or water content. Carbonation is enhanced by the addition of water or moisture, which promotes CO_2 dissolution and leaching of Ca^{2+} from the mineral constituents, while excessive water can hinder CO_2 diffusion by blocking the pores of the matrix. The reaction rate can also be increased by raising the temperature to between 30 and 60 °C. However, carbonation efficiency decreases above 60 °C due to the lower solubility of CO_2 in water at higher temperatures (Ukwattage et al., 2015).

In addition, carbonated mineral residues can be used in the production of construction materials (cement and concrete, road construction, lightweight aggregates and AAMs), wastewater treatment, or environmental remediation. For example, carbonated slag has significant potential for the cement industry, as the carbonation process can improve the hydraulic properties of this by-product (Biava et al., 2024). In this study, the CO_2 sequestration potential of selected industrial residues from Austria and Slovenia was evaluated, with the aim of using the resulting carbonated mineral residues as secondary raw materials for the production of sustainable mineral-based construction materials.

2 Materials and methods

Two types of raw materials were selected for this study: waste ash and slag. The ash samples were wood biomass bottom ash (A1) and coal fly ash with added bauxite (A2), while the slag samples were electric arc furnace (EAF) slag (S1) and a mixture of electric arc furnace stainless (EAF-S) slag and ladle slag (S2).

Before the chemical analysis the samples were dried in a laboratory oven at 105 °C to a constant weight and sieved to a particle size below 125 µm. To determine the loss on ignition (LOI), the samples were heated at 950 °C in accordance with EN 196-2:2013. The fused beads were prepared by mixing ash with a flux of 50% lithium tetraborate and 50% lithium metaborate at a ratio of 1:10 (0.947 g ash to 9.47 g flux) and heating at 1100 °C. The chemical composition of the samples was analysed using a Thermo Scientific ARL PERFORM'X Wavelength Dispersive X-ray Fluorescence Spectrometer (WDXRF) equipped with an Rh-target X-ray tube and UniQuant software.

For the mineralogical analysis, each sample was sieved to below 63 µm and placed in 27 mm diameter holders. To minimise the effects of the preferred orientation, the samples were back-loaded into a circular sample holder. An X-ray diffraction (XRD) analysis was performed before and after carbonation using a PANalytical Empyrean X-ray diffractometer with a CuKα1 X-ray source. The X-ray tube was operated at 45 kV and 40 mA. The measurements were carried out in a 2θ range of 4-70° with a step size of 0.013° 2θ. The external standard method with corundum (NIST SRM 676a) was used to determine the amorphous phase. The quantitative phase analysis was performed using XRD powder patterns and ICDD PDF-4 (2020) database files,

applying Rietveld refinement with the PANalytical X'Pert HighScore Plus diffraction software (version 4.9).

The sequestration potential of 15 g of each sample with a particle size below 125 μm was tested using a modified method (Tominc and Ducman, 2023) for semi-dry carbonation at a controlled relative humidity of 80 ± 3.2 %, a temperature of 40 ± 0.5 °C, and a CO_2 concentration of 20 ± 0.1 vol% for 72 hours. Before exposure in the carbonation chamber, the samples were mixed with 10 wt.% water. Carbonation was considered complete when a constant mass was reached. The CO_2 content (wt.%) in the samples was determined by FTIR, TGA and calcimeter, and the CO_2 uptake was calculated based on Equation (1) (Medas et al., 2017, Nielsen and Quaghebeur, 2023):

$$\mathrm{CO_{2\ uptake}(wt\%)} = \frac{(\mathrm{CO_{2\ carb}\ (wt\%) - CO_{2\ orig}\ (wt\%)})}{(100 - \mathrm{CO_{2\ carb}\ (wt\%)})} \times 100 \quad (1)$$

The CO_2 uptake quantifies the increase in CO_2 content during the carbonation process, while the CO_2 sequestration capacity ($CO_{2\ capacity}$) indicates the total amount of CO_2 that can be sequestered per kilogram of the analysed sample (g_{CO2}/kg_{sample}). The CO_2 sequestration capacity of each sample was calculated using Equation (2) (Capelo-Avilés et al., 2024). $CO_{2\ carb}$ refers to the measured CO_2 content in the sample (wt%) after complete carbonation.

$$\mathrm{CO_{2\ capacity}}\left(\mathrm{g_{CO2}/kg_{sample}}\right) = \frac{\mathrm{CO_{2\ carb}\ (wt\%)}}{100 - \mathrm{CO_{2\ carb}\ (wt\%)}} \times 1000 \quad (2)$$

For the calcimetry, which measures the carbonate content based on its reaction with 10% hydrochloric acid, the CO_2 release was measured using a pressure calcimeter (OFITE Calcimeter, OFI Testing Equipment Inc., USA, according to ASTM D 4373) with an analytical error below 5%. The calcimeter was calibrated before the measurements by reacting HCl with a $CaCO_3$ standard (Calcium Carbonate Precipitated, OFI Testing Equipment, Inc., CAS: 471-34-1). The calibration curve (Figure 1) was generated from five measurements (0.2, 0.4, 0.6, 0.8, and 1.0 g $CaCO_3$) with R^2=0.9996.

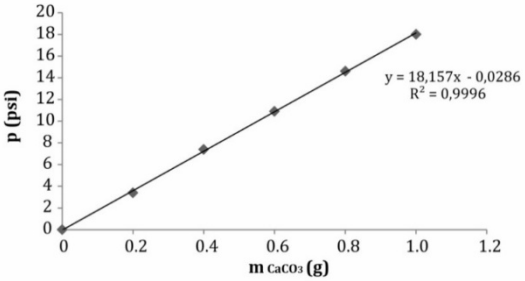

Figure 1: Calibration curve for the calcimetric measurements.
Source: own.

Thermogravimetric analysis (TGA) was performed on dry samples using a TGA Q5000IR thermal analyser (TA Instruments, New Castle, Delaware, USA). The analysis followed a controlled heating programme with a ramp rate of 10 K min^{-1} from 25 to 1000 °C. To prevent oxidation, the sample chamber was filled with N_2 at a flow rate of 25 mL min^{-1}. Approximately 20 mg of each sample was placed in 100 µL Al_2O_3 crucibles. The CO_2 content was determined from the mass loss within the temperature range associated with the decomposition of the carbonate mineral (500-800 °C), based on the dry matter at 105 °C (Capelo-Avilés et al., 2024). The measurements were analysed using a TA Universal Analysis 2000 v.4.5A (TA Instruments, New Castle, Delaware, USA). Each sample was tested individually.

A Fourier transform infrared (FTIR) spectrometer (PerkinElmer Spectrum Two, Kentucky, USA) equipped with an attenuated total reflection accessory (Universal ATR) was used to observe the infrared spectra of the analysed samples, using a diamond crystal as a solid sample support, in the range 380-4000 cm^{-1} at a resolution of 4 cm^{-1}. The standards calcite (Calcium Carbonate Precipitated, OFI Testing Equipment, Inc., CAS: 471-34-1) and quartz (Silicon Dioxide, Sigma-Aldrich, Co., CAS:60676-86-0) with known concentrations were used to generate a calibration curve (Figure 2). The calibration curve was generated with eight measurements (100% SiO_2, 95% SiO_2 + 5% $CaCO_3$, 90% SiO_2 + 10% $CaCO_3$, 80% SiO_2 + 20% $CaCO_3$, 70% SiO_2 + 30% $CaCO_3$, 50% SiO_2 + 50% $CaCO_3$, 30% SiO_2 + 70% $CaCO_3$ and 100% $CaCO_3$), with a correlation of 0.9993 and a standard error of 1.47%. After the spectra were acquired for ATR-FTIR, automatic baseline correction was performed, and the positions and peak heights were recorded using the Spectrum Quant 10.6 software.

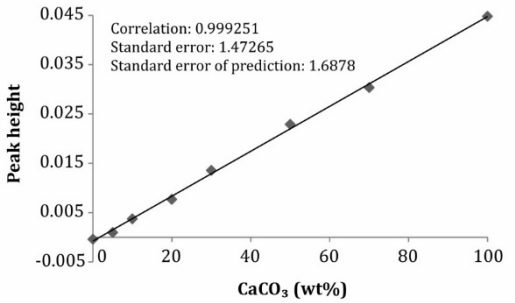

Figure 2: Calibration curve for FTIR.
Source: own.

3 Results and Discussion

The X-ray fluorescence analysis (XRF) revealed that the untreated analysed ashes and slags are composed mainly of CaO (18-37%), SiO_2 (11-39%) and Al_2O_3 (7-32%), with varying amounts of MgO (1-13%), Fe_2O_3 (0-33%), SO_3 (0.1-4%) and K_2O (0.01-3%), while Na_2O was present only in low concentrations. Of these, the contents of CaO and MgO are of particular interest, as these oxides play a key role in mineral carbonation. Both react with CO_2 to form stable carbonates, making these residues promising candidates for CO_2 sequestration. Among the analysed samples, A1 and S2, which have the highest CaO and MgO contents, show high potential for carbonation and, consequently, significant CO_2 uptake. The detailed chemical composition and the LOI at 950 °C are presented in Table 1.

The carbonation behaviour of the samples was investigated under controlled conditions. The reaction was completed after 72 hours, and the reaction rate was increased significantly by the addition of 10 wt.% water and a higher CO_2 concentration compared to our previous study (Tominc and Ducman, 2025), in which 4 vol.% CO_2 was used without water added before placing the samples in the carbonation chamber. The literature also indicates that the presence of water plays a crucial role in enhanced carbonation, as it allows the dissolution of CO_2, promotes the formation of bicarbonate/carbonate ions, increases the mobility of Ca^{2+} and Mg^{2+}, and provides the medium for the nucleation and precipitation of stable carbonates (Medas et al., 2017, Capelo-Avilés et al., 2024).

Table 1: Chemical composition of the analysed ashes and slags in terms of primary oxides (wt.%), measured by XRF, and LOI at 950 °C.

Sample ID	LOI $_{950\ °C}$	Al_2O_3	SiO_2	CaO	MgO	Fe_2O_3	K_2O	Na_2O	SO_3
A1	9.38	7.28	39.0	29.35	4.56	3.42	3.01	1.02	0.76
A2	23.39	32.08	10.87	17.71	0.64	6.40	2.21	0.41	4.09
S1	0.20	14.33	13.82	22.91	6.32	32.96	0.01	0.35	0.11
S2	9.60	9.58	18.16	37.41	13.49	7.55	0.01	0.00	0.29

Source: own

A comparison of the untreated and carbonated samples highlights the effect of carbonation on their mineralogical composition. As shown in Table 2 and Figure 3, phases susceptible to carbonation decreased progressively, indicating their transformation into carbonation products.

Table 2: Phase composition of the analysed ashes and slags (wt.%).

Mineral	Formula	A1 untr	A1 carb	A2 untr	A2 carb	S1 untr	S1 carb	S2 untr	S2 carb
calcite	$CaCO_3$	9.7	19.9	19.5	23.8	1.3	5.2	7.6	10.7
portlandite	$Ca(OH)_2$	12.5	0.5	-	-	-	-	-	-
ettringite	$Ca_6Al_2(SO_4)_3(OH)_{12}\cdot 26H_2O$			8.7	0.7				
gamma belite	γ-Ca_2SiO_4	-	-	-	-	12.8	2.7	5.3	4.1
gehlenite	$Ca_2Al_2SiO_7$	-	-	24.0	24.3	-	-	-	-
wüstite	FeO	-	-	16.1	16.3	-	-	-	-
quartz	SiO_2	7.8	8.4	1.0	1.2	-	-	-	-
akermanite	$Ca_2Mg(Si_2O_7)$	10.0	9.4	-	-	-	-	-	-
magnetite	Fe_3O_4	-	-	6.1	5.9	-	-	-	-
anhydrite	$CaSO_4$	-	-	5.5	5.4	-	-	-	-
periclase	MgO	-	-	-	-	-	-	4.7	4.2
diaspore	AlO(OH)	-	-	3.7	4.4	-	-	-	-
anorthite	$CaAl_2Si_2O_8$	-	-	3.1	3.2	-	-	-	-
gypsum	$CaSO_4\cdot 2H_2O$	-	-	3.0	0.0	-	-	-	-
merwinite	$Ca_3Mg(SiO_4)_2$	-	-	-	-	-	-	2.0	1.9
hematite	Fe_2O_3	-	-	1.4	2.0	-	-	-	-
brucite	$Mg(OH)_2$	-	-	-	-	-	-	<1.0	<1.0
ACn*		60.0	61.8	54.1	59.3	39.7	45.6	66.1	68.6

*ACn : Amorphous and Crystalline non-quantifiable phases; untr: untreated
Source: own

In the untreated A1 sample, the main crystalline phases were calcite (9.7 wt.%), portlandite (12.5 wt.%), akermanite (10.0 wt.%) and quartz (7.8 wt.%). After CO_2 treatment, a significant change in the mineral composition was observed, as the portlandite reacted (0.5 wt.%) with CO_2 almost completely to form calcite (19.9 wt.%). The phase assemblage of the untreated A2 sample contained mainly calcite,

ettringite and anhydrite, with low quantities of gypsum, hematite, diaspore, anorthite and quartz. The sample showed only a slight increase in calcite content (from 19.5 to 23.8 wt.%), suggesting a high degree of carbonation already during storage. However, during carbonation, the CO_2 reacts with the Ca-bearing phases such as ettringite (decreasing from 8.7 to 0.7 wt.%), leading to their decomposition and likely resulting in the formation of calcite and amorphous or poorly crystalline phases. The sulphate phases, such as gypsum and anhydrite, also decreased, while the inert minerals, such as hematite, diaspore and quartz showed little to no reaction. Meanwhile, the ACn fraction increased from 54.1 to 59.3 wt.%, which aligns with the formation of amorphous carbonation products following the breakdown of the ettringite and other Ca-bearing phases. The original sample S1 contained calcite, gamma belite, gehlenite, magnetite and wüstite. During carbonation, the gamma belite reduced noticeably (from 12.8 to 2.7 wt.%), indicating an extensive reaction with CO_2, consistent with the increase in calcite content (from 1.3 to 5.2 wt.%). Gehlenite, magnetite and wüstite are mostly inert under normal carbonation conditions. The ACn fraction increased from 39.7 to 45.6 wt.%, further supporting the formation of non-crystalline carbonation products. In sample S2, the calcite formation became increasingly prominent, rising from 7.6 to 10.7 wt.%, confirming calcite as the main carbonation product. The Ca- containing phases such as gamma belite react readily with CO_2 to form calcite (Chen et al., 2021). In the presence of water and CO_2, γ-belite and any residual β-belite can undergo carbonation, generating C-S-H and calcite (Chang et al., 2016). Other Ca-rich phases, including merwinite, showed lower carbonation reactivity.

Overall, Table 2 shows clearly that carbonation increased the calcite content in all the samples and decreased the carbonatable phases such as portlandite, ettringite and γ-belite. In contrast, phases such as gehlenite, magnetite, wüstite, anhydrite and quartz remained largely inert under the tested conditions.

For TGA, the mass loss between 500 and 800 °C was attributed to the thermal decomposition of $CaCO_3$ into CaO and CO_2 (Figure 4), while the mass loss at lower temperatures was attributed to the removal of organic carbon (typically in the range 250-500 °C), partial decomposition of the portlandite (usually around 400 °C, as shown in Figure 4a (the orange dotted lines), or the decomposition of the aluminate-ferrite-monosulphate (AFm) phases (such as monosulphate, monocarbonate, or Friedel's salt). This was distinctive for sample S2, and is recognisable as mass loss at around 140 and 400 °C (as shown in Figure 4b).

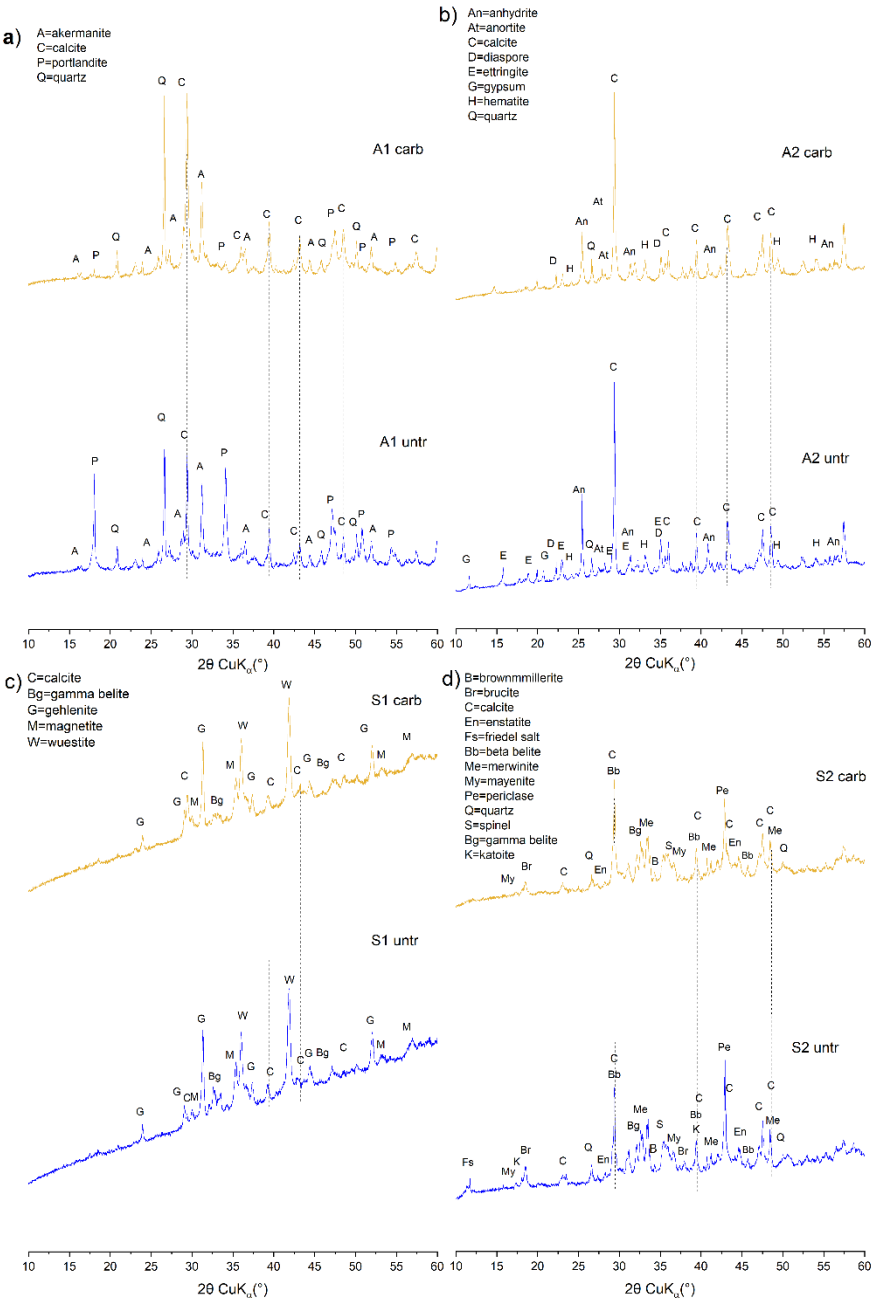

Figure 3: X-ray diffraction patterns of the untreated and carbonated samples: a) A1, b) A2, c) S1, and d) S2. Calcite, the main carbonation product, is indicated by the dotted lines.

Source: own.

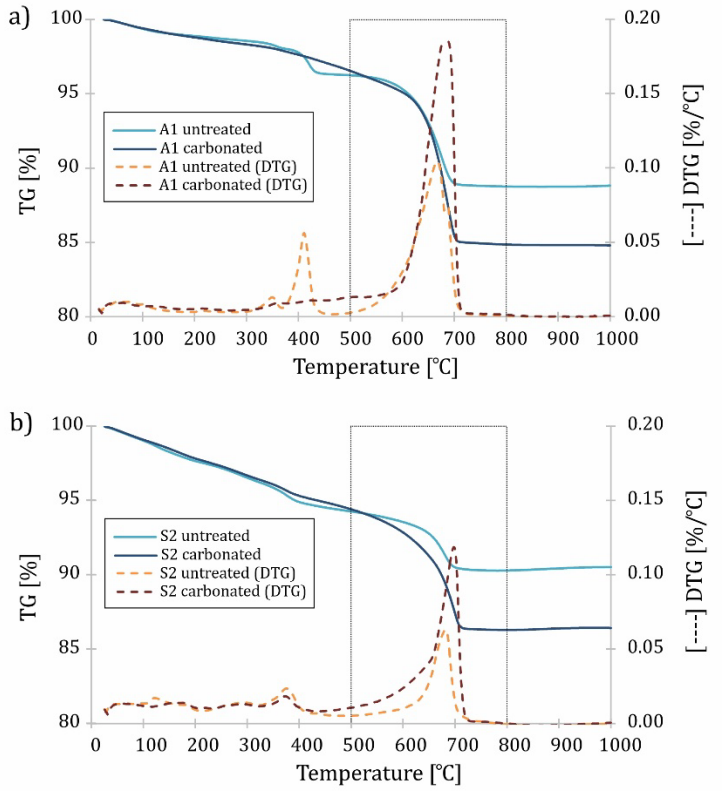

Figure 4: TG/DTG curves of the selected samples after 72 hours of carbonation for a) A1 and b) S2, showing the maximum CO_2 content in the temperature range 500-800 °C.

Source: own.

The FTIR analysis, which estimates the $CaCO_3$ content based on characteristic absorption bands, showed trends consistent with those of TGA, with only minor deviations observed at low levels of carbonation (e.g., S1 original). The FTIR spectra of the carbonated samples (Figure 5) showed the characteristic C-O bonds typical of carbonate phases, with a strong band at approximately 1410 cm^{-1} corresponding to the ν_3 vibrations of CO_3^{2-} (asymmetric C-O stretching). Additional bands at around 874 cm^{-1} and 712 cm^{-1} are attributed to the ν_2 out of-plane and in-plane bending vibrations of CO_3^{2-} from the trace carbonate compounds (Capelo-Avilés et al., 2024). The increased intensity of these bands in the carbonated samples confirms the formation of $CaCO_3$ during carbonation, consistent with the TGA and

calcimetric measurements. For the calcimetric measurements, the CO_2 content of the samples was determined using the stoichiometric ratios given in Equation (3):

$$CaCO_3 + 2HCl \rightarrow CaCl_2 + CO_2 + H_2O \quad (3)$$

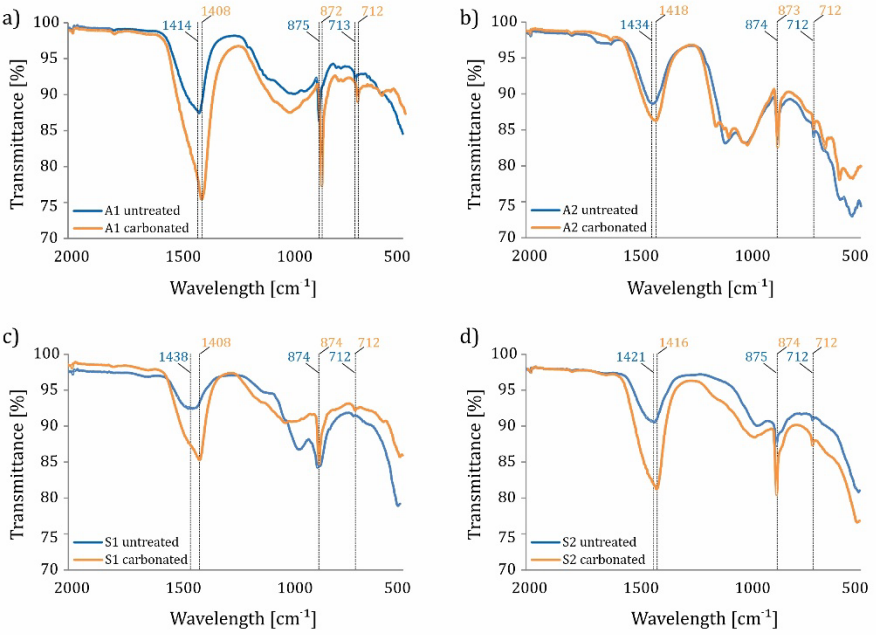

Figure 5: FTIR spectra of samples a) A1, b) A2, c) S1 and d) S2.
Source: own.

Table 3: Comparative analysis of $CaCO_3$ and CO_2 content before and after enhanced carbonation, determined by TGA, pressure calcimeter and quantitative FTIR.

Sample ID		TGA		FTIR		Calcimeter	
		CO_2/dry matter (wt%)	$CaCO_3$ (wt%)	CO_2 (wt%)	$CaCO_3$ (wt%)	CO_2 (wt%)	$CaCO_3$ (wt%)
A1	untr	7.6	**17.2**	7.6	**17.3**	5.5	**12.4**
	carb	11.8	**26.8**	12.8	**29.1**	13.3	**30.3**
A2	untr	9.8	**22.2**	10.5	**23.8**	10.8	**24.6**
	carb	10.8	**24.4**	11.8	**26.8**	11.2	**25.4**
S1	untr	0.9	**2.0**	2.6	**5.8**	2.2	**4.9**
	carb	3.2	**7.3**	3.6	**8.3**	5.3	**12.1**
S2	untr	4.0	**9.2**	4.1	**9.3**	4.1	**9.4**
	carb	8.2	**18.6**	8.1	**18.5**	9.8	**22.3**

Source: own

A comparative assessment of the $CaCO_3$ content before and after accelerated carbonation was performed using TGA, calcimetry and quantitative FTIR. All three techniques provided consistent estimates of the CO_2 content, with differences of less than 3 wt.%, as shown in Table 3.

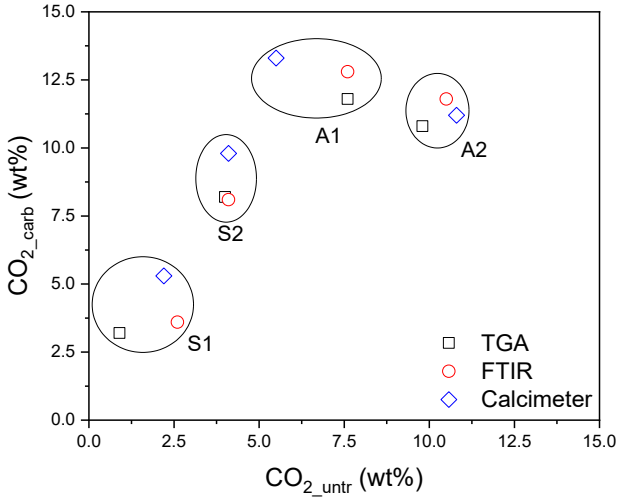

Figure 6: Comparison of the calculated CO_2 content (wt.%) before and after carbonation, determined by three analytical methods (TGA, FTIR and calcimeter). The scatter plot shows good agreement between the analytical methods for each sample.

Source: own.

The CO_2 uptake was calculated according to Equation (1). For most samples, the pressure calcimeter gives higher CO_2 uptake and capacity values than TGA and FTIR. The main limitation of TGA is the possible overlap in decomposition temperatures, while, for FTIR, weak peaks and peak overlap are also major limitations. The pressure calcimeter provides a more realistic estimate of the maximum capacity. Among the samples tested, biomass ash A1 showed the greatest increase in $CaCO_3$ content after CO_2 exposure, corresponding to a CO_2 uptake of 9.1 wt.% and CO_2 sequestration capacity of 153.7 g CO_2 per kg of ash according to the calcimetric measurements (Table 4). In contrast, ash A2 was found to be almost completely carbonated during storage, indicating high reactivity even under ambient conditions. The CO_2 uptake in ash A2 was only 0.4 wt.%; however, the CO_2 sequestration capacity was 125.7 g CO_2 per kg of ash. Sample S2, with a CO_2 uptake of 6.3 wt.%, demonstrated considerable potential for CO_2 sequestration, with a

capacity of 108.7 g CO_2 per kg of slag, while sample S1, with a CO_2 uptake of 3.3 wt.%, showed a comparatively lower carbonation potential, with a capacity of 56.2 g CO_2 per kg of slag, due to a lower proportion of reactive Ca- and Mg-containing minerals.

Table 4: CO_2 uptake (wt.%) and CO_2 sequestration capacity (g_{CO2}/kg_{sample}) of the analysed samples determined by TGA, FTIR and calcimeter.

Sample ID	TGA		FTIR		Calcimeter	
	CO_2 uptake	CO_2 capacity	CO_2 uptake	CO_2 capacity	CO_2 uptake	CO_2 capacity
A1	4.8	133.4	5.9	146.7	9.1	153.7
A2	1.1	120.5	1.5	133.6	0.4	125.7
S1	2.4	33.3	1.1	37.9	3.3	56.2
S2	4.5	89.1	4.4	88.6	6.3	108.7

Source: own

4 Conclusions

The potential for CO_2 sequestration in wood biomass bottom ash (A1), coal fly ash with added bauxite (A2), EAF slag (S1), and a mixture of EAF stainless slag and ladle slag (S2) was assessed, to support ongoing research aimed at reducing the carbon footprint of industrial processes. The selected waste materials have the potential for permanent CO_2 binding, with sequestration capacities of 56.2-153.7 g CO_2 per kg of sample according to the calcimetric measurements. In addition, the analysed materials will be used further as feedstock for the development of mineral-based construction materials, thus offering significant potential for applications in construction, infrastructure and environmental technology.

Acknowledgment

This work was supported by the Slovenian Research Agency and the Austrian Science Fund under Project no. N2-0320/I 6481-N (Waste to alkali-activated binders (WIN)), and was supported partially by the Slovenian Research and Innovation Agency (ARIS) under Research Core Grant no. P2-0273.

Data availability status

The original data presented in the study are openly available in the DiRROS repository at the following link: http://hdl.handle.net/20.500.12556/DiRROS-24534.

References

Alturki, A. (2022). The Global Carbon Footprint and How New Carbon Mineralization Technologies Can Be Used to Reduce CO_2 Emissions. *ChemEngineering, 6*, 44. doi:10.3390/chemengineering6030044

Biava, G., Depero, L.E., Bontempi E. (2024). Accelerated Carbonation of Steel Slag and Their Valorisation in Cement Products: A Review. *Spanish Journal of Soil Science, 14*,12908. doi: 10.3389/sjss.2024.12908

Capelo-Avilés, S., Tomazini de Oliveira, R., Gallo Stampino, I.I., Gispert-Guirado, F., Casals-Terré, A., Giancola, S., Galán-Mascarós, J.R. (2024). A thorough assessment of mineral carbonation of steel slag and refractory waste. *Journal of CO_2 Utilization, 82*, 102770. doi:10.1016/j.jcou.2024.102770

Chang, J., Fang, Y., Shang, X. (2016). The role of β-C_2S and γ-C_2S in carbon capture and strength development. *Materials and Structures, 49*, 4417–4424. doi:10.1617/s11527-016-0797-5

Chen, Z., Cang, Z., Yang, F., Zhang, J., Zhang, L. (2021). Carbonation of steelmaking slag presents an opportunity for carbon neutral: A review. *Journal of CO_2 Utilization, 54*, 101738. doi:10.1016/j.jcou.2021.101738

Li, L., Wu, M. (2022). An overview of utilizing CO_2 for accelerated carbonation treatment in the concrete industry. *Journal of CO_2 Utilization, 60*, 102000. doi:10.1016/j.jcou.2022.102000

Medas, D.,Cappai, G., De Giudici, G., Piredda, M. and Podda, S. (2017). Accelerated carbonation by cement kiln dust in aqueous slurries: chemical and mineralogical investigation. *Greenhouse Gasses: Science and Technology,7(4)*, 692–705. doi: 10.1002/ghg.1681

Nielsen, P., Quaghebeur, M. (2023). Determination of the CO_2 Uptake of Construction Products Manufactured by Mineral Carbonation. *Minerals, 13*, 1079. doi:10.3390/min13081079

Scrivener, K., Snellings, R. Lothenbach, B. (Eds.). (2016). A Practical Guide to Microstructural Analysis of Cementitious Materials (1st ed.). CRC Press. doi:10.1201/b19074

Tominc, S., Ducman, V. (2023). Methodology for Evaluating the CO_2 Sequestration Capacity of Waste Ashes. *Materials, 16*, 5284. doi:10.3390/ma16155284

Tominc, S., Ducman, V. (2025). Determination of the maximum CO_2 sequestration capacity of Slovenian waste ashes using thermogravimetry and calcimetry. *7th International Conference on Technologies & Business Models for Circular Economy: Conference Proceedings, 7*, 151-159. doi:10.18690/um.fkkt.1.2025.13

Ukwattage, N.L., Ranjith, P.G., Yellishetty, M. , Bui, H.H., Xu, T. (2015). A laboratory-scale study of the aqueous mineral carbonation of coal fly ash for CO_2 sequestration, *Journal of Cleaner Production, 103*, 665-674. doi:10.1016/j.jclepro.2014.03.005

Zajac, M., Skibsted, J., Bullerjahn, F., Skocek, J. (2022). Semi-dry carbonation of recycled concrete paste, *Journal of CO_2 Utilization, 63*, 102111. doi:10.1016/j.jcou.2022.102111

Fibre-Reinforced Cement as a Source of Microplastics and Their Post-Release Behaviour

Katja Turk,[1, 2] Branka Mušič[1]

[1] Slovenian National Building and Civil Engineering Institute, Ljubljana, Slovenia
katja.turk@zag.si, branka.music@zag.si
[2] University of Ljubljana, Faculty of Chemistry and Chemical Technology, Ljubljana, Slovenia
kt54579@student.uni-lj.si

The construction industry consumes vast amounts of plastics, but has in recent decades embraced the circular economy principles increasingly. Nevertheless, these materials degrade throughout their life cycle, and represent a non-negligible source of microplastics, contributing to one of today's major environmental challenges. In this study we investigated the generation and properties of microplastics released from cementitious composites reinforced with polypropylene (PP) and recycled polyethylene terephthalate (rPET) fibres. The two degradation scenarios (simulated wear and demolition) produced distinct particle size ranges, spanning from long fibres to fine fragments. Cement adhesion to the fibres, governed by their surface morphology and functionalisation, was identified as a factor capable of altering key properties such as the contaminant-dependent density. Complementary leaching experiments showed further that functionalised fibres exhibit a high potential for releasing organic substances. Overall, our findings highlight the need to consider multiple aspects of microplastics derived from fibre-reinforced cement when assessing their environmental implications.

DOI
https://doi.org/10.18690/um.fkkt.1.2026.9

ISBN
978-961-299-130-2

Keywords:
microplastics, fibre-reinforced cement, construction materials, circular economy, environmental impact

University of Maribor Press

1 Introduction

Plastics have transformed modern life, becoming indispensable due to their versatility, processability, low weight, and, above all, affordability. These properties have not only contributed to technological progress and improved quality of life but, in some cases, even reduced environmental impacts by lowering energy consumption and substituting other problematic materials (Hinton et al., 2022). In 2022, global plastic production exceeded 400 Mt (Plastics Europe, 2024), and projections estimate it may reach around 590 Mt by 2050 (*Global Plastic Production*, 2023). The scale of industry, dominated by short-lived products, remains tied strongly to fossil fuel dependence, the generation of vast and poorly managed waste streams, and the resulting pollution of ecosystems worldwide (Hinton et al., 2022). Because of this pervasive and persistent contamination, researchers refer increasingly to the present era as the "plastic age" (Porta, 2021; Stoett et al., 2024).

Within the framework of sustainable development, the circular economy has emerged as one of the central strategies. Beyond reducing environmental burdens, it also emphasises the recognition of plastic waste as a secondary resource for new products, thereby decreasing the demand for virgin raw materials (Shamsuddoha & Kashem, 2024). Among the industries where such circular solutions are particularly promising, construction stands out, due to its massive plastic demand and long product lifespans. Although progress remains slow and the development, as well as implementation of secondary raw materials, are limited (Awoyera & Adesina, 2020), the share of post-consumer recycled plastics has increased substantially, rising by 70% between 2018 and 2022 (Plastics Europe, 2024). This trend is especially significant for construction, which already accounts for 22.9% of recycled plastic use in Europe (Plastics Europe, 2024).

The construction sector, the world's second-largest consumer of plastics (Plastics Europe, 2024), uses polymer-based materials not only as structural and protective components, but also as reinforcement or fillers in composites to improve their performance (Agarwal & Gupta, 2017). One example is the incorporation of polymer fibres into cement, which is the most commonly used material for fibre reinforcement compared to steel and glass (Ochigue et al., 2025). They improve tensile strength and crack resistance, resulting in more durable building materials, while contributing to lightweight properties and competitive costs (Concrete

Reinforcing Fibre Market Size, Share, 2025). For instance, polymeric fibres lower the amount of steel reinforcement required in concrete pipes exposed to aggressive environments such as sanitary sewers (Peyvandi et al., 2014), while also addressing the problem of steel corrosion (Prasittisopin, 2025).

Polymeric fibres incorporated into cementitious matrices can originate from both virgin and recycled plastics. The incorporation of recycled polymers into construction materials is gaining significant momentum, with the construction sector currently showing the fastest growth in recycled plastic uptake among all the industries (Plastics Europe, 2024). This trend is also driven by increasing legislative pressure to improve recycling rates and reduce waste generation (Horvat et al., 2024). The use of secondary fibres therefore represents a promising approach to achieving high-performance, yet more sustainable composites, in line with the objectives of the EU Circular Economy Action Plan, which encourages circularity and greater use of secondary raw materials in construction (European Commission, 2020). At the same time, fundamental questions remain regarding the stability and durability of these materials and potential environmental trade-offs, including the release of microplastics at various stages of the material's life cycle, from production and use to demolition and subsequent waste handling.

Despite being engineered for long-term durability, construction materials containing plastics inevitably undergo gradual degradation. Mechanical wear, UV exposure and other ageing processes facilitate the breakdown of plastics, leading to the formation and release of microplastics (Yuk et al., 2022), defined as insoluble synthetic polymer particles ranging from 1 μm to 1000 μm (*ISO 24187*, 2023). In the case of fibre-reinforced cement materials, microplastic can detach from the surface of concrete paving blocks as they undergo abrasion and weathering, subsequently entering the environment through urban runoff (Smyth et al., 2025). Furthermore, demolition activities increase microplastic release markedly, as the breaking and crushing of concrete liberate fine particles that can disperse through the air or leach into the surrounding media (Prasittisopin et al., 2023). It has been reported that demolition processes generate substantially higher levels of particulate matter than those observed during regular service life, contributing significantly to air pollution and its associated adverse health effects (Cheng et al., 2021).

Due to their widespread occurrence, persistence and potential impacts on ecosystems and human health, microplastics have become one of the most pressing environmental challenges of recent decades (Ghosh et al., 2023). However, research efforts within the field of microplastics are highly uneven across the sectors. Despite being one of the largest consumers of plastics, the construction industry has received little scientific attention, even though the Irish Environmental Protection Agency (Mahon et al., 2017) highlighted it as potentially the most hazardous sector in terms of microplastic generation. Between 2004 and 2024, construction was mentioned in only 0.6% of all microplastic-related publications (Turk et al., 2025). At the same time, the issue is largely overlooked within the construction industry itself. While much emphasis is placed on reducing CO_2 emissions and improving energy efficiency, the potential release of microplastics from building materials and their environmental and health consequences has yet to receive comparable attention (Prasittisopin, 2025). This knowledge gap underscores the urgent need for focused research to understand better how construction materials, including fibre-reinforced cement, contribute to microplastic pollution, and how such emissions can be monitored and mitigated effectively.

In this study, we examined fibre-reinforced cement incorporating virgin polypropylene (PP) and recycled polyethylene terephthalate (rPET) fibres, focusing on the formation and characteristics of the resulting microplastics. Considering the growing use of recycled materials in construction, the two fibre types were compared, to determine how the fibre origin and composition affect cement adhesion and the properties of the generated microplastics. Microplastic particles from reinforcing fibres, which may form through abrasion or demolition of construction structures, were analysed further for their morphology and density, and leaching experiments were conducted to evaluate their potential influence on water chemistry, specifically, the total organic carbon (TOC).

2 Materials and methods

2.1 Materials

The experiments were carried out using 12 mm polypropylene fibres (f-PP) functionalised specifically for incorporation into cement-based materials as an additive to concrete or mortar. These fibres are manufactured in accordance with

the harmonised technical specification EN 14889-2:2007 (European Committee for Standardisation (CEN), 2006). To reflect circularity considerations and the potential use of recycled materials in cementitious matrices, parallel experiments were also performed with 12 mm polyethylene terephthalate fibres (f-rPET) produced from recycled material. These fibres represent a newer product and are not yet used widely in construction applications; consequently, they have not been surface-functionalised specifically or tailored chemically for incorporation into cementitious systems such as concrete.

Because plastic materials ultimately fragment into microplastics, several analyses were also conducted on pre-prepared microfibres. Polyethylene terephthalate microfibres (μf-rPET) were obtained from the manufacturer as precision-cut fibres of 500 μm (produced from the same material as f-rPET). In contrast, the polypropylene microfibres (μf-PP) were produced in-house by cryogenic milling of the f-PP at -196 °C using a Cryogenic Mixer Mill CryoMill (Retsch GmbH, Germany) in three high-frequency milling cycles (60 s, 30 Hz), with intermediate cooling steps (30 s, 5 Hz) between the cycles.

2.2 Preparation of the cement prisms

The cement prisms were prepared by incorporating f-PP and f-rPET (2 vol%) into the cement matrix to produce fibre-reinforced composites. The fibres were first mixed homogeneously with the dry cement, after which water was added at a water-to-cement ratio (w/c) of 0.5. The mixture was cast into moulds, sealed to prevent moisture loss, and cured under closed conditions for 28 days at 23 ± 2 °C.

2.3 Simulation of surface abrasion and demolition

The release of microplastics from fibre-reinforced cement was simulated under controlled laboratory conditions, using two approaches to represent both the use phase and later demolition. The use phase was simulated through surface abrasion using a hand rasp. The rasp was cleaned thoroughly and fixed in a vice, with paper placed underneath to collect the released particles. The sample prisms were then rubbed manually against the rasp surface. To mimic the mechanical stresses associated with the demolition and subsequent processing of construction waste, the prisms were also subjected to fragmentation using a MixMill MM20 horizontal

vibration ball mill (Domel, Slovenia). The cured prisms were first broken coarsely into pieces of approximately 0.5 g using a chisel and hammer. Milling was then performed with about 2.5 g of material and a single 25 mm stainless steel ball at a frequency of 10 Hz for 30 seconds per cycle, repeated until complete homogenisation was achieved. Following both treatments, microplastic fragments were detected visually under a stereo microscope SMZ-171 (Motic, China).

2.4 Assessing the amount of cement residues adhered to the fibres

The amount of cement adhering to the fibre surface was determined using scanning electron microscopy (SEM), JSM-IT500LV (Jeol, Japan). A controlled crack was induced in the cement prism using a chisel and hammer. The main cement mass was separated carefully, and the protruding fibres were trimmed near the fracture surface using fine scissors. The extracted fibres were transferred carefully onto SEM pin stubs and analysed to assess the morphology of the (micro)fibres and extent of the adhering cementitious material. To quantify the amount of cement attached to the fibres, a custom script was developed in Mathematica. High-resolution SEM images (2000× magnification) were pre-processed and binarised so that the fibre area appeared black (value 0), while the adhering cement residues appeared white (value 1). The surface coverage of fibres by cement was calculated based on the resulting pixel matrix.

2.5 Density measurement

The density of (micro)fibres without cement residues was determined using a 50 mL metal pycnometer and isopropanol. To minimise evaporation, the overflow opening for excess liquid was sealed immediately with a small piece of adhesive tape, and the pycnometer rim was additionally secured with Parafilm. The density of each sample was calculated according to Equation (1), where ϱ is the density of the (micro)fibres, ϱ_l is the density of the liquid, m_1 is the mass of the empty pycnometer, m_2 is the mass of the pycnometer filled with the (micro)fibres, m_3 is the mass of the pycnometer containing both the (micro)fibres and the liquid, and m_4 is the mass of the pycnometer containing the liquid. In addition, the floatability of the (micro)fibres was evaluated using the sink–flow method in a demineralised water and 5% NaCl solution to simulate seawater.

$$\rho = \rho_l \times \frac{m_2 - m_1}{(m_4 - m_1) - (m_3 - m_2)} \quad (1)$$

2.6 Leaching experiment

The leaching of chemical substances from (micro)fibres was conducted in 100 mL Erlenmeyer flasks. Approximately 3 g of (micro)fibres were mixed with 60 mL of demineralised water, corresponding to the standard TCLP solid-to-liquid ratio of 1:20 (U.S. Environmental Protection Agency, 1992). The mixtures were agitated on an orbital shaker at 300 rpm for 3 hours. After agitation, the suspensions were vacuum-filtered through Sartorius filter paper (grade 393). The resulting filtrates were collected in pre-cleaned glass vials and analysed for TOC using a multi N/C 3100 analyser (Analytik Jena, Germany).

3 Results and discussion

3.1 Microplastic generation under simulated wear and demolition

The abrasion simulation produced a fine powder consisting of fragmented cementitious material and short polymer fibres, with approximate dimensions of 400 μm and smaller. In contrast, the simulation of demolition by crushing followed by milling in a horizontal vibration mill under the applied conditions produced a distinctly different product. In this case, the polymer fibres embedded in the cement matrix did not necessarily fragment to the microplastic size range during the initial crushing phase. A microscopic examination revealed fibres ranging from the original 12 mm in length down to microscopic dimensions. Additionally, numerous fibres were observed to be entangled and interconnected by larger cement fragments forming aggregates. As an example, Figure 1 shows the microscopic images of the abraded, as well as the crushed and milled materials derived from the cement prisms with f-rPET.

Based on these observations, it can be concluded that mechanical wear and demolition processes generate microplastics through fundamentally different mechanisms, resulting in various particle size distributions and shapes of the resulting fragments. Abrasion causes primarily progressive surface erosion and fibre fragmentation, while demolition results mainly in the detachment of larger fibre–

cement aggregates that may later degrade into microplastics through secondary processes. These findings highlight the importance of simulating multiple degradation pathways when assessing the potential environmental release of microplastics from fibre-reinforced cement composites.

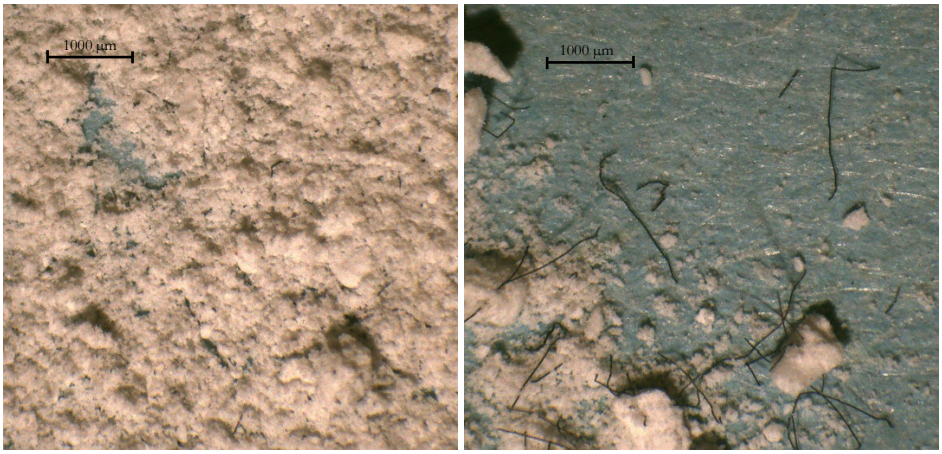

Figure 1: Microscopic images of the material obtained by abrasion (left) and by crushing followed by milling (right) of the cement prisms reinforced with f-rPET.
Source: own.

3.2 Adhesion of cement residues on the (micro)fibres

Based on quantitative surface coverage calculations using a custom-made program in Mathematica, the cement adhered more strongly to f-PP, with an average coverage of 13.4 ± 6.0 %, compared with only 2.4 ± 0.9 % for f-rPET, which is also evident from the SEM micrographs (Figure 2). The extent of cement adhesion to fibres is governed by a combination of mechanical, physical and chemical interactions that are interlinked closely. According to the adsorption theory, good interfacial bonding requires intimate contact between the adhering substrates, and arises from a combination of mechanical interlocking, electrostatic interactions, diffusion processes and adsorption/surface reactions at the interface (Pakravan et al., 2012).

The SEM images of f-PP revealed an intrinsically very smooth surface, which would generally limit mechanical interlocking with the cementitious matrix. In this context, the importance of appropriate surface functionalisation becomes evident. The f-PP

used in this study were treated specifically, in accordance with EN 14889-2:2006 (European Committee for Standardisation (CEN), 2006), to enhance compatibility with cementitious materials and promote interfacial bonding. This surface modification likely contributed to the substantially higher cement coverage observed on f-PP, as it facilitates better wetting and stronger physicochemical interactions at the interface, thereby reducing the tendency of the matrix to slip along the fibre surface.

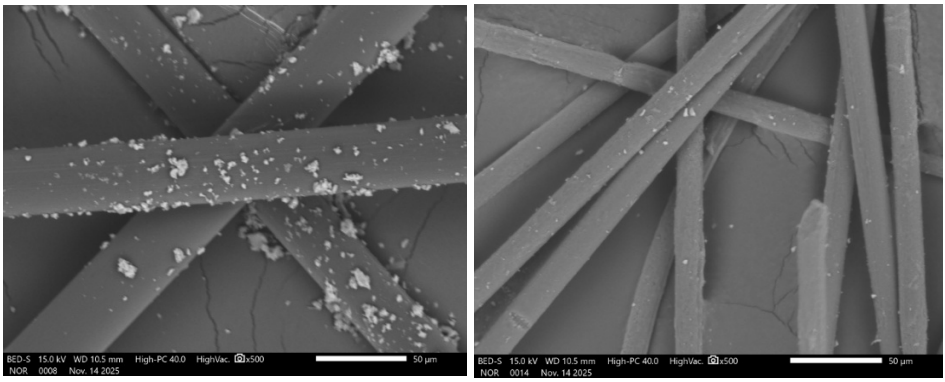

Figure 2: SEM images of f-PP (left) and f-rPET (right).
Source: own.

In contrast, the SEM images of f-rPET at higher magnification (2000×) showed a more irregular and less smooth surface. As these fibres were not functionalised specifically for cementitious applications their surface chemistry does not promote adhesion actively. It is therefore plausible that the limited cement attachment observed on f-rPET arises mainly from mechanical interlocking within these grooves and surface irregularities, rather than from tailored chemical interactions at the interface. In both cases, the cement residues were distributed unevenly along the fibre length, forming a heterogeneous pattern with localised clusters of cement particles separated by nearly clean fibre segments (Figure 2). The adhered residues also varied considerably in size, from fine particles to larger agglomerates, indicating that local microstructural conditions might influence the extent and quality of the fibre–matrix contact.

It is important to note that the strength of attachment of these residues remains unknown, and it is therefore unclear to what extent the attached particles would detach, for example, under mild mechanical stresses, such as sample handling and transport, or under environmental abrasion. This uncertainty is particularly relevant when considering the environmental behaviour of fibres and the microplastics derived from them, as the stability of cement residues on the fibre surface will affect the particle density, fragmentation pathways and, ultimately, their transport and fate in aquatic and terrestrial systems directly (Galafton et al., 2025).

3.3 Density

The density measurements obtained using the pycnometer showed satisfactory agreement with the values reported by the fibre manufacturers (Table 1), confirming the robustness of the applied pycnometry procedure and the choice of isopropanol over water as the measuring liquid. Due to the hydrophobic nature of plastics, the water did not wet the (micro)fibre surface adequately, which led to the trapping of visible air bubbles, and, consequently, to unreliable density measurements. In addition, PP has a lower density than water and therefore floated, contributing further to errors in the step where the excess liquid is displaced from the pycnometer. By contrast, isopropanol wetted the (micro)fibres effectively, reduced air entrapment, and, owing to its lower density, allowed all the (micro)fibres to sink to the bottom of the measuring vessel.

Table 1: Densities of the PP and rPET (micro)fibres compared with the data from the technical data sheets (TDS) available on the internet or provided by the manufacturer.

	Density (TDS)	Density (pycnometer method)
f-PP	920 ± 10 kg/m³ (Treechem, n.d.)	923,9±3,1 kg/m³
µf-PP		893,3 ± 1,3 kg/m³
f-rPET	1370 ± 10 kg/m³ (SwissFlock, n.d.)	1411,98 ± 12,2 kg/m³
µf-rPET		1357,0 ± 4,9 kg/m³

This relatively simple approach proved more suitable than advanced techniques such as gas pycnometry, where the measured densities deviated more markedly from the TDS values, or mercury intrusion porosimetry, which was not appropriate for these materials and produced unusable density data. Beyond that, the good agreement with manufacturer values is also important from the perspective of material validation, as

the density is not only used as a separation parameter for microplastics (Mattsson et al., 2022), but can also support the identification of different polymer types (Barnett et al., 2021). Nevertheless, slight differences were observed between the measured densities of the microfibres and their longer counterparts. These are most likely due to residual air trapped between the individual filaments, a phenomenon that can occur for both fibre lengths, but is more pronounced in the case of microfibres because of their higher specific surface area. Air bubbles occupy volume in the pycnometer without contributing to the total mass, which leads to an apparent underestimation of the true density.

From an environmental perspective, density is a key property governing the behaviour of microplastics, as it controls their distribution within the water column largely, and, consequently, their bioavailability to aquatic organisms (L. Li et al., 2018). The sink–float method tests confirmed the expected behaviour of the tested (micro)fibres: The PP remained at the water surface, whereas the rPET sank to the bottom (Figure 3). The combination of quantitative density measurements with simple flotation experiments provides a robust, yet practical framework for evaluating the environmental behaviour of (micro)fibres, providing both precise density values and direct insight into whether the materials tend to remain at the water surface or sink into deeper layers, where they may change and ultimately accumulate in freshwater or marine sediments, potentially affecting living organisms (Alavian Petroody et al., 2023; Zidar et al., 2024).

Figure 3: Sink-float method for (micro)fibres (from left to right: f-PP, µf-PP, f-rPET, µf-rPET).

Source: own.

However, it must be recognised that cement residues adhering to the (micro)fibre surface can affect their contaminant-dependent density substantially, so (micro)fibres that would otherwise float may begin to sink when a sufficient amount of cement is attached. Due to the practical challenges of isolating enough (micro)fibres with firmly attached cement residues from the cementitious matrix, we were not able to perform reliable pycnometric density measurements on these composite particles. Nevertheless, the qualitative observations in aqueous media showed that fibres carrying cement residues may sink or remain suspended below the surface, in contrast to pristine f-PP, which floated consistently. These findings suggest that cement adhesion can modify the contaminant-dependent density significantly, and, consequently, the environmental transport and fate of fibre-derived microplastics, particularly in aquatic systems.

Once released into the environment, however, the density of microplastics agglomerate can evolve further. Processes such as mechanical abrasion, biofilm formation and other forms of biofouling, as well as weathering and the adhesion of mineral or organic matter, can increase the density of the (micro)fibres progressively. As a result, polymers with intrinsic densities lower than that of water may ultimately be found embedded in sediments. Moreover, while the difference between the density of particles and that of the surrounding water largely controls their settling, depth-related changes in temperature and salinity, and, hence, in water density, introduce additional complexity to their vertical transport (J. Li et al., 2023). Assessing the environmental fate of microplastics is therefore extremely complex, and requires integrating intrinsic material properties, such as density, with dynamic environmental processes.

3.4 Leaching experiment

Measurement of dissolved carbon is one of the commonly used approaches to assess the amounts of leachates released from plastic materials and microplastics. The leaching results are presented in Figure 4. For rPET the TOC values were higher for µf-rPET than for the corresponding f-rPET. This result reflects the larger specific surface area of the smaller particles, which generally enhances the extent of leaching. Accordingly, the leaching data are often normalised to particle surface area and reported as the mass of a released substance per unit surface area (Egea et al., 2024; Romera-Castillo et al., 2018). In contrast, this trend was not observed for PP, where

the TOC values for µf-PP were lower than for the corresponding f-PP. This apparent discrepancy can be explained by the floating nature of the PP, which became more pronounced in the case of µf-PP. While the f-PP could be pushed down into the solution more easily, the µf-PP tended to accumulate as a diffuse layer at the water`s surface and adhered partially to the walls of the Erlenmeyer flasks during shaking. As a result, only a fraction of the µf-PP mass was truly in contact with the aqueous phase, thereby limiting the extent of leaching and leading to lower measured TOC values. This suggests that improved experimental design ensuring more effective contact between the (micro)fibres and the aqueous phase could facilitate more extensive leaching and yield more representative TOC measurements.

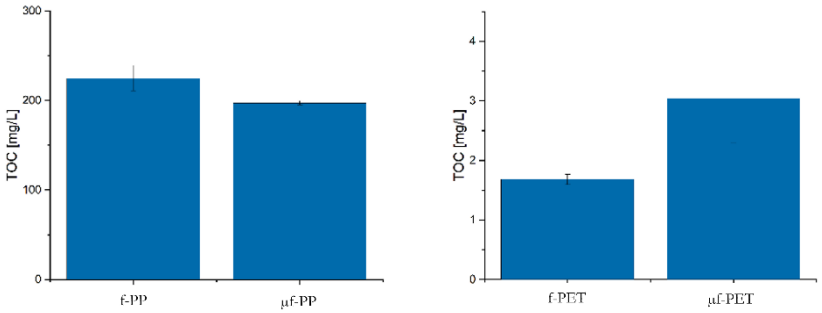

Figure 4: TOC values of the leachates for PP (left) and rPET (micro)fibres (right).
Source: own.

Also, different polymers exhibit distinct leaching behaviours. For example, Yuan et al., 2023 reported more pronounced initial leaching from PP compared with PET under comparable conditions. In addition, commercial fibres contain various additives, (e.g. surfactants, coupling agents, stabilisers), that are introduced to obtain the desired performance. f-PP designed for concrete applications require surface chemistry that promotes good interfacial bonding with the cement matrix, which is consistent with our SEM observations of higher amounts of cement residues adhering to the f-PP surface compared with f-rPET. Under intensive mixing and shaking, such additives can be released into the aqueous phase. This was also evident during filtration, where leachates from the PP (micro)fibres produced pronounced foaming, in contrast to rPET. This behaviour supports the interpretation that plastic-derived additives contributed substantially to the elevated TOC values observed for f-PP and µf-PP in the leaching experiments further.

The TOC levels are also influenced strongly by experimental conditions such as particle concentration, shaking speed, pH of the medium, exposure time and temperature, which makes direct comparison between different studies challenging. For example, leaching typically evolves over time, being most intense during the initial phase and then slowing gradually (Yuan et al., 2023). Our experiment was designed specifically to capture this early, highly dynamic stage, and was conducted under relatively aggressive conditions (high shaking speed and high (micro)fibre concentration). In this light, the higher TOC values observed in our study compared with the literature data can be interpreted as a consequence of the chosen experimental setting (Chen et al., 2024; Yuan et al., 2023). Furthermore, even after filtration, the leachate may still contain nanoplastics, that pass through the filter and are detected as part of the TOC signal together with low-molecular-weight organic leachates (Chen et al., 2024).

Although TOC is inherently a non-specific parameter and does not allow identification of individual leached compounds, it nonetheless serves as a valuable screening tool for comparing leaching behaviour between different materials (e.g., PP vs. rPET, fibres vs. microfibres) and for identifying scenarios in which plastic-derived leachates may represent a relevant contribution to organic loading in ecosystems.

4 Conclusions

In this work we examined how fibre-reinforced cementitious composites can act as a source of microplastics and associated chemical leachates throughout the use phase of the life cycle, from the production of the fibre-cement composite to degradation and demolition. We demonstrate that the characteristics of fibre-derived microplastics from cementitious composites depend strongly on the degradation pathway. Abrasion produced predominantly fine fragments, whereas the applied demolition scenario involving crushing and subsequent milling generated a much broader particle size spectrum, ranging from intact 12 mm fibres to microfibres. These contrasting outcomes highlight that different mechanical processes can lead to distinct microplastic size distributions and morphologies, even when starting from the same material.

We showed further that cement residues can adhere to polymer fibres, and that the extent of this adhesion depends on both the fibre surface treatment and surface morphology. The f-PP functionalised specifically for use in concrete exhibited markedly higher cement coverage than f-rPET. Nonetheless, the less smooth surface of f-rPET still enabled a certain degree of mechanical anchoring of cement residues, despite the lack of targeted functionalisation. This adhesion of cement residues can also modify key properties such as contaminant-dependent density and may shift fibres that would otherwise float towards suspending or sinking behaviour, thereby altering their environmental fate.

Finally, the leaching experiments indicate that, beyond particle size and surface area, the presence of additives used to enhance fibre–cement compatibility likely plays a major role in governing the leachate levels. Together, these findings emphasise that, when assessing the potential environmental impacts of fibre-reinforced cementitious materials, it is essential to consider not only the microplastics themselves, but also the attached cement residues and the functional additives necessary to achieve the required performance of the reinforcing fibres, as these components may appear subsequently in the leachate.

Acknowledgment

This work was supported by the Slovenian Research and Innovation Agency (ARIS) through research program P2-0273 and the Young Researcher Program (Grant no. 59559).

References

Agarwal, S., & Gupta, R. K. (2017). Plastics in Buildings and Construction. In *Applied Plastics Engineering Handbook* (pp. 635–649). Elsevier. https://doi.org/10.1016/B978-0-323-39040-8.00030-4

Alavian Petroody, S. S., Hashemi, S. H., Škrlep, L., Mušič, B., van Gestel, C. A. M., & Sever Škapin, A. (2023). UV Light Causes Structural Changes in Microplastics Exposed in Bio-Solids. *Polymers*, *15*(21), 4322. https://doi.org/10.3390/polym15214322

Awoyera, P. O., & Adesina, A. (2020). Plastic wastes to construction products: Status, limitations and future perspective. *Case Studies in Construction Materials*, *12*, e00330. https://doi.org/10.1016/j.cscm.2020.e00330

Barnett, S., Evans, R., Quintana, B., Miliou, A., & Pietroluongo, G. (2021). An Environmentally Friendly Method for the Identification of Microplastics Using Density Analysis. *Environmental Toxicology and Chemistry*, *40*(12), 3299–3305. https://doi.org/10.1002/etc.5164

Chen, C., Du, R., Tang, J., Wang, B., Li, F., Zhang, Z., & Yu, G. (2024). Characterization of microplastic-derived dissolved organic matter in freshwater: Effects of light irradiation and polymer types. *Environment International*, *185*, 108536. https://doi.org/10.1016/j.envint.2024.108536

Cheng, C.-W., Sheu, G.-T., Chou, J.-S., Wang, P.-H., Cheng, Y.-C., & Lai, C.-Y. (2021). Fine particulate matter PM2.5 generated by building demolition increases the malignancy of breast cancer MDA-MB-231 cells. *Chemosphere*, *265*, 129028. https://doi.org/10.1016/j.chemosphere.2020.129028

Concrete Reinforcing Fiber Market Size, Share (No. FBI106752). (2025). Fortune Business Insights. https://www.fortunebusinessinsights.com/concrete-reinforcing-fiber-market-106752

Egea, L. G., Brun, F. G., & Jiménez-Ramos, R. (2024). Dissolved organic carbon leaching from microplastics and bioavailability in coastal ecosystems. *Science of The Total Environment*, *909*, 168673. https://doi.org/10.1016/j.scitotenv.2023.168673

European Commission. (2020). *A new Circular Economy Action Plan: For a cleaner and more competitive Europe* (No. COM(2020) 98 final). https://eur-lex.europa.eu/legal-content/EN/TXT/HTML/?uri=CELEX:52020DC0098

European Committee for Standardization (CEN). (2006). *Fibres for concrete—Part 2: Polymer fibres—Definitions, specifications and conformity* (No. EN 14889-2:2006). https://www.en-standard.eu/bs-en-14889-2-2006-fibres-for-concrete-polymer-fibres-definitions-specifications-and-conformity/

Galafton, C., Budhiraja, V., Stevens, S., Mušič, B., & Maga, D. (2025). Environmental and littering impacts of disposable cups made of polypropylene and polylactic acid in Germany. *Sustainable Production and Consumption*, *57*, 35–45. https://doi.org/10.1016/j.spc.2025.04.013

Ghosh, S., Sinha, J. K., Ghosh, S., Vashisth, K., Han, S., & Bhaskar, R. (2023). Microplastics as an Emerging Threat to the Global Environment and Human Health. *Sustainability*, *15*(14), Article 14. https://doi.org/10.3390/su151410821

Global plastic production. (2023). Statista. https://www.statista.com/statistics/282732/global-production-of-plastics-since-1950/

Hinton, Z. R., Talley, M. R., Kots, P. A., Le, A. V., Zhang, T., Mackay, M. E., Kunjapur, A. M., Bai, P., Vlachos, D. G., Watson, M. P., Berg, M. C., Thomas H. Epps, & Korley, L. T. J. (2022). Innovations Toward the Valorization of Plastics Waste. *Annual Review of Materials Research*, *52*(Volume 52, 2022), 249–280. https://doi.org/10.1146/annurev-matsci-081320-032344

Horvat, B., Knez, N., Hribar, U., König, J., & Mušič, B. (2024). Thermal insulation and flammability of composite waste polyurethane foam encapsulated in geopolymer for sustainable building envelope. *Journal of Cleaner Production*, *446*, 141387. https://doi.org/10.1016/j.jclepro.2024.141387

ISO 24187:2023—Principles for the analysis of microplastics present in the environment. (2023). https://www.iso.org/standard/78033.html

Li, J., Shan, E., Zhao, J., Teng, J., & Wang, Q. (2023). The factors influencing the vertical transport of microplastics in marine environment: A review. *Science of The Total Environment*, *870*, 161893. https://doi.org/10.1016/j.scitotenv.2023.161893

Li, L., Li, M., Deng, H., Cai, L., Cai, H., Yan, B., Hu, J., & Shi, H. (2018). A straightforward method for measuring the range of apparent density of microplastics. *Science of The Total Environment*, *639*, 367–373. https://doi.org/10.1016/j.scitotenv.2018.05.166

Mahon, A. M., Officer, R., Nash, R., & O'Connor, I. (2017). *Scope, Fate, Risks and Impacts of Microplastic Pollution in Irish Freshwater Systems*. https://doi.org/10.13140/RG.2.2.13353.60005

Mattsson, K., Ekstrand, E., Granberg, M., Hassellöv, M., & Magnusson, K. (2022). Comparison of pre-treatment methods and heavy density liquids to optimize microplastic extraction from natural marine sediments. *Scientific Reports*, *12*(1), 15459. https://doi.org/10.1038/s41598-022-19623-5

Ochigue, P. C. D., Aguilos, M. A., Lubguban, A. A., & Bacosa, H. P. (2025). Circular Economy Solutions: The Role of Thermoplastic Waste in Material Innovation. *Sustainability*, *17*(2), 764. https://doi.org/10.3390/su17020764

Pakravan, H. R., Jamshidi, M., Latifi, M., & Chehimi, M. M. (2012). Polymeric fibre adhesion to the cementitious matrix related to the fibres type, water to cement ratio and curing time.

International Journal of Adhesion and Adhesives, *35*, 102–107. https://doi.org/10.1016/j.ijadhadh.2012.02.006

Peyvandi, A., Soroushian, P., & Jahangirnejad, S. (2014). Structural Design Methodologies for Concrete Pipes with Steel and Synthetic Fiber Reinforcement. *Aci Structural Journal*, *111*, 83–92. https://doi.org/10.14359/51686432

Plastics Europe. (2024). *The Circular Economy for Plastics – A European Analysis 2024*. https://plasticseurope.org/knowledge-hub/the-circular-economy-for-plastics-a-european-analysis-2024/

Porta, R. (2021). Anthropocene, the plastic age and future perspectives. *FEBS Open Bio*, *11*(4), 948–953. https://doi.org/10.1002/2211-5463.13122

Prasittisopin, L. (2025). Unveiling the duality of cement and concrete addressing microplastic pollution: A review. *Environmental Science and Pollution Research*, *32*(14), 8717–8742. https://doi.org/10.1007/s11356-025-36267-w

Prasittisopin, L., Ferdous, W., & Kamchoom, V. (2023). Microplastics in construction and built environment. *Developments in the Built Environment*, *15*, 100188. https://doi.org/10.1016/j.dibe.2023.100188

Romera-Castillo, C., Pinto, M., Langer, T. M., Álvarez-Salgado, X. A., & Herndl, G. J. (2018). Dissolved organic carbon leaching from plastics stimulates microbial activity in the ocean. *Nature Communications*, *9*(1), 1430. https://doi.org/10.1038/s41467-018-03798-5

Shamsuddoha, M., & Kashem, M. A. (2024). Zero Plastic Drive: A Comprehensive Review on Unveiling Innovative Sustainable Solutions for a Circular Plastics Economy. *Sustainability*, *16*(23), 10329. https://doi.org/10.3390/su162310329

Smyth, K., Tan, S., Van Seters, T., Henderson, V., Passeport, E., & Drake, J. (2025). Pavement wear generates microplastics in stormwater runoff. *Journal of Hazardous Materials*, *481*, 136495. https://doi.org/10.1016/j.jhazmat.2024.136495

Stoett, P., Scrich, V. M., Elliff, C. I., Andrade, M. M., de M. Grilli, N., & Turra, A. (2024). Global plastic pollution, sustainable development, and plastic justice. *World Development*, *184*, 106756. https://doi.org/10.1016/j.worlddev.2024.106756

SwissFlock. (n.d.). *Material safety data sheet—Polyester (PET) Precision cut flock*.

Treechem. (n.d.). *Technical Datasheet—Polypropylene fiber*. Retrieved December 2, 2025, from https://www.treechem.com.mx/pdf/TDS%20POLYPROPYLENE%20FIBER.pdf

Turk, K., Kalčíková, G., Jemec Kokalj, A., & Mušič, B. (2025). From plastic use in the construction and built environment to state-of-the-art circular economy solutions to combat microplastic pollution. *Environmental Sciences Europe*, *37*. https://doi.org/10.1186/s12302-025-01228-0

U.S. Environmental Protection Agency. (1992, July). *Test Methods for Evaluating Solid Waste, Physical/Chemical Methods, Method 1311: Toxicity Characteristic Leaching Procedure (TCLP)*. U.S. Environmental Protection Agency. https://www.epa.gov/sites/default/files/2015-12/documents/1311.pdf

Yuan, M., Xiang, H., Tong, Y., Zhou, K., Peng, C., & Chen, W. (2023). Spectroscopic Tracking of the Characteristics of Microplastic-Derived Dissolved Organic Matter. *Separations*, *10*(2), 101. https://doi.org/10.3390/separations10020101

Yuk, H., Jo, H. H., Nam, J., Kim, Y. U., & Kim, S. (2022). Microplastic: A particulate matter(PM) generated by deterioration of building materials. *Journal of Hazardous Materials*, *437*, 129290. https://doi.org/10.1016/j.jhazmat.2022.129290

Zidar, P., Kühnel, D., Škapin, A. S., Skalar, T., Drobne, D., Škrlep, L., Mušič, B., & Jemec Kokalj, A. (2024). Comparing the effects of pristine and UV–VIS aged microplastics: Behavioural response of model terrestrial and freshwater crustaceans. *Ecotoxicology and Environmental Safety*, *285*, 117020. https://doi.org/10.1016/j.ecoenv.2024.117020

Prediction of Hydrophobic Properties in Biopolymer-Based Coatings via Formulation Data Modelling

Anja Verbič,[1] Vuk Martinović,[1] Rubén Saborido,[2] Antonio Borrego,[3] Mariano Luque,[3] Uroš Novak,[1] Blaž Likozar[1], Blaž Stres[1]

[1] National Institute of Chemistry, Department of Catalysis and Chemical Reaction Engineering, Ljubljana Slovenia
anja.verbic@ki.si, vuk.martinovic@ki.si, uros.novak@ki.si, blaz.likozar@ki.si, blaz.stres@ki.si
[2] University of Málaga, Institute for Software Engineering and Software Technology "Jose Maria Troya Linero", Málaga, Spain
rsain@uma.es
[3] University of Málaga, Department of Applied Economics (Mathematics), Málaga, Spain
antoniobo@uma.es, mluque@uma.es

The urgent need to replace environmentally persistent and toxic per- and polyfluoroalkyl substances (PFAS) in hydrophobic coatings, has driven the exploration of renewable biopolymers as sustainable alternatives. Biopolymer-based coatings, derived from chitosan, cellulose or starch, are promising alternatives, but optimising their formulations to achieve targeted performance remains challenging. The traditional experimental approaches are time-consuming and resource-intensive. This study integrated a simple linear regression (SLR) technique based on ordinary least squares (OLS) to model the relationship between the formulations` composition and resultant surface water contact angles (WCA) achieved when the coatings are applied on textiles. An SLR/OLS model was applied to experimental data of biopolymer mixtures to predict the WCA, based on the presence and ratios of coating components. The model predicted the WCA values accurately, proving the potential for guiding the design of multifunctional coatings, by enabling rapid screening and optimisation of the formulations, reducing reliance on extensive laboratory experimentation and consumption of chemicals.

DOI
https://doi.org/10.18690/um.fkkt.1.2026.10

ISBN
978-961-299-130-2

Keywords:
biopolymers, functional materials, coatings, PFAS, data modelling, simple linear regression

University of Maribor Press

1 Introduction

The environmental and health concerns associated with per- and polyfluoroalkyl substances (PFAS) have accelerated the search for sustainable hydrophobic coatings. While PFAS are used widely for imparting hydrophobicity and oleophobicity in textile and packaging materials, they are persistent, bioaccumulative and proven to be toxic. Biopolymers, such as chitosan, cellulose and starch, represent a promising alternative capable of forming functional coatings (Verbič et al. 2025, Golja et al. 2025, Calvo et al. 2024). However, developing and optimising these formulations to achieve the desired functional properties remains difficult, due to complex interactions between the compounds. The traditional experimental approaches rely on repetitive synthesis and testing, which is labour-consuming and resource-intensive and limits the pace of innovation. To overcome these challenges, this research proposes a new approach, based on simple linear regression (SLR), to accelerate and target the development of coating formulations better. By correlating the formulation parameters with functional performance, measured as the water contact angle (WCA), this method enables more efficient and predictive design of hydrophobic coatings.

Recent advances in machine learning (ML) have introduced powerful data-driven workflows for modelling and even inverse design of different formulations in material development (Xie et al., 2025; Wheatle et al., 2020). ML methods can capture complex nonlinear relationships in high-dimensional formulation spaces and complement the classical statistical approaches. In practice, most formulation development systems exhibit nonlinear behaviour due to complex mixtures and interactions between the compounds, which traditionally necessitates the use of more advanced statistical tools. Among these, full quadratic polynomial regression, typically implemented within the framework of response surface methodology (RSM) is applied widely for optimisation. RSM uses regression-based mathematical models to describe how the formulation variables influence the material properties to identify optimal compositions (Chen & Chen, 2025; Elganidi et al., 2022). While these models require only marginally more computational power than SLR, they demand more deliberate experimental design, larger datasets, and more extensive analysis to account for the curvature and interaction effects between the components. However, *in silico* workflows do not always require highly complex models at the earliest stages. In fact, SLR remains a valuable and underexplored tool

for preliminary screening, which can provide a valuable starting point for narrowing down viable formulations.

Despite the fact that SLR models capture only first-order relationships, they are fast, interpretable and effective for preliminary screening. SLR models capture the relationships between variables using a straight line, known as a regression line. This line represents the best fit through the data points (i.e., the best representation of correlation between the variables), and is chosen to maximise the accuracy of model predictions (Miller et al., 2022). Using a regression line, the relationships between the formulation variables (e.g., the presence of different compounds and their ratios) and material responses (e.g., the WCA of the final coated material) can be computed easily. The line of regression is defined by a set of parameters, and there are several methods available for obtaining the estimates of these parameters. One of the methods is ordinary least squares (OLS), arguably the most popular method for estimating the parameters (Su, 2012). It is based on minimising the quantity of the residual sum of squares – residuals being the vertical distances from the fitted line and the measured y-values (Weisberg, 2005). Using this approach, a range of promising candidate formulations can be generated, which can then be refined using more advanced methods, or validated through actual experimental testing. Notably, our literature review revealed that there are no published studies investigating the use of SLR models for prediction of the targeted properties of biopolymer coating formulations, highlighting the need to evaluate the potential of this *in silico* screening followed by targeted experimental verification to support the development of biopolymer blends with desired functional properties in a more efficient manner.

Through data-driven modelling, the correlation between the formulation composition and hydrophobic performance of the coated end-product can be explored systematically, providing valuable insights for optimising coating recipes. The data-driven model enables the predictions of new formulations, based on modified ratios and concentrations of the existing compounds, that have not been yet explored experimentally, along with the corresponding WCA values that these formulations are expected to achieve. This allows researchers to prioritise only the most promising candidates for laboratory validation, thereby reducing the reliance on extensive experimentation. Our study explores whether SLR is an appropriate model, and to what extent strong agreement between the generated predictions and experimentally measured properties is provided, thereby assessing its suitability as a

reliable early-stage screening method that can support resource-efficient and environmentally responsible laboratory development.

2 Materials and methods

2.1 Materials and coating preparation

Six coating compounds were used for the coating formulations: deionised water, alkyl ketene dimer (Melamin d.d., Kočevje, Slovenia), sodium alginate (Sigma-Aldrich, Steinheim, Germany), cellulose nanofibrils (Sappi Valida, Maastricht, Netherlands), corn starch (Sigma-Aldrich, Steinheim, Germany), and agar (Sigma-Aldrich, Steinheim, Germany). Each component was dispersed in water and mixed in a blender. The formulations were prepared by combining these compounds in defined ratios, depending on the specific mixture certain compounds were included, while others were not, resulting in a diverse set of coatings. All the formulations were prepared fresh, and applied immediately to the textile substrates to ensure consistent coating formation. The coated textiles were then dried under controlled laboratory conditions prior to the WCA measurements (Verbič et al., 2025).

2.2 Characterisation of the hydrophobicity

The surface wettability of the coated samples was determined by measuring the WCA values using a tensiometer (Theta T200, Biolab scientific, Sweden). A 3 μL droplet of water was placed on the coated textile surface and the contact angle was measured after 5 seconds. Three measurements were performed on each sample.

2.3 Data preparation, modelling and validation

The dataset consisted of 12 different coating formulations (and an additional uncoated sample) with 11 variables, each described by the relative concentrations of each compound present in the mixture (6 variables) and sample preparation (2 variables), and three measurements of the WCA values of the final coated sample (3 variables), i.e., 312 datapoints.

To develop a predictive model capable of capturing the relationship between the formulation variables and the resulting WCA accurately, an SLR framework was adopted based on the OLS method. Within this framework, the WCA value was treated as the dependent response variable, while the relative percentages of the six components present in the coating formulation were incorporated as explanatory predictors. This setup allowed us to quantify how variations in the formulation composition influenced the observed wettability of the coating surface.

The trained model was then used to generate new, computationally predicted formulations, by sampling within the experimentally feasible ranges of these three input variables. The predicted formulations were then synthesised in the wet-lab following the predicted composition, and evaluated using the same coating and WCA measurement procedures as the initial samples. The newly measured data were incorporated into the dataset for further model refinement.

3 Results and Discussion

To investigate whether an SLR model can support early-stage formulation screening for targeted development reliably, the modelling workflow was structured into four consecutive steps: i) data acquisition from wet-lab experiments, ii) model training, iii) forward projection, and iv) experimental verification with a database update (Figure 1). This combined experimental-computational loop ensured that the model was developed on real experimental inputs, and that its predictions could be validated and improved.

The input data consisted exclusively of the experimentally produced biopolymer coating formulations and their measured WCA values. For every mixture the compositional variables and the corresponding WCA values of the coated samples were inserted into the dataset. The dataset was inspected for inconsistencies and missing entries, and organised to allow meaningful comparison across the formulations. Before fitting the regression model, the independent experimental measurements obtained for each mixture were averaged to yield a single representative value. This averaging procedure reduced the measurement noise, and ensured that the response variable reflected a consistent estimate of the true WCA for each formulation. The model was trained using the dataset of input variables. Its purpose was not only to reproduce the measured results, but to determine whether

a linear relationship could provide accurate WCA predictions for practical use, and to justify SLR as an appropriate screening tool. The model was then fitted to the dataset to identify relationships between the formulations parameters and measured WCA.

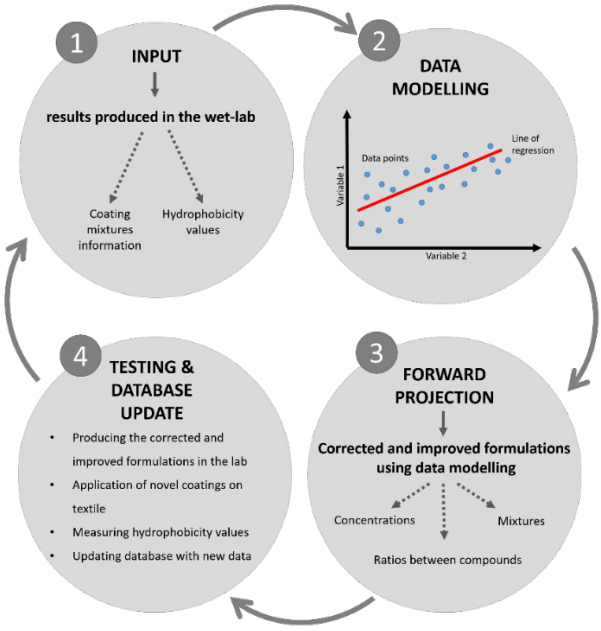

Figure 1: Schematic presentation of the experimental modelling workflow.

The SLR framework based on the OLS method was used to perform the forward projection. The OLS estimator operates by minimising the sum of squared residuals between the observed and predicted values, thereby providing the best linear approximation under the classical assumption that the residual errors are normally distributed with constant variance. This property makes OLS particularly suitable for identifying linear trends in experimental data, and for evaluating the relative importance of the individual formulation variables.

Upon fitting the model, statistical analysis revealed that only three of the six formulation variables (compounds present in the mixture), denoted here as p_1, p_2, p_3, exerted significant effects on the WCA at conventional confidence levels. The remaining variables did not demonstrate statistically meaningful contributions,

suggesting that the wettability of the coating is governed primarily by these three key measurements. The resulting regression model can therefore be expressed in the following general form, Equation (1):

$$WCA = \beta_0 + \beta_1 p_1 + \beta_2 p_2 + \beta_3 p_3 + \epsilon, \quad (1)$$

where WCA is the dependent variable, β_0 represents the intercept term, $\beta_1, \beta_2, \beta_3$ are the estimated regression coefficients associated with the significant formulation variables, and ϵ denotes the residual error term. This model provides a parsimonious yet effective representation of the relationship between formulation composition and surface wettability, and serves as the foundation for the subsequent predictive and experimental validation efforts.

Based on these results, a new dataset was constructed by sampling random compositions systematically within the experimentally feasible ranges defined for the three selected variables. The predicted formulations remained within the chemical space already covered by the experimental work, ensuring practical synthesisability. For each adjusted formulation (i.e. the adjusted ratios between the compounds), the corresponding predicted WCA values using the established model were computed, representing an expected hydrophobic performance. This represents the key results of the modelling stage: the model proposed improved variation of the known formulation and predicted the WCA they should achieve upon testing in the lab. The process allowed to generate a diverse set of formulations that captured a wide spectrum of possible outcomes within the defined parameter space. The resulting dataset not only broadened the scope of the analysis, but also provided a controlled framework for testing the predictive capabilities of the model. In the next stage, these formulations were subjected to experimental validation, enabling us to assess both the accuracy and the robustness of the predictive model rigorously under real-world laboratory conditions. Such validation was crucial to determine whether the model can guide formulation design reliably and ultimately accelerate the discovery of optimised material properties.

To evaluate the predictive performance of the SLR model, a validation step was carried out using formulations newly generated by the model. These formulations were prepared in the wet-lab, according to the predicted compound ratios, applied to textile substrates following the same application protocol used for the initial

samples. The WCA measurements were then performed, to obtain the corresponding experimental hydrophobicity values. The validation process produced two important outcomes. First, the measured WCA values were compared to the model predictions to evaluate the prediction accuracy. The comparison between the predicted and experimentally measured WCA demonstrated that the SLR framework based on the OLS method generated a reliable model in predicting the hydrophobic performance within the range of formulations already explored, confirming its suitability for early-stage screening. In the newly synthesised, model-predicted formulations, the experimentally measured WCA values matched the projected values closely (within 10 %), indicating that the functional properties of the coating were predicted accurately by the model. Notably, several formulations even exceeded their predicted WCA. Second, all the newly obtained data were incorporated into the existing data, to improve the model`s robustness for future iterations and amendments with additional formulation data from other experiments to broaden the exploration of the chemical space.

The results confirm that the SLR framework based on the OLS method can support early-stage screening effectively in the field of Biopolymer-based hydrophobic coatings` development. While the model did not introduce new compounds into the formulation, it predicted new ratios between the existing compounds with increasing WCA successfully, allowing the targeted refinement of formulations without extensive laboratory testing. The ability to predict WCA for adjusted formulations with increased WCA provides a practical decision-making tool for optimising hydrophobic performance in the complex formulation gradients. The predicted WCA values showed a strong agreement with the experimental measurements, establishing SLR/OLS modelling as a valuable tool that can capture dominant trends in small datasets.

4 Conclusions

This study demonstrates that data-driven modelling provides an effective and sustainable approach for developing biopolymer-based hydrophobic coatings as alternatives to PFAS. By applying the SLR framework based on the OLS method, the correlation between coating composition and WCA was modelled successfully, allowing reliable prediction of the hydrophobic performance with increased WCA values. Despite being performed on a relatively small dataset using fewer than 350

data points, the model achieved high predictive accuracy and identified an improved variant of the existing formulations successfully, which were validated experimentally. The integration of data modelling into the formulation development supported rapid screening and optimisation of the coating composition, reducing the experimental workload, material consumption and environmental impact significantly, while accelerating the pace of innovation. Future work will focus on expanding the dataset, exploring other models and incorporating additional variables, which will improve the predictive performance and broaden the model's applicability further.

Acknowledgment

This research was supported by the Horizon Europe project PROPLANET (Grant agreement number 10109842) and the Slovenian Research Agency (Research Core Funding No. P2-0152).

References

Calvo O., Blanes M., Sirvent E.A., Pastor Climent B., Verbič A., Stres B., Golja B., Novak U., Likozar B. (2024). Desarrollo de acabados textiles libres de PFAS mediante alternativas biobasadas. Proceedings of XI Congreso I+D+i, Campus d'Alcoy : Creando sinergias, pp.365-370.

Chen, H. Y., & Chen, C. (2025). Importance of Using Modern Regression Analysis for Response Surface Models in Science and Technology. *Applied Sciences*, *15*(13), 7206.

Elganidi, I., Elarbe, B., Ridzuan, N., & Abdullah, N. (2022). Optimisation of reaction parameters for a novel polymeric additives as flow improvers of crude oil using response surface methodology. *Journal of Petroleum Exploration and Production Technology*, *12*(2), 437-449.

Golja B., Stres B., Novak U., Likozar B., Verbič A. (2025). Eco-friendly hydrophobic textiles: a shift from PFAS to sustainable bio-polymers. Proceedings of crossing boundaries: 50th International Symposium on Novelties in Textiles. p.123-129.

Miller, A., Panneerselvam, J., & Liu, L. (2022). A review of regression and classification techniques for analysis of common and rare variants and gene-environmental factors. *Neurocomputing*, *489*, 466-485.

Su, X., Yan, X., and Tsai, C. (2012). Linear regression. *Wiley Interdisciplinary Reviews Computational Statistics*, *4*, 275–94.

Verbič A., Stres B., Jerman I., Golja B., Žagar E., Martinović V., Logar P., Lavrič G., Prašnikar A., Likozar B., Novak U., Oberlintner, A. (2025). Breaking free from PFAS: biocompatible, durable and high-performance octenyl succinic anhydride (OSA)-modified starch/chitosan coating with ZnO for textile applications. *Carbohydrate Polymers*, 123792.

Weisberg, S. (2005). Applied linear regression. *John Wiley & Sons, 528,* 21-22.

Wheatle, B. K., Fuentes, E. F., Lynd, N. A., & Ganesan, V. (2020). Design of polymer blend electrolytes through a machine learning approach. *Macromolecules*, *53*(21), 9449-9459.

Xie, C., Qiu, H., Liu, L., You, Y., Li, H., Li, Y., ... & An, L. (2025). Machine learning approaches in polymer science: Progress and fundamental for a new paradigm. *SmartMat*, *6*(1), e1320.

DOI
https://doi.org/10.18690/um.fkkt.1.2026.11

ISBN
978-961-299-130-2

A Business Model Framework for Scaling Bioleaching Technology: From Laboratory to Semi-Industrial Applications for CRM Recovery from E-Waste PCBs

Dragica Marinič,[1] Miha Štruc,[1, 2]
Anastasia-Maria Moschovi,[3] Iakovos Yakoumis,[3]
Primož Oprčkal [1]

[1] Slovenian National Building and Civil Engineering Institute (ZAG), Ljubljana, Slovenia
dragica.marinic@zag.si, miha.struc@zag.si, primoz.oprackal@zag.si
[2] Jožef Stefan International Postgraduate School, Ljubljana, Slovenia
miha.struc@zag.si
[3] Monolithos Catalysts and Recycling Ltd., Athens, Greece
yakoumis@monolithos-catalysts.gr, moschovi@monolithos.gr

Innovative technological solutions for waste electrical and electronic equipment are critical for circular and sustainable economy. E-waste, generating 57.4 million tonnes annually, includes around 6 million tonnes of printed circuit boards (PCBs), which are rich in critical raw materials (CRMs) such as copper, nickel, zinc, cobalt, lead, and chromium. Despite this potential, less than 40% of e-waste is recycled in the EU. Bioleaching, employing acidophilic autotrophic bacteria to extract metals at ambient temperature, provides a sustainable alternative to pyrometallurgical and hydrometallurgical methods, yet industrial-scale deployment remains challenging. This study presents a complete bioleaching value chain—from mechanical pre-treatment and froth flotation to stirred-tank bioleaching and solvent extraction—demonstrated at three reactor scales (2 L, 20 L, and 100 L) over 30 days at 30 °C. Metal recovery was quantified by X-ray fluorescence. At 2 L, a mixed *Acidithiobacillus ferrooxidans*/*A. thiooxidans* inoculum recovered 47.3% Cu, 93.4% Ni, and 96.3% Cr. At 20 L, *A. thiooxidans* achieved 64.3% Cu and 90.3% Ni, and at 100 L, recoveries reached 53.5% Cu and 92.0% Ni. Coupled with an estimated 64% reduction in CO_2 emissions, these results confirm that bioleaching is a technically viable and commercially deployable method for CRM recovery from e-waste.

Keywords:
e-waste,
PCBs,
bioleaching,
Acidithiobacillus ferrooxidans,
Acidithiobacillus thiooxidans

University of Maribor Press

1 Introduction

Innovative technological solutions for waste electrical and electronic equipment (WEEE or e-waste) are crucial for the transition to a circular and sustainable economy and a key priority for the European Union (EU). According to the European Commission (EC), the circular economy rate in the EU was 11.8% in 2023, a slight increase compared to 2022 (EC, 2023).

The rapid proliferation of electronic devices has created one of the world's fastest-growing waste streams. In 2021, global e-waste reached 57.4 million tonnes, with printed circuit boards (PCBs) alone accounting for approximately 6 million tonnes (Baldé et al., 2024). PCBs contain copper, nickel, zinc, cobalt, lead, chromium and precious metals at levels often matching or exceeding those found in primary ores, making them a strategically important secondary raw material. The EU Directive 2012/19/EU on WEEE and the Critical Raw Materials Act both mandate higher recycling rates, yet less than 40% of e-waste is recovered currently (Lundberg, 2025).

Metal recovery from e-waste has relied mainly on pyrometallurgical and hydrometallurgical processes. Pyrometallurgy uses high temperatures to separate the metals, while hydrometallurgy employs acids and chemical leaching to dissolve the metal ions from the solid waste (Debbarma et al., 2023; Dhiman, 2023). Although effective, both methods consume large amounts of energy and chemicals and generate hazardous residues, making them unsustainable in the long term (Upadhyay and Ramayya, 2023). These drawbacks have encouraged researchers to explore greener and more sustainable recovery technologies, such as bioleaching. Bioleaching, which uses bacteria such as *Acidithiobacillus ferrooxidans* and *Acidithiobacillus thiooxidans* to extract critical raw materials (CRMs) with much lower environmental impact and relatively low cost, is one of the most important areas of laboratory research in the field of Innovative Technological Processes for E-waste Recycling (Manikandan et al., 2021; Ji et al., 2024; Marinič et al., 2025).

However, most research of this kind ends in the laboratory testing phase (Technology Readiness Levels (TRL 4–5)), as the transition to a pilot or semi-industrial scale (TRL 7) requires greater financial investment, additional research to adapt the process to a bigger scale and a longer validation period (Ellwood et al., 2020; EC, 2022). This has led to the emergence of the so-called 'funding gap' or

'valley of death', which can be overcome through public–private partnerships, among other things (Probst et al., 2013).

Our research is a part of the WEEE-NET9.SPEED project, and is a good practical example where this phenomenon has been eliminated with the financial support of EIT RawMaterials. It is an upgrade of the WEEE-NET9 project, which was finalised in 2024, and enabled the transfer of the knowledge and implementation of bioleaching technology from the laboratory scale to pilot and semi-industrial scales (TRL 7) in the company Monolithos Catalysts & Recycling Ltd (Athens, Greece).

Despite strong laboratory performance – copper recoveries exceeding 95% have been reported in the literature under optimised small-scale conditions (Arshadi et al., 2019; Fu et al., 2021) – the scale-up of bioleaching beyond the bench scale is reported rarely. The transition from a well-controlled 2 L laboratory reactor to a 20 L pilot or 100 L semi-industrial vessel introduces substantial engineering challenges: less uniform mixing, reduced oxygen transfer efficiency, pH and temperature gradients, and greatly increased logistical demands for sterile inoculum production. These challenges halt development at the laboratory stage frequently.

This study presents the results of a structured three-stage scale-up campaign conducted at ZAG (Slovenian National Building and Civil Engineering, Ljubljana, Slovenia) and Monolithos Catalysts & Recycling Ltd (Athens, Greece), progressing from 2 L through 20 L to 100 L. The article describes the complete processing chain from PCB shredding to solvent extraction, and presents XRF-based solid-phase metal removal as the primary evidence of the bioleaching performance at each scale.

2 Process of the Value Chain and Business Model

The bioleaching process demonstrated here is structured as a modular five-stage service chain, summarised in the process flow diagram – business model (Figure 1). Each stage can be offered independently, or as an integrated package to WEEE recycling clients. The chain progresses from raw PCB collection through mechanical preparation, bacterial leaching, liquid–solid separation and solvent extraction, to generate market-ready metal concentrates.

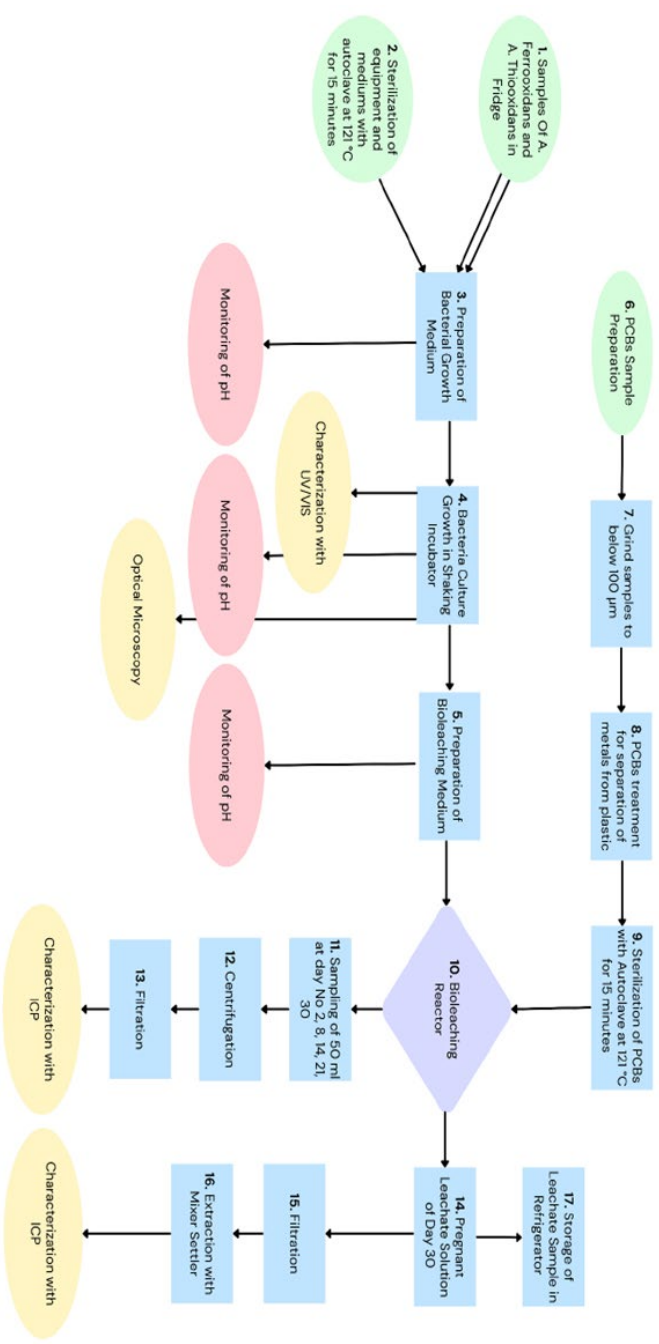

Figure 1: Flow chart of the experiment
Source: own.

2.1 Stage 1: Mechanical Pre-Treatment and Plastic Separation

PCBs of the first and second grades are sourced from decommissioned LCD displays, laptops, tablets and industrial electronics. The feedstock is compositionally heterogeneous: LCD boards have standard copper tracks with tin–lead solder, while laptop boards contain thicker copper layers, lead-free solder and surface finishes such as ENIG (Electroless Nickel Immersion Gold) or immersion silver. Higher-grade laptop boards are enriched disproportionately in gold and nickel, making feedstock characterisation an important initial step.

Pre-treatment starts with manual dismantling to remove the large discrete components (batteries, capacitors, connectors). The boards are then processed through an industrial cutting machine to produce centimetre-scale fragments, which enter a grinding circuit. After each pass the material is sieved; oversized fragments are returned for re-grinding until the entire batch passes through a 125 μm aperture sieve, producing a fine metallic powder in which the individual PCB layers are fully disaggregated. This controlled particle size is critical: finer material maximises the surface area for bacterial attack while avoiding excessive energy consumption.

Before entering the bioleaching process, the ground material undergoes froth flotation. This step exploits the difference in hydrophobicity between plastics and the denser metallic fraction: air injected through the slurry carries hydrophobic plastic particles to the surface, where they overflow with the froth, while the metallic concentrate sinks and is collected. Retaining significant amounts of plastic in the bioleaching reactor suppresses bacterial activity, increases acid consumption, and introduces organic contamination that interferes with the downstream solvent extraction. The separated metallic fraction is then sterilised by autoclaving at 121 °C for 15 minutes before entering the reactor, to prevent external microorganisms from competing with the inoculated culture.

2.2 Stage 2: Bacterial Culture Preparation

Two bacterial strains are used: *Acidithiobacillus ferrooxidans* (DSM 583) and *Acidithiobacillus thiooxidans* (DSM 9463), both obtained from the German Collection of Microorganisms and Cell Cultures (DSMZ). Both are acidophilic, chemoautotrophic bacteria commonly found in acidic, metal- or sulphur-rich

environments. *A. ferrooxidans* oxidises ferrous iron (Fe^{2+}) to ferric iron (Fe^{3+}), the primary oxidant responsible for attacking metal alloys in the PCB matrix, while *A. thiooxidans* oxidises the reduced sulphur compounds to sulphuric acid, lowering the solution pH below 2 and maintaining the acidic conditions required for metal solubilisation.

A key practical constraint identified during scale-up was that *A. ferrooxidans* growth could be maintained reliably only in the 2 L experiment, which was conducted in a dedicated sterile laboratory environment. At 20 L and 100 L, logistical constraints and contamination risks in a shared research facility restricted the inoculum to *A. thiooxidans* alone. This finding has important implications for future scale-up: maintaining dual-strain inoculum at larger volumes requires dedicated sterile fermenters for inoculum production, separated from the main reactor facility.

2.3 Stage 3: Bioleaching Reactor Operation

The bioleaching step is performed in stirred-tank reactors at three volumes. In all cases, the e-waste loading is 15 g/L, aeration is continuous via air pumps, the temperature is 30 °C and each run lasts 30 days. The bioleaching medium differs between scales: the 2 L experiment used a MIX medium (pH 2.5) formulated to support both bacterial strains simultaneously, containing per litre $(NH_4)_2SO_4$ 4.00 g, KCl 0.10 g, K_2HPO_4 0.50 g, $MgSO_4 \cdot 7H_2O$ 0.50 g, $Ca(NO_3)_2$ 0.01 g, $FeSO_4 \cdot 7H_2O$ 22.10 g, and elemental sulphur 5.00 g. The 20 L and 100 L experiments used an S-medium (pH 2.5) formulated for *A. thiooxidans* alone, containing per litre $(NH_4)_2SO_4$ 0.40 g, K_2HPO_4 3.00 g, $MgSO_4 \cdot 7H_2O$ 0.50 g, $FeSO_4 \cdot 7H_2O$ 0.01 g, and elemental sulphur 10.00 g.

The reactor contents are pre-conditioned for 24 hours – medium and PCB powder mixed without bacteria — after which the pH is adjusted to 2.5 using concentrated H_2SO_4 and the bacterial inoculum (10 % v/v) is added. Samples are collected on days 0, 2, 8, 14, 21, and 30 under a strict sterile technique: the workspace is cleaned with 70 % ethanol; a 100 mL aliquot is withdrawn by peristaltic pump and centrifuged at 9,000 rpm for 10 minutes to separate the solid from the supernatant. The supernatant is filtered through a 0.22 μm membrane; 15 mL is transferred to ICP cups and refrigerated; the remainder is frozen for archiving. The solid pellet is

retained from each sampling day. A control reactor without bacterial inoculation is run in parallel, and sampled at day 21 to quantify the abiotic dissolution.

2.4 Stage 4: Liquid–Solid Separation and Solvent Extraction

At the end of the 30-day run, the entire reactor contents are filtered through a 15-20 μm filter press to separate the pregnant leach solution (PLS) from the depleted solid residue. The solid cake is dried, weighed and submitted for XRF analysis to quantify the residual metal content. The PLS – containing dissolved copper, nickel, zinc, cobalt and iron in an acidic sulphate matrix – is processed through a mixer-settler solvent extraction (SX) circuit. An oxime-based organic extractant transfers copper selectively into the organic phase; the loaded organic is stripped with dilute sulphuric acid to yield a copper-rich aqueous concentrate suitable for electrowinning or direct sale as copper sulphate. The copper-depleted raffinate is treated for nickel and zinc recovery. Under optimised conditions at the 100 L scale, the Cu SX efficiency reached 75-85 %, Ni 30-45 % and Fe 60-75 %, with a raffinate pH of approximately 2.4-2.6.

2.5 Commercial Framework

The modular nature of the process enables several independent service offerings: feedstock characterisation and bioleachability assessment, bench-scale or pilot-scale bioleaching trials, and integrated SX with product generation. A patent application for the process has been submitted to the Slovenian Intellectual Property Office. The process achieves approximately 64 % less CO_2 per kilogram of treated PCBs compared with the pyrometallurgical benchmarks, making it an attractive option for companies seeking to reduce the environmental footprint of their metal recovery operations.

3 Materials and Methods

3.1 PCB Feedstock

All three experiments used PCBs from the same pre-processed batch, prepared by Monolithos. The XRF analysis of the raw solid confirmed copper as the dominant metal at 342,900 ppm (342.9 kg/tonne dry solid), with secondary metals at 1–3

kg/tonne: nickel (3.20 kg/t), cobalt (2.20 kg/t), cadmium (2.75 kg/t), zinc (2.65 kg/t), lead (2.19 kg/t) and chromium (1.01 kg/t).

3.2 Experimental Conditions at Each Scale

Table 1: Experimental parameters for the bioleaching trials at 2 L, 20 L, and 100 L scales

Parameter	2 L	20 L	100 L
Reactor vessel	5 L	20 L	100 L
Working volume	2 L	14 L	14 L
Duration	30 days	30 days	30 days
Inoculum (10 % v/v)	*A. ferrooxidans* + *A. Thiooxidans* (50:50)	*A. Thiooxidans* only	*A. Thiooxidans* only

3.3 XRF Analysis

The solid-phase elemental composition was determined by X-ray fluorescence (XRF) spectrometry on samples from the initial PCB powder (before inoculation) and from the dried filter cake at day 30. The samples were dried at 60 °C to constant weight before the analysis. The concentrations are reported in kg/tonne (equivalent to g/kg dry solid). The recovery yield was calculated according to Equation (1):

$$\text{Recovery (\%)} = [(C_0 - C_{end}) / C_0] \times 100 \quad (1)$$

where C_0 is the initial metal concentration and C_{end} is the residual concentration after bioleaching. Higher values indicate a greater transfer of metal from the solid phase into the leach solution. Control experiments (no bacteria) were run in parallel, to separate the biologically driven removal from the abiotic acid dissolution.

4 XRF Results: Solid-Phase Metal Removal

4.1 2 L Reactor

The XRF analysis of the solid before and after the 30-day trial at 2 L demonstrated effective metal removal across all seven elements. The copper – dominant at 342,900 ppm – decreased to 180,700 ppm, a recovery yield of 47.3 %. The moderate copper recovery at this scale reflects the layered, encapsulated nature of copper in the PCB laminate: the inner copper layers and thick electroplated pads require sustained acid

exposure for full dissolution, and 30 days under batch conditions was insufficient for complete solubilisation (Arshadi et al., 2019; Mostafavi et al., 2018; Saldaña et al., 2023).

The trace and minor metals showed markedly higher removal. Nickel recovery reached 93.4 %, chromium 96.3 %, cobalt 90.9 % and zinc 86.0 %. These elements are associated predominantly with surface coatings –ENIG layers, solder masks and component metallisations – that are accessible to bacterial attack rapidly at fine particle size. Cadmium (71.6 %) and lead (62.9 %) showed intermediate removal consistent with the partial dissolution of the solder materials. The control samples confirmed that abiotic acid dissolution alone produced substantially lower solid-phase depletion, validating the biological contribution.

Table 2: XRF solid-phase concentrations before and after bioleaching — 2 L reactor (30 days, 30 °C, mixed *A. ferrooxidans* + *A. Thiooxidans*)

Element	Before (kg/tonne)	After (kg/tonne)	Recovery (%)
Copper (Cu)	342.9	180.7	47.3
Nickel (Ni)	3.20	0.21	93.4
Chromium (Cr)	1.01	0.04	96.3
Cobalt (Co)	2.20	0.20	90.9
Zinc (Zn)	2.65	0.37	86.0
Cadmium (Cd)	2.75	0.78	71.6
Lead (Pb)	2.19	0.81	62.9

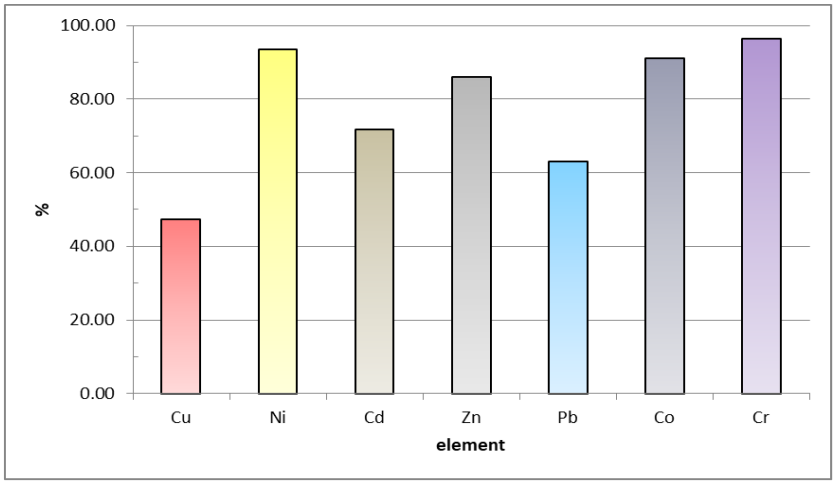

Figure 2: Yield potential for the 2 L experiment
Source: own.

4.2 20 L Reactor

The XRF analysis of the solid before and after the 30-day trial at 2 L demonstrated effective metal removal across all seven elements (Table 3 & Figure 3). The 20 L experiment, conducted with *A. Thiooxidans* alone in S-medium, yielded the highest copper recovery of any scale: 64.3 % (from 342,900 ppm to 122,300 ppm, a removal of 220,600 ppm). Nickel recovery remained high at 90.3 %, cadmium at 72.5 % and chromium at 74.1 %. Zinc recovery was 66.5 %, cobalt 56.1 % and lead 38.7 % – the last showing the greatest relative decline compared with the 2 L run. The transition from the dual-strain MIX medium to single-strain S-medium did not reduce the performance for the majority of elements, confirming *A. Thiooxidans* as an effective standalone leaching organism at this scale.

Table 3: XRF solid-phase concentrations before and after bioleaching — 20 L reactor (30 days, 30 °C, *A. Thiooxidans* only)

Element	Before (kg/tonne)	After (kg/tonne)	Recovery (%)
Copper (Cu)	342.9	122.3	64.3
Nickel (Ni)	3.20	0.31	90.3
Chromium (Cr)	1.01	0.26	74.1
Cobalt (Co)	2.20	0.96	56.1
Zinc (Zn)	2.65	0.89	66.5
Cadmium (Cd)	2.75	0.76	72.5
Lead (Pb)	2.19	1.34	38.7

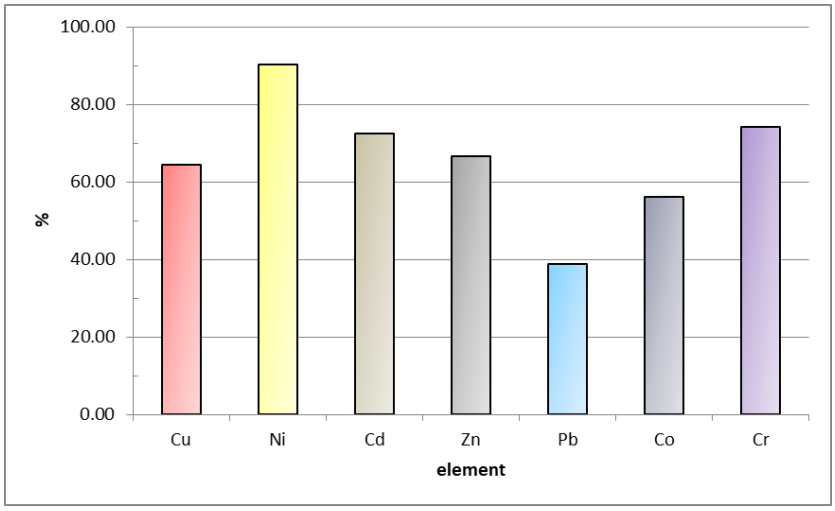

Figure 3: Yield potential for the 20 L experiment
Source: own.

4.3 100 L Reactor

At 100 L, the XRF analysis of the day-30 solid residue confirmed commercially relevant metal removal across all the elements (Table 4 & Figure 4). Copper recovery was 53.5 %, intermediate between the 2 L and 20 L values. Nickel recovery was 92.0 %, the highest of any scale, demonstrating the excellent robustness of nickel solubilisation at semi-industrial volumes. Chromium recovery was 74.7 %, consistent with the 20 L result. Cobalt dropped to 47.7 % and zinc to 74.2 %; cadmium (57.1 %) and lead (57.2 %) showed moderate removal. The control data confirmed that the observed solid-phase depletion was primarily biological in origin.

Table 4: XRF solid-phase concentrations before and after bioleaching — 100 L reactor (30 days, 30 °C, *A. Thiooxidans* only)

Element	Before (kg/tonne)	After (kg/tonne)	Recovery (%)
Copper (Cu)	342.9	159.6	53.5
Nickel (Ni)	3.20	0.26	92.0
Chromium (Cr)	1.01	0.26	74.7
Cobalt (Co)	2.20	1.15	47.7
Zinc (Zn)	2.65	0.69	74.2
Cadmium (Cd)	2.75	1.18	57.1
Lead (Pb)	2.19	0.94	57.2

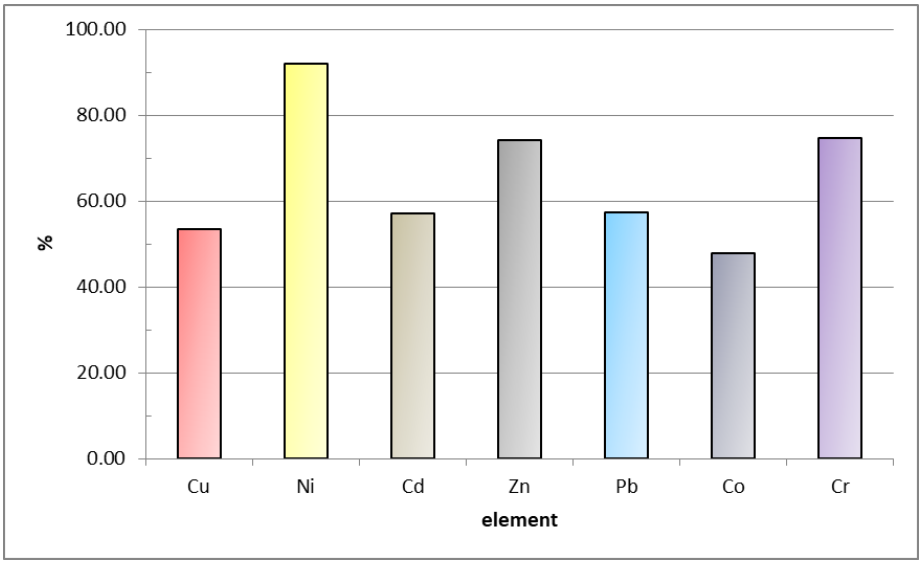

Figure 4: Yield potential for the 100 L experiment
Source: own.

5 XRF Results: Solid-Phase Metal Removal

Table 5 consolidates the XRF-based recovery yields across all three scales, revealing patterns that have direct implications for further scale-up.

Table 5: XRF-based solid-phase recovery yields (%) across all three reactor scales

Element	2 L (%)	20 L (%)	100 L (%)
Copper (Cu)	47.3	64.3	53.5
Nickel (Ni)	93.4	90.3	92.0
Chromium (Cr)	96.3	74.1	74.7
Cobalt (Co)	90.9	56.1	47.7
Zinc (Zn)	86.0	66.5	74.2
Cadmium (Cd)	71.6	72.5	57.1
Lead (Pb)	62.9	38.7	57.2

Copper recovery showed a non-monotonic trend, rising from 47.3% at 2 L to 64.3% at 20 L before falling to 53.5% at 100 L, contrary to the typical scale-up expectations of decreasing recovery due to mass transfer limitations (Saldaña et al., 2023). The improved performance at 20 L may result from using *A. thiooxidans* alone, which avoids competition with *A. ferrooxidans* and enhances sulphuric acid production, as well as more favourable mixing conditions. Nickel remained highly stable across the scales (90.3–93.4%), reflecting its presence in easily accessible ENIG coatings that dissolve readily (Arshadi et al., 2019). Chromium recovery dropped from 96.3% at 2 L to approximately 74% at larger scales due to the absence of *A. ferrooxidans*, which reduces Fe^{3+}-driven oxidative dissolution (Blaby-Haas, 2022; Potysz et al., 2016). Cobalt showed the steepest decline (90.9% to 47.7%), confirming its dependence on ferric iron (Adetunji et al., 2023; Saldaña et al., 2023). Zinc followed an intermediate pattern (86.0% → 66.5% → 74.2%), influenced by the mixing intensity and particle suspension (Fu et al., 2021; Mostafavi et al., 2018). Cadmium remained relatively consistent (71–72%) before declining at 100 L (57.1%), likely due to the higher pH reducing solubility (Rautela et al., 2021). Lead showed high variability (62.9% → 38.7% → 57.2%), due primarily to $PbSO_4$ precipitation, which underestimates the true recovery in the XRF analysis (Potysz et al., 2016; Srichandan et al., 2019).

6 Conclusions

A complete bioleaching process value chain for critical raw material recovery from e-waste PCBs has been demonstrated at three successive scales – 2 L, 20 L, and 100 L – each operated for 30 days at 30 °C. The XRF analysis of the solid phase at each scale provided the following key findings:

At 2 L, a mixed *A. ferrooxidans* / *A. thiooxidans* culture achieved Cu recovery of 47.3 %, Ni 93.4 %, Cr 96.3 %, and Co 90.9 %, establishing a strong laboratory benchmark. At 20 L, the single-strain *A. thiooxidans* produced the highest Cu recovery of any scale (64.3 %) while maintaining Ni above 90 %, validating the scale transfer. At 100 L, the Cu recovery was 53.5 % and Ni 92.0 %, confirming semi-industrial viability with only modest losses in Co and Zn recovery relative to the laboratory scale.

The primary recommendations for future work are: (i) develop dedicated inoculum fermenters for *A. ferrooxidans* to recover Co and Cr performance at a large scale; (ii) extend the bioleaching period beyond 30 days to approach the maximum Cu recovery; (iii) optimise the aeration and agitation at 100 L and beyond to reduce the performance gaps for Co and Zn; and (iv) implement real-time pH and ORP feedback control to maintain optimal conditions throughout the run. Together, these improvements are expected to bring large-scale copper recovery to 70 % or above, while sustaining the already excellent Ni and Cr yields, supporting commercialisation of the process as a low-carbon alternative to conventional e-waste smelting.

Acknowledgment

This work was carried out within the WEEE-NET9.SPEED project (Project No. 21115), supported by EIT RawMaterials and co-funded by the European Union. The authors acknowledge the contributions of Monolithos Catalysts & Recycling Ltd (Athens, Greece), as well as the project partners Ekosij d.o.o. (Slovenia), PowerHUB (Czech Republic) and the University of Miskolc (Hungary).

References

Adetunji, A.I., Oberholster, P.J., Erasmus, M., 2023. Bioleaching of Metals from E-Waste Using Microorganisms: A Review. Minerals 13, 828. https://doi.org/10.3390/min13060828

Arshadi, M., Yaghmaei, S., Mousavi, S.M., 2019. Optimal electronic waste combination for maximal recovery of Cu-Ni-Fe by Acidithiobacillus ferrooxidans. Journal of Cleaner Production 240, 118077. https://doi.org/10.1016/j.jclepro.2019.118077

Baldé, C.P., Kuehr, R., Yamamoto, T., McDonald, R., D'Angelo, E., Althaf, S., Bel, G., Deubzer, O., Fernandez-Cubillo, E., Forti, V., Gray, V., Herat, S., Honda, S., Iattoni, G., di Cortemiglia, V.L., Lobuntsova, Y., Nnorom, I., Pralat, N., Wagner, M., 2024. THE GLOBAL E WASTE MONITOR 2024.

Debbarma, P., Suyal, D.C., Kumar, S., Joshi, D., Singh, M., Rajwar, J., Rawat, B., Dasila, H., Maithani, D., Soni, R., 2023. Bioremediation of E-waste Through Microbial Exopolysaccharides: A Perspective, in: Debbarma, P., Kumar, S., Suyal, D.C., Soni, R. (Eds.), Microbial Technology for Sustainable E-Waste Management. Springer International Publishing, Cham, pp. 245–257. https://doi.org/10.1007/978-3-031-25678-3_15

Dhiman, V., 2023. Metal Bioleaching from E-waste Using Fungal Communities, in: Debbarma, P., Kumar, S., Suyal, D.C., Soni, R. (Eds.), Microbial Technology for Sustainable E-Waste Management. Springer International Publishing, Cham, pp. 201–211. https://doi.org/10.1007/978-3-031-25678-3_12

European Commission. (2023). Circular economy - material flows. *Eurostat*. https://ec.europa.eu/eurostat/statistics-explained/index.php?title=Circular_economy_-_material_flows (accessed 12 June 2025)

Fu, K., Tian, L., Hou, P., Long, M., Chen, S., Lin, H., 2021. Stirred-tank leaching of coarse-grained waste, printed circuit boards with Acidithiobacillus ferrooxidans. Physicochem. Probl. Miner. Process. https://doi.org/10.37190/ppmp/141558

Hurst, C.J. (Ed.), 2022. Microbial Metabolism of Metals and Metalloids, Advances in Environmental Microbiology. Springer International Publishing, Cham. https://doi.org/10.1007/978-3-030-97185-4

Ji, X., Yang, M., Wan, A., Yu, S., & Yao, Z. (2022). Bioleaching of typical electronic waste—Printed circuit boards (WPCBs): A short review. *International Journal of Environmental Research and Public Health, 19*(12), 7508. https://doi.org/10.3390/ijerph19127508

Lundberg, B.A., 2025. Global WEEE Management: Behavior and Future Projections. JSR 9, 17–26. https://doi.org/10.58970/JSR.1092

Manikandan, N., Awasthi, M. K., & Kumar, V. (2021). Biotechnological recovery of metals from e-waste: Opportunities and challenges. *Environmental Technology & Innovation, 24*, 102034. https://doi.org/10.1016/j.eti.2021.102034

Marinič, D., Štruc, M., & Oprčkal, P. D. (2025). Eco-friendly bioleaching : innovative technology for extracting critical raw materials from WEE. *In 7th International Conference on Technologies & Business Models for Circular Economy*. University of Maribor, University Press, Maribor. https://dirros.openscience.si/IzpisGradiva.php?id=23011&lang=slv (accessed 14 July 2025)

Mostafavi, M., Mirazimi, S.M.J., Rashchi, F., Faraji, F., Mostoufi, N., 2018. Bioleaching and Kinetic Investigation of WPCBs by A. Ferrooxidans, A. Thiooxidans and their Mixtures. J. Chem. Pet. Eng. 52. https://doi.org/10.22059/jchpe.2018.255842.1227

Potysz, A., Lens, P.N.L., Van De Vossenberg, J., Rene, E.R., Grybos, M., Guibaud, G., Kierczak, J., Van Hullebusch, E.D., 2016. Comparison of Cu, Zn and Fe bioleaching from Cu-metallurgical slags in the presence of Pseudomonas fluorescens and Acidithiobacillus thiooxidans. Applied Geochemistry 68, 39–52. https://doi.org/10.1016/j.apgeochem.2016.03.006

Rautela, R., Arya, S., Vishwakarma, S., Lee, J., Kim, K.-H., Kumar, S., 2021. E-waste management and its effects on the environment and human health. Science of The Total Environment 773, 145623. https://doi.org/10.1016/j.scitotenv.2021.145623

Saldaña, M., Jeldres, M., Galleguillos Madrid, F.M., Gallegos, S., Salazar, I., Robles, P., Toro, N., 2023. Bioleaching Modeling—A Review. Materials 16, 3812. https://doi.org/10.3390/ma16103812

Srichandan, H., Mohapatra, R.K., Parhi, P.K., Mishra, S., 2019. Bioleaching approach for extraction of metal values from secondary solid wastes: A critical review. Hydrometallurgy 189, 105122. https://doi.org/10.1016/j.hydromet.2019.105122

Upadhyay, R., Ramayya, P.J., 2023. Role of Biotechnological Approaches for the Valorization of Precious Metals from E-waste, in: Debbarma, P., Kumar, S., Suyal, D.C., Soni, R. (Eds.), Microbial Technology for Sustainable E-Waste Management. Springer International Publishing, Cham, pp. 319–335. https://doi.org/10.1007/978-3-031-25678-3_20

8TH INTERNATIONAL CONFERENCE ON TECHNOLOGIES & BUSINESS MODELS FOR CIRCULAR ECONOMY: CONFERENCE PROCEEDINGS

SANJA POTRČ, MILOŠ BOGATAJ, ZDRAVKO KRAVANJA, ZORKA NOVAK PINTARIČ (EDS.)

University of Maribor, Faculty of Chemistry and Chemical Engineering, Maribor, Slovenia
sanja.potrc@um.si, milos.bogataj@um.si, zdravko.kravanja@um.si, zorka.novak@um.si

The 8th international scientific, professional and development conference *Technologies & Business Models for Circular Economy* (TBMCE) was organised by the Faculty of Chemistry and Chemical Engineering, University of Maribor, in collaboration with the Strategic Research and Innovation Partnership – Networks for the Transition into Circular Economy (SRIP – Circular Economy), managed by the Chamber of Commerce and Industry of Štajerska. The event took place from 3 to 5 September 2025 at the Grand Hotel Bernardin in Portorož, Slovenia. The conference addressed key research and development areas related to the transition to a circular economy, including improvements in energy efficiency, process electrification, and the use of renewable and low-carbon energy sources. Particular emphasis was placed on the optimisation of resource use, recovery of critical materials from waste, and the conversion of residues into high value-added products. Approaches to sustainable water resource management, circular CO_2 utilisation, and the development of green processes and technologies were also discussed. In addition, aspects of digitalisation, standardisation, and the development of innovative circular business models were considered as key enabling mechanisms for the transition to a circular economy.

DOI
https://doi.org/10.18690/um.fkkt.1.2026

ISBN
978-961-299-130-2

Keywords:
circular economy, sustainable development, processes and technologies, circular business models, research and development

University of Maribor Press

University of Maribor

Faculty of Chemistry and Chemical Engineering

2025

September 3 - 5

Grand Hotel Bernardin
Portorož, Slovenia